creative commons
COMMONS DEED

저작자표시 2.0 대한민국

이용자는 아래의 조건을 따르는 경우에 한하여 자유롭게

- 이 저작물을 복제, 배포, 전송, 전시, 공연 및 방송할 수 있습니다.
- 이차적 저작물을 작성할 수 있습니다.
- 이 저작물을 영리 목적으로 이용할 수 있습니다.

다음과 같은 조건을 따라야 합니다:

**저작자표시**. 귀하는 원저작자를 표시하여야 합니다.

- 귀하는, 이 저작물의 재이용이나 배포의 경우, 이 저작물에 적용된 이용허락조건을 명확하게 나타내어야 합니다.
- 저작권자로부터 별도의 허가를 받으면 이러한 조건들은 적용되지 않습니다.

**저작권법에 따른 이용자의 권리는 위의 내용에 의하여 영향을 받지 않습니다.**

이것은 이용허락규약(Legal Code)을 이해하기 쉽게 요약한 것입니다.

Disclaimer

dCollection

[UCI]I804:48009-200000363483

**Doctor of Philosophy**

# A SENSORLESS REFLECTING CONTROL FOR BILATERAL HAPTIC TELEOPERATION SYSTEM BASED ON PNEUMATIC ARTIFICIAL MUSCLE ACTUATORS

**The Graduate School**

**of the University of Ulsan**

**School of Mechanical Engineering**

**CONG PHAT VO**

# A SENSORLESS REFLECTING CONTROL FOR BILATERAL HAPTIC TELEOPERATION SYSTEM BASED ON PNEUMATIC ARTIFICIAL MUSCLE ACTUATORS

**CONG PHAT VO**

**School of Mechanical Engineering**

**University of Ulsan, Korea**

# A SENSORLESS REFLECTING CONTROL FOR BILATERAL HAPTIC TELEOPERATION SYSTEM BASED ON PNEUMATIC ARTIFICIAL MUSCLE ACTUATORS

Supervisor: Professor KYUONG KWAN AHN

A Dissertation

Submitted to
the Graduate School of the University of Ulsan
In Partial Fulfillment of the Requirement
for the Degree of

DOCTOR OF PHILOSOPHY
(Mechanical and Automotive Engineering)

by

CONG PHAT VO

School of Mechanical Engineering

University of Ulsan, Korea

February 2021

# A SENSORLESS REFLECTING CONTROL FOR BILATERAL HAPTIC TELEOPERATION SYSTEM BASED ON PNEUMATIC ARTIFICIAL MUSCLE ACTUATORS

**This certifies that the dissertation of**
**CONG PHAT VO is approved by**

| | | |
|---|---|---|
| **Committee Chair:** | **Prof. CHEOL KEUN HA** | |
| **Committee Member:** | **Prof. BYUNG RYONG LEE** | |
| **Committee Member:** | **Prof. KYUONG KWAN AHN** | |
| **Committee Member:** | **Prof. HEE JUN KANG** | |
| **Committee Member:** | **Prof. JOON BUM BAE** | |

**School of Mechanical Engineering**
**University of Ulsan, Korea**
**February 2021**

## Acknowledgments

First of all, I would like to express my deepest gratitude to my supervisor, Professor Kyoung Kwan Ahn, who has kept inspiring me to explore far beyond my own expectation. It has been a great experience to do research under this technical guidance, during which he has shared a lot of his experience. He has always encouraged and taught me to strive for a single goal, and it had a deep impact on my research. He has provided me with opportunities to visit local industries, attend international conferences and meet with top scientists around the world, which were invaluable experiences and broadened my vision.

I would like to express my gratitude to committee members, Prof. Cheol Keun Ha, Prof. Byung Ryong Lee, Prof. Kyoung Kwan Ahn, Prof. Hee Jun Kang, and Prof. Joon Bum Bae, for evaluating and providing suggestions and comments throughout this thesis.

My sincere gratitude and respect go to my colleagues in Korea and in Vietnam, and all labmate: Fluid Power and Machine Intelligence Laboratory, University of Ulsan, for their help, sharing, discussion, and co-working during my study time here. I would like to express gratitude to the Korea National research projects, University of Ulsan, Korea and Thu Duc College of Technology, Viet Nam for providing me with a great opportunity and financial support to pursue my Ph.D. degree.

At last but not least, I give my dearest gratitude to my family: grandmother, parents, younger brother, my girlfriend Ms. Nguyet Que and her family, who have given me motivation in life and the freedom to pursue my dream. I have owed them so much that I could not pay back in a lifetime.

Ulsan, Korea, February 2021

**Cong Phat Vo**

# Contents

Acknowledgments ..... I

Contents ..... II

List of Figures ..... V

List of Tables ..... VII

Nomenclature ..... VIII

ABSTRACT ..... XI

Chapter 1 INTRODUCTION ..... 1

1.1 Overview ..... 1
1.2 Research objectives ..... 3
1.3 Limitation of the dissertation ..... 4
1.4 Dissertation outline ..... 4

Chapter 2 MODELING OF THE BILATERAL TELEOPERATION SYSTEM BASED ON THE APAM CONFIGURATION ..... 6

2.1 Mathematical modeling ..... 6
2.2 Experimental modeling ..... 9
2.3 The BHTS modeling ..... 11
2.4 Platform setup of the BHTS ..... 12

Chapter 3 ADAPTIVE GAIN INTEGRAL TERMINAL SLIDING MODE CONTROL SCHEME OF A APAM SYSTEM BASED ON TDE ..... 15

3.1 Introduction ..... 15
3.2.1 Overview ..... 15
3.2.2 The proposed control scheme for the PAM system ..... 16
3.2 Proposed control description ..... 18
3.2.1 The Integral Terminal Sliding Mode Controller ..... 18
3.2.2 The Proposed Adaptive Gain ITSMC with TDE ..... 20
3.3 Experimental Validation ..... 22
3.3.1 Case study 1 ..... 23
3.3.2 Case study 2 ..... 24
3.3.3 Case study 3 ..... 25
3.3.4 Case study 4 ..... 26
3.4 Chapter summary ..... 28

Chapter 4 ADAPTIVE FINITE-TIME FORCE CONTROL SCHEME OF A APAM SYSTEM WITH TDE ..... 29
4.1 Introduction ..... 29
4.1.1 Overview ..... 29
4.1.2 The proposed control idea ..... 31
4.2 Controller descriptions ..... 32
4.2.1 Proposed Friction Free Force combined State Observer ..... 32
4.2.2 The proposed nonlinear control design ..... 34
4.3 Experimental results and discussion ..... 37
4.3.1 Estimation Force Validation ..... 38
4.3.2 Scenario 1 ..... 39
4.3.3 Scenario 2 ..... 39
4.3.4 Scenario 3 ..... 40
4.4 Chapter summary ..... 42
Chapter 5 MODEL-FREE CONTROL FOR OPTIMAL CONTACT FORCE OF A APAM SYSTEM IN UNKNOWN ENVIRONMENTS USING RL ..... 43
5.1 Introduction ..... 43
5.1.1 Overview ..... 43
5.1.2 The proposed control idea ..... 44
5.2 Control Strategy ..... 44
5.2.1 Robot Position/Force control ..... 44
5.2.2 Optimal desired force ..... 46
5.3 Validation results ..... 51
5.4 Chapter summary ..... 54
Chapter 6 HUMAN-ROBOT INTERACTIVE CONTROL FOR A APAM CONFIGURATION-BASED HAPTIC INTERFACE USING IRL ..... 56
6.1 Introduction ..... 56
6.1.1 Overview ..... 56
6.1.2 Proposed idea ..... 57
6.2 Developed a Human-Robot Interaction System. ..... 58
6.2.1 Robot-Specific Inner-Loop Control ..... 59
6.2.2 Task-Oriented Outer-Loop Control ..... 61
6.3 Validation results ..... 66
6.3.1 Simulation results ..... 66
6.3.2 Experimental results ..... 68
6.4 Chapter summary ..... 70

Chapter 7 FORCE SENSORLESS REFLECTING CONTROL FOR BILATERAL HAPTIC TELEOPERATION SYSTEM ..... 71
7.1 Introduction. ..... 71
7.1.1 Overview ..... 71
7.1.2 Proposed control idea of the bilateral haptic teleoperation ..... 73
7.2 The Nonlinear Bilateral Controller Design ..... 73
7.2.1 Control Contact Force Estimation Using Adaptive Observer ..... 74
7.2.2 Master control design ..... 77
7.2.3 Slave control design ..... 78
7.3 Experimental results and discussion ..... 80
7.3.1 Force Estimation ..... 81
7.3.2 Tracking control performance ..... 82
7.3.3 Transparency performance ..... 85
7.4 Chapter summary ..... 86
Chapter 8 CONCLUSION AND FUTURE WORKS ..... 88
8.1 Conclusion ..... 88
8.2 Future works ..... 89
Appendix ..... 90
Appendix 3.1 ..... 90
Appendix 3.2 ..... 90
Appendix 3.3 ..... 90
Appendix 3.4 ..... 91
Appendix 4.1 ..... 92
Appendix 4.2 ..... 92
Appendix 4.3 ..... 93
Appendix 5.1 ..... 94
Appendix 6.1 ..... 95
Appendix 6.2 ..... 97
Appendix 7.1 ..... 97
Appendix 7.2 ..... 98
Appendix 7.3 ..... 98
Appendix 7.4 ..... 99
Appendix 7.5 ..... 100
PUBLICATIONS ..... 101
REFERENCES ..... 103

## List of Figures

Figure 1. The bilateral haptic teleoperation architecture with the transmission signal. ..... 2
Figure 2. Structure (a) and working principle (b) of the PAM. ..... 3
Figure 3. A cross-sectional view of the simplified geometric model of PAM. ..... 6
Figure 4. Response of the PAM system. (a, b) Open-loop control, (c) Hysteresis curve. ..... 9
Figure 5. Response of d(t) and time-delay estimation error. ..... 9
Figure 6. Response of the APAM system. (a) the chirp control signal, (b) Hysteresis curve. . 10
Figure 7. Experimental results of the PAM for certain separate pressure values. ..... 10
Figure 8. The 3D CAD design and the test rig setup of the master system. ..... 13
Figure 9. The 3D CAD design and the test rig setup of the slave system. ..... 14
Figure 10. Photograph of the experimental apparatus of the overview BHTS. ..... 14
Figure 11. Structure of Adaptive Gain ITSMC with TDE scheme. ..... 17
Figure 12. (a) Working principle and (b) Configuration of the experimental system. ..... 23
Figure 13. Comparison of control performance with respect to case study 1. ..... 24
Figure 14. Comparison of control performance with respect to case study 2. ..... 25
Figure 15. Comparison of control performance with respect to case study 3. ..... 26
Figure 16. Histories of robust control gain in the loading case study 4. ..... 27
Figure 17. Comparison of control performance with respect to case study 4. ..... 27
Figure 18. Structure of the proposed control. ..... 32
Figure 19. Environment force estimation performances of three comparative observers. ..... 38
Figure 20. Comparison of control performance with respect to scenario 1. ..... 39
Figure 21. Comparison of control performance with respect to scenario 2 ..... 40
Figure 22. Comparison of control performance with respect to scenario 3. ..... 41
Figure 23. Control gain in scenarios. ..... 41
Figure 24. Structure of the proposed optimal contact force control. ..... 45
Figure 25. Environment parameter estimation with RLS. ..... 51
Figure 26. RL in unknown environments during the learning process. ..... 52
Figure 27. Learning curves. ..... 52
Figure 28. Desired force and position tracking response. ..... 53
Figure 29. (a) A human hand model in human-robot interaction. (a) Working principle of the human-robot system based-APAM. ..... 58

Figure 30. Control scheme with double loops for the human-robot interaction control. ..... 60
Figure 31. The tracking error of the robot trajectory and the prescribed impedance model. ... 67
Figure 32. Reference versus the output trajectory during and after learning. ..... 67
Figure 33. The output trajectory and the prescribed impedance model in the inner loop. ..... 69
Figure 34. The desired trajectory and the output trajectory in the outer loop. ..... 69
Figure 35. Interaction force. ..... 69
Figure 36. The proposed bilateral control scheme for APAM actuated haptic system. ..... 74
Figure 37. Comparison of torque estimation performances in the interaction condition. ..... 81
Figure 38. Comparison of the tracking position performances in the free space situation. ..... 83
Figure 39. Transparency performance of the BHTS in the free motion and soft contract. ..... 84
Figure 40. Transparency errors of the BHTS in the free motion and soft contract. ..... 84
Figure 41. Transparency performance of the BHTS in the free motion and stiff contract. ..... 85
Figure 42. Transparency errors of the BHTS in the free motion and stiff contract. ..... 85

## List of Tables

Table 1. Parameters of The Studied PAM Model. ..... 8
Table 2. List of APAM model parameters. ..... 10
Table 3. Specifications of the experimental devices. ..... 11
Table 4. Performance indices of comparative controllers ..... 28
Table 5. Performance indices of comparative controllers. ..... 83

## Nomenclature

| | |
|---|---|
| $L$ | muscle length |
| $D$ | muscle diameter |
| $\theta$ | the initial angle between the axis of the muscle and fibers |
| $b$ | the length of single knitted fibers mesh shell |
| $n$ | the winding turns of fibers |
| $d$ | the lump disturbance |
| $\xi_k$ | the displacement and air pressure of the $k^{\text{th}}$ PAM |
| $P_k$ | the air pressure and air pressure of the $k^{\text{th}}$ PAM |
| $P_0$ | the initial pressure |
| $\Delta P$ | the pressure difference |
| $\upsilon_i$ | the auxiliary variables |
| $\rho$ | the integral sliding surface |
| $s$ | the terminal sliding surface |
| $u_n$ | the nominal control signal |
| $u_s$ | the robust control signal |
| $\hat{d}$ | the estimation value of the lump disturbance |
| $\varepsilon_d$ | the time delay estimation error |
| $\hat{\eta}_3$ | the estimation value of the robust control gain |
| $\mu, \delta, \sigma$ | the adaptation gains |
| $\delta, \eta$ | the positive scalar of the AFOB |
| $\kappa$ | the online updated value of the AFOB |
| $\overline{\varsigma}_i$ | the positive design parameter of the AFOB |
| $t_d$ | the time delay parameter |
| $t$ | the sampling period |
| $\tau_e$ | the external torque |
| $\tau_e^*$ | the periodic torque |
| $\hat{\tau}_e$ | the estimated force of the external force |
| $\tau$ | the generalized joint torque coordinates |
| $\tau_d$ | the general nonlinear disturbance |

$\tau_h$ the human control effort

$\tau_m$ the applied control torque in the master system

$\tau_s$ the applied control torque in the slave system

$\hat{\tau}_m$ the estimated force of the external force in the master system

$\hat{\tau}_s$ the estimated force of the external force in the slave system

$F_d$ the desired force applied on the environment

$F_d^*$ the optimal desired force applied on the environment

$F_e$ the robot-environment interaction force

$\theta$ the output position of the joint

$\theta_d$ the desired position in joint space

$\theta_m$ the output position of the desired impedance model

$\theta_{mf}$ the output position of the impedance filter

$\theta_{sd}$ the home position of the slave system

$\theta_{md}$ the home position of the master system

$\omega_e$ the predetermined angular frequency of the additional periodic signal

$\xi_e$ the indicates the damping ratio

$\sigma$ the integral terminal sliding mode surface

$K_h$ the human input force gain

$K_s$ the control gain

$\sigma_h$ the sliding mode error

$\psi$ the disturbance compensation

$\hat{\psi}$ the neural network approximation

$W_i$ the weights of the NN functional approximation

$\phi_i$ the parameters of the neural approximation

$\hat{\kappa}_5$ the adaptive switching gain law of the FITSMC

$x$ the position of the robot end-effector in task space

$x_e$ the environment position

$x_r$ the virtual reference trajectory

$x_d$ the desired reference trajectory

$r_0$ the distance of the contact force

$e_f$ the force tracking error differencing the desired-contact force

$e_r$ the error between the desired position and a virtual reference

$e_h$ the tracking error differencing the system position and the impedance model output

$Q$ the cost-to-go value function

$\hat{Q}$ the approximated cost-to-go value function

$\Psi$ the normalized RBFs

$N$ the number of RBFs

$\sigma$ the width of RBF

$K$ the number of clusters

$\upsilon$ the learning rate

$\gamma$ the discount factor

$\delta_\Delta$ the trace decay factor

$\varepsilon$ the greedy exploration strategy

$\varepsilon$-decay the greedy decay factor

$S, R, P, B$ the weight of the ARE

$M, C, K$ the inertia, viscosity and stiffness of the system model

$\bar{M}, \bar{C}, \bar{K}$ the nominal values of the inertia term $M$, damping term $C$, stiffness term $K$

$M_e, C_e, K_e$ the inertia, viscosity and stiffness of the environment model

$M_a, C_a, K_a$ the inertia, viscosity and stiffness of the impedance model in the slave system

$M_d, C_d, K_d$ the inertia, viscosity and stiffness of the impedance model in the master system

$\kappa_p, \kappa_d, k_e$ the unknown gains of the human transfer function

$\alpha_1, \alpha_2, \alpha_3, \alpha_4$ the parameters of LeD

$K_p, K_i, K_d$ the parameters of PID

$\eta_1, \eta_2, \kappa_1, \kappa_2, \gamma_1, \gamma_2$ the parameters of the BTSMC for the nominal system

$k_1, k_2, \alpha, \eta_3, \kappa_3, \kappa_4$ the parameters of the ITSMC

$\lambda_1, \lambda_2, \kappa_4, \kappa_5, K_c, \nu, \eta_4, \eta_5$ the parameters of the FITSMC

## ABSTRACT

This thesis builds the bilateral haptic teleoperation system (BHTS) driven by pneumatic artificial muscle (PAM) actuators applying studied control approaches. The BHTS enables human users to conduct remote complex tasks in spatial decoupling or inaccessible environments, while can be able to provide the haptic perception of being present for the human operator. However, it is very difficult to ensure a highly accurate performance as well as properties of the BHTS due to incorporation simultaneously between the master-human and slave-environment, the existence of uncertain, nonlinear and unknown terms inside the PAM system dynamics. The strategy of this study begins with developing independent control for each feature of the master and slave system. To start with, the thesis presents several methods to determine both mathematical and experimental models of the haptic bilateral system. Then, a novel integral terminal sliding mode control (ITSMC) scheme is designed as a combination of a nominal control scheme and a discontinuous robust control scheme. Moreover, and time-delay estimator (TDE) technique and an adaptation gain for the ITSMC scheme are not only eliminated uncertainty but also developed to faded the chattering of the control signal and estimate the ideal robust gain. All of them are analyzed via a Lyapunov-based algorithm. The positioning task of both the master/slave systems applies the above-developed controllers and achieve great efficiency. Meantime, for force tracking performance, a fast finite-time nonlinear controller is developed from the fast ITSMC framework with TDE and adaptive switching terms and a friction-free disturbance combined state observer to compensate disturbances. After robot-specific loop implementations are performed, the controller for the bilateral haptic teleoperation control is designed wherein the interactive forces are completely estimated by the upgraded a novel adaptive force observer (AFOB) to external forces without using any force sensor and an advanced state control method is adopted to stabilize the closed-loop system. The robustness, transparency, effectiveness and feasibility of the proposed methods are definitely proven by the theoretical proof and comparative experiments. Especially, to increase the responsiveness to an unknown environment and human behavior, several additional studies in turn for slave-environment interaction and human-mater interaction are based on the learning mechanism. Specifically, a model-free control based on the reinforcement learning (RL) method is established to optimize the desired force from slave-environment interaction.

Meanwhile, an integral RL technique is then integrated to adjust the parameter of the prescribed impedance model for human-mater interaction. All proposed algorithms are not only demonstrated by the theoretical proof but also verified in experimental trials.

# Chapter 1
# INTRODUCTION

## 1.1 Overview

The bilateral haptic teleoperation technology [1] enables a human operator the ability to conduct remote complicate tasks while receiving haptic feedback, as seen in Figure 1. Specifically, the human operates the haptic interface or the master system and transmits signals to the remotely located slave system or the teleoperator, which performs the tasks and interacts with an unknown environment. Meanwhile, the interaction signals between the slave and the environment can be feedbacked to the human through the master system. These signals between the human-master and slave-environment are exchanged via the communication channels. Hence, the BHTS has many factors that affect operated quality. Based on a series of previous researches relating to this topic shows that the evaluation is normally dependent on several critical properties such as stability, perception, or transparency. Ideally, these properties are simultaneously optimized without destabilizing the global system stability. For this purpose, the specific parameters of the system such as the type of master and slave device, the reliability of the sensor and actuator, as well as time-varying delay or packet loss in the communication channels have to be taken into account in the controller design. In order to achieve an ideal BHTS, the consideration of additional information about the remote environment, the human behavior as well as the problems accrued into communication is necessary at least there will be certain improvements.

From a system configuration perspective, The requirement for flexibility and compliance for the applications in rehabilitation robotics, prosthetic robots, and especially the human-robot interaction, has ignited the growing interest of soft robots in recent years. The main components of soft robots are soft actuators, which are made of compliant materials. Among the soft actuators, pneumatic artificial muscle (PAM) actuator is considered as one of the most promising solutions due to many advantages of security, lightweight, cleaning, high force-to-weight, and force-to-volume ratio [1]. PAM is a pipe-like actuator that generates a pulling force as the bladder to make contact with the braid fibers via internal air pressurization and contracts in the axial direction whereas expanding in the radial direction. Since the PAM has many above-mentioned benefits, it has been widely used in the fields of medical treatment [2], gait rehabilitation [3], [4], biomedicine [5], [6], etc. Moreover, the PAM has natural compliance that

makes it feasible for biomimetic robotic devices, particularly those intended for interaction with humans. For more detail, an artificial muscle PAM consists of an internal bladder (rubber tube) surrounded by a braided mesh shell (with flexible yet non-extensible threads) that is attached at either end to fittings or some tendon-like structure, as shown in Figure 2. Then the pair of the PAM could be utilized to form an antagonistic single-freedom joint, called APAM, similar to a couple of antagonistic muscles of human beings.

To realize the PAM actuator into a real-time BHTS application, many approaches have been performed during recent decades. To derive a mathematical model of the PAM, the static and dynamic characteristics of the system were studied based on physical analyses by Chou et al. and Tondu et al. [7-9]. Some general aspects were deeply considered in these studies such as the relationship between pressure and force, changes in the geometric structure, the contraction ratio, the elastic characteristics, and viscous and Coulomb frictions. However, validating the obtained results shows that it is difficult to describe an accurate model of the actuator due to the existence of the uncertain, nonlinear, and unknown terms inside the device. Meanwhile, to cover the challenges in control performance, some conventional and extended proportional-integral-derivative (PID) controllers were proposed by Kawashima et al. and Ganguly et al. [10-12]. Obtaining a good control result proved the effectiveness of such methods. Due to the high nonlinearity and sensitivity to working conditions of the PAM systems (for instance, the supplied pressure, temperature, or viscosity), the applicability of the controllers is limited only to a specific region. As a result, to provide better control results by dealing with these limitations, this thesis proposes to display comprehensively available control strategies for the BHTS based on the concepts associated with its properties.

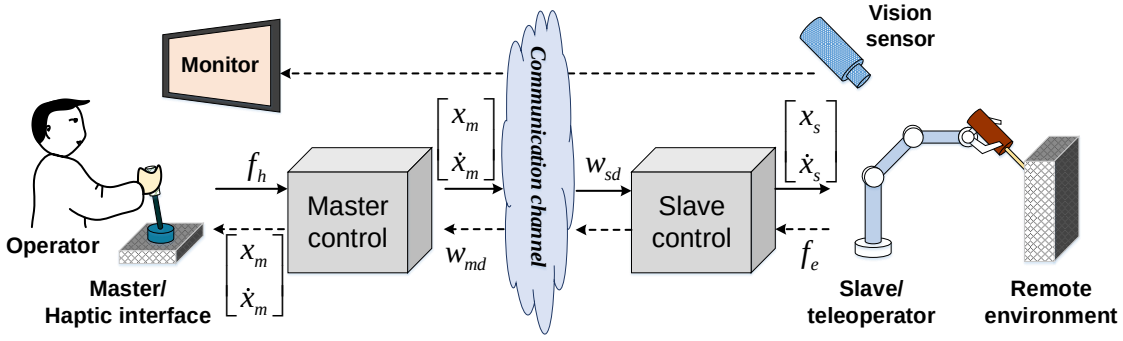


*Figure 1. The bilateral haptic teleoperation architecture with the transmission signal.*

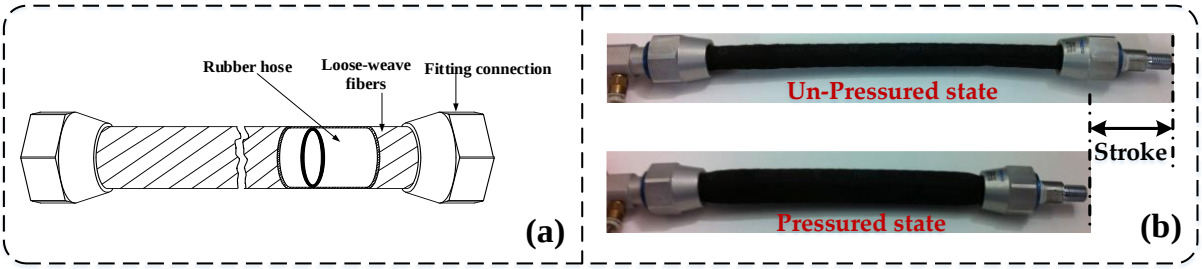


*Figure 2. Structure (a) and working principle (b) of the PAM.*

## 1.2 Research objectives

The main objectives of this dissertation are first of all to introduce a new study for the bilateral haptic teleoperation based on the APAM configuration. Then there are provided some effective control strategies for a PAM system based on combinations of intelligent estimation as well as learning machine and nonlinear control techniques. For a master or slave system, each subsystem had specific objectives which can be summarized as follows. In the slave subsystem, both position and force are considered in free-motion or contact-motion with an unknown environment, in which the system model is analyzed at both mathematical or experimental approaches. Then, in the first proposed control strategy, an integral terminal-style sliding mode controller is designed with the combination of an adaptive gain and time-delay estimation (TDE) to realize the robustness performance of the control objective and minimize control energy. The control parameters are then optimized by a backpropagation method. To verify the adaptive integral terminal sliding mode control (AITSMC) approach, some experiments are performed in a real-time PAM test rig. Through comparing with a conventional PID controller under different conditions, the effectiveness and feasibility of the AITSMC controller are confirmed.

Next, the interacted force properties with the environment are considered. In detail, a new force sensorless finite-time control scheme is investigated based on the new adaptive gain fast ITSMC combined with a friction-free disturbance (FSOB). As the experimental results, it can be easily seen that applicability for a system and simplicity in the design are advantages of the robust controller. After investigating the position and force features of the PAM system by several proposed strategies, one of the difficult problems is needed to solve, when the detailed interacted human or environmental parameters are unknown.

For robot-environment interaction control in the slave subsystem, the model-free controllers for optimal contact force are based on learning online ability via the RL technique. It is improved the classical human-robot interaction control to optimize the impedance model parameter using the RL methods.

Successively, in the master subsystem, human behavior may lead to difficulty in processing the outer-task. To address this drawback, the internal parameters of a prescribed impedance model of the system dynamics can be optimal by using integral reinforcement learning (IRL). It is solved the given output-feedback algorithm without the human model information while Recurrent Neural Network (RNN) is provided a control strategy with perfectly tracking position control. Human-robot interaction force during the robot performing manipulation is presented as a novel barrier-Lyapunov-function.

Finally, a novel force sensorless reflecting control for a haptic-enabled device driven by a bilateral PAM system. With the wish to develop a simple, fast and robust online estimation, the novel adaptive force observer (AFOB) is proposed to estimate external forces without using any force sensor signal. Meanwhile, the separately fast finite time nonsingular terminal sliding mode control (FNTSMC) schemes are developed based on the force estimation in both subsystems to achieve good tracking performance and fast response. Thus, the great transparency performance with both force feedback and position tracking can be achieved simultaneously by using the proposed method. The finite-time stability of the total controlled system is demonstrated by the Lyapunov approach. Some limitations of the designed methods are discussed.

## 1.3 Limitation of the dissertation

The effectiveness and feasibility of the proposed controllers have been confirmed in both theoretical proof and experimental validation. However, some limitations can be remarked as follows. In control design in joint-space, some proper control strategies are employed to stabilize the closed-loop system with a highly robust property. Deploying these controllers with many control parameters, which are mainly tuned by the trial-and-error method, in a real-time system is really not a trivial task for an inexpert one. Besides, the proposed control strategies in joint-space are almost based on the mathematical or experimental model. For the faster convergence rate, the method should be implemented from the exact mathematical model of the system dynamics. In the model approximation strategies in task-space, because of the existence of reward function and the process of learning, the computational complexity scales exponentially with the size of data. One big problem to learn control policy from a large number of data. Based on the investigation in this thesis, the author believes that it is possible to develop the learning method for both the master and slave systems. Moreover, the controllers can be embedded in an applicated device practically. These limitations will be done in the near future.

## 1.4 Dissertation outline

The remainder of this thesis is organized as follows. The general hardware configuration and modeling of the studied BHTS system are introduced in Chapter 2. Chapter 3 presents the design procedure of the adaptive gain ITSMC control scheme for position tracking the APAM system. The force finite-time sensorless control is proposed to handle the contact force, which is illustrated in Chapter 4 while the integrated intelligent control approach employed to further improve the environmental interaction control efficiency is provided in Chapter 5. In Chapter 6, human-robot cooperative control is developed for learning of operator behaviors, and the proposed RNN controller is guaranteed position control. In Chapter 7, the force sensorless reflecting control-assisted AFOB for a BHTS-actuated APAM configuration is validated and discussed once again in this prototype. Finally, the conclusions of the study and the recommendations discussed as future works are presented in Chapter 8.

# Chapter 2

# MODELING OF THE BILATERAL TELEOPERATION SYSTEM BASED ON THE APAM CONFIGURATION

## 2.1 Mathematical modeling

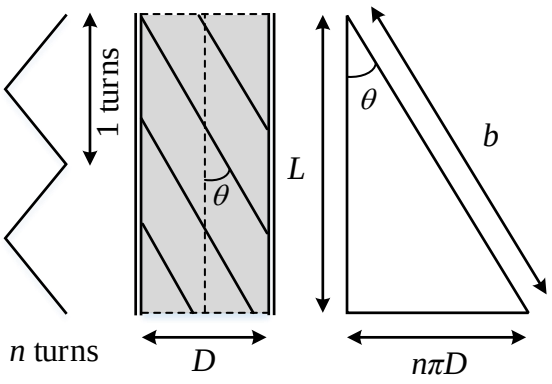


*Figure 3. A cross-sectional view of the simplified geometric model of PAM.*

The mathematical model of the PAM system is developed based on the geometrical properties and physical processes running inside the muscle. The major characteristics of the PAM are the relation between pressure, force, volume, and length. Specifically, the most often mentioned characteristic of the PAM is the force as a function of the pressure and a length-contraction. The PAM used in the work is a cylindrical artificial muscle from braided fibers with zero or nonzero wall thickness. The basic parameters of the PAM are shown in Figure 3, which are muscle length $L$, the diameter of the muscle $D$ and the initial angle $\theta$ between the axis of the muscle and fibers, the length of single knitted fibers mesh shell $b$, and the winding turns of fibers $n$.

The actual length $L$ and actual diameter $D$ are expressed as functions of the initial angle $\theta$ as follows:

$$L = b\cos\theta \tag{1}$$

$$n\pi D = b\sin\theta \tag{2}$$

The volume of a cylinder with zero wall thickness is expressed as a function of the muscle diameter and valve diameter as follows:

$$\Delta V = \frac{\left(b^2 - L^2\right)L}{4\pi n^2} \tag{3}$$

According to the principle of conservation of energy and assuming that there is no energy loss in the actuator, the tensile force can be calculated as [7]:

$$F = -P\frac{d\Delta V}{dL} = -P\frac{dV/d\theta}{dL/d\theta} = -P\frac{b^2 - 3L^2}{4\pi n^2} \tag{4}$$

The length $L$ can be expressed as a function of $x$:

$$L = \begin{cases} L_0 - x \ \ for\ PAM_1 \\ L_0 + x \ \ for\ PAM_2 \end{cases} \tag{5}$$

where $L_0$ is the initial length of a PAM.

In fact, two proportional valves integrated inside the pressure regulators were used to regulate the pressure of the compressed air supplied into the PAMs. Consequently, the position is obtained through the antagonistic control of the pressure of the pair of the PAMs. A positive/negative motion of the plate requires an increment/decrement of the pressure $P_1$ of the PAM 1 and a decrement/increment of the pressure $P_2$ of the PAM 2. Therefore, the antagonistic actuation can be described by:

$$\begin{cases} P_1 = P_0 + \Delta P \\ P_2 = P_0 - \Delta P \end{cases} \tag{6}$$

where $P_0$ is the initial pressure and $\Delta P$ is the pressure difference from $P_0$ used as a manipulated variable in the antagonistic pressure control. It is useful to note that the antagonistic strategy can simplify the motion control, since only one control variable, the pressure difference $\Delta P$, is used for the actuation of the motion through a pair of the PAMs in an antagonistic configuration. The pressure difference $\Delta P$ is the control input of the closed-loop system, i.e., $u = \Delta P$. Each PAM geometric force is formulated as the gauge relative pressure $\Delta P$ multiplied by the change in volume concerning length, respectively.

$$F_1 = \left(P_0 + \Delta P\right)\left(\frac{3\left(L_0 - x\right)^2 - b^2}{4\pi n^2}\right) \tag{7}$$

$$F_2 = \left(P_0 - \Delta P\right)\left(\frac{3\left(L_0 + x\right)^2 - b^2}{4\pi n^2}\right) \tag{8}$$

where $F_1$ and $F_2$ express the contraction forces of the two PAMs, $x$ is the mechanism position. Hence, the motion equation of the system can be written as the following nonlinear second-order equation.

$$M\ddot{x} + C\dot{x} = F_1 - F_2 + \Delta \tag{9}$$

where $M$ is the mass of the plate, $C$ is the viscous damping coefficient, $\Delta$ is the total of unknown disturbances in the system dynamics, which includes external perturbations, e.g., load variations or disturbance torque, and friction nonlinearities.

Substituting (7), (8) into (9), the load dynamics of the system can be presented as:

$$\ddot{x} = f(x, \dot{x}) + g(x)u + \Delta \tag{10}$$

where $f(x) = -\frac{3P_0L_0x}{\pi n^2 M} - \frac{B\dot{x}}{M}$ and $g(x) = \frac{3\left(L_0^2 + x^2\right) - b^2}{2\pi n^2 M}$.

Let us define $f_0(x)$, $g_0(x)$ are the nominal values of $f(x)$ and $g(x)$, respectively. Thus the equation (10) can be rewritten as the following.

$$\ddot{x} = f_0(x, \dot{x}) + g_0(x)u + d \tag{11}$$

where $d = (f(x, \dot{x}) - f_0(x, \dot{x})) + (g(x) - g_0(x))u + \Delta$. Let $x_1 = x$ and $x_2 = \dot{x}$, then the equation (11) can be transformed as:

$$\begin{cases} \dot{x}_1 = x_2 \\ \dot{x}_2 = f_0\left(x_1, x_2\right) + g_0\left(x_1\right)u + d \end{cases} \tag{12}$$

**Remark 2.1***: It is noted that $g_0(x_1) > 0$ with $x_1 \in \mathbb{R}$.*

**Assumption 2.1***: The lump disturbance d is bounded by the following inequation.*

$$d \le \delta_d \tag{13}$$

*where $\delta_d$ is a positive constant.*

The model response and the system response corresponding to a chirp signal are depicted in Figure 4. Obviously, the system model can fairly illustrate the complicated response of the real system, i.e., the hysteretic behavior. Figure 5 shows the nonlinear term $d(t)$ in (11) and its TDE error. It can be seen that the TDE is capable to estimate the nonlinearity and disturbance in the PAM system.

*Table 1. Parameters of The Studied PAM Model.*

| Parameter | Description | Value | Unit |
|---|---|---|---|
| $P_s$ | Supply pressure | 6.5 | bar |
| $C$ | Viscous damping coefficient | 50 | N.s/mm |
| $M$ | Mass of the plate | 0.5 | Kg |
| $L_0$ | Original length of the PAM | 175 | mm |
| $n$ | Number of turns of the thread | 1.04 | |
| $b$ | Thread length | 200 | mm |

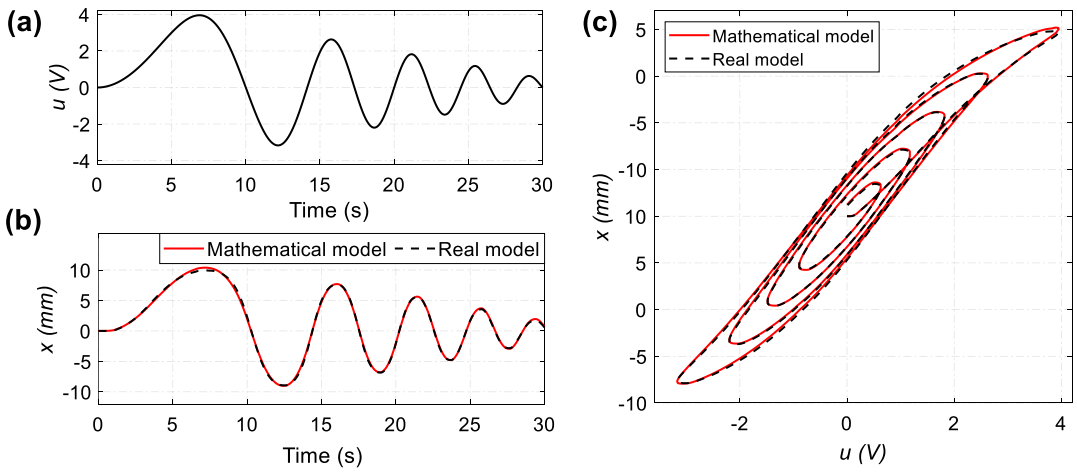


*Figure 4. Response of the PAM system. (a, b) Open-loop control, (c) Hysteresis curve.*

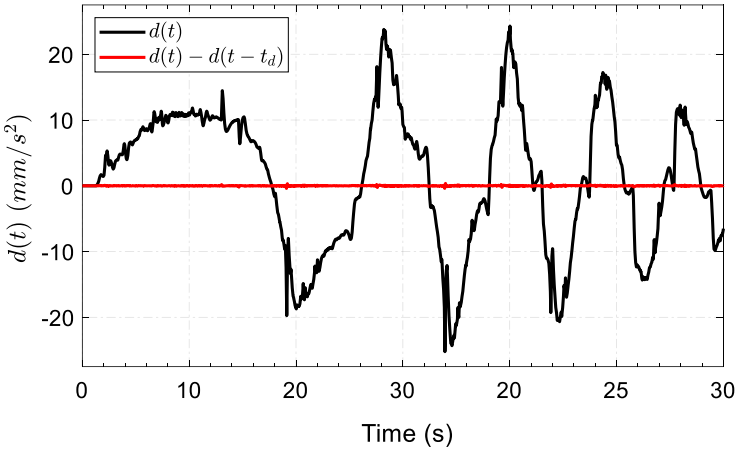


*Figure 5. Response of d(t) and time-delay estimation error.*

## 2.2 Experimental modeling

For determining the nonlinear model of the PAM, the theoretical models of the PAMs were presented in [7, 9] which described the major characteristics of the PAM are the relation between pressure, force, volume, and length. Besides, the phenomenological models of PAMs were investigated in [8, 13, 14] which express the output force as a function of pneumatics' pressure and kinematics. In this study, the three-element phenomenological model considering the hysteresis phenomenon presented in [14] is adopted to describe the dynamics of the PAM.

*Table 2. List of APAM model parameters.*

| | Parameter | Value | Units |
|---|---|---|---|
| Spring elements | $k_{k1}$ | 117.32 | N/m/bar |
| | $k_{k0}$ | 6.8 | N/m |
| Damping elements | $b_{k1}$ | 96.2 | N/m/s/bar |
| | $b_{k0}$ | 0.85 | N/m/s |
| Force elements | $f_{k1}$ | 91.22 | N/bar |
| | $f_{k0}$ | 4.73 | N |

The expression of the approximated force exerted by a single PAM based on its pressure and contraction strain follows the constitutive laws.

$$M_k\ddot{\xi}_k + b_k(P_k)\dot{\xi}_k + k_k(P_k)\xi_k = f_k(P_k)$$
$$\begin{cases} b_k(P_k) = b_{k1}P_k + b_{k0} \\ k_k(P_k) = k_{k1}P_k + k_{k0} \quad (k=1,2) \\ f_k(P_k) = f_{k1}P_k + f_{k0} \end{cases} \tag{14}$$

where $M_k$, $\xi_k$, $P_k \in \mathbb{R}^n$ are the mass of load, the displacement and air pressure of the $k^{\text{th}}$ PAM, respectively; $b_k(P_k)$, $k_k(P_k)$, and $f_k(P_k)$ are the damping coefficient, stiffness, and the contraction force of the $k^{\text{th}}$ PAM, respectively; $b_{k1}$, $b_{k0}$, $k_{k1}$, $k_{k0}$, $f_{k1}$, and $f_{k0}$ are the coefficients of the model

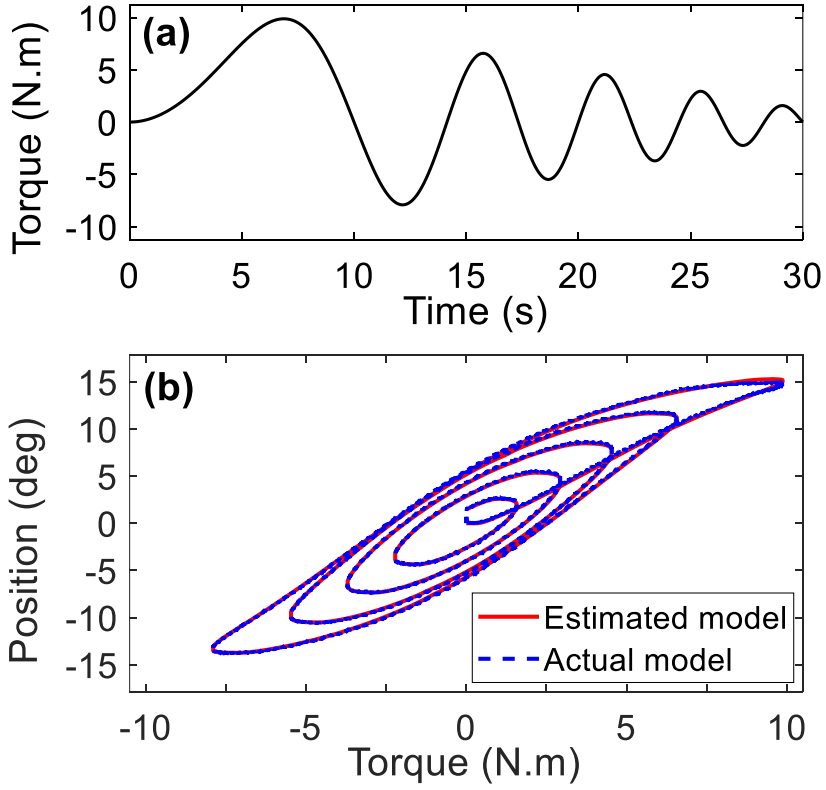


*Figure 6. Response of the APAM system. (a) the chirp control signal, (b) Hysteresis curve.*

parameters, as shown in Figure 7. The specification parameters of the APAM model are given in Table 2. Figure 6 expresses the open-loop responses of the model and the real APAM system with respect to a chirp control input signal of the frequency of 0.01 Hz and the reducing amplitude by the function $4\pi \times (1 - 0.03t)$ via sampling time $t$. As can be seen in this figure, the dynamics model described in (14) can fairly represent the high nonlinearity of the real system with small estimation error.

### 2.3 The BHTS modeling

In fact, two proportional valves integrated inside the pressure regulators were used to regulate the pressure of the compressed air supplied into the PAMs. Consequently, the position is obtained through the antagonistic control of the pressure of the pair of the PAMs. A positive/negative motion of the plate requires an increment/decrement of the pressure $P_1$ of the PAM 1 and a decrement/increment of the pressure $P_2$ of the PAM 2. Therefore, the antagonistic actuation can be described by:

$$P_1 = P_0 + \Delta P, \qquad P_2 = P_0 - \Delta P \tag{15}$$

where $P_0$ = 3 bar is the initial pressure and $\Delta P$ is the pressure difference from $P_0$ used as a manipulated variable in the antagonistic pressure control. In the APAM system, the two PAMs

*Table 3. Specifications of the experimental devices.*

| Device | Description |
|---|---|
| PAM | Type: Festo MAS-10-200N-AA-MC-O<br>Nominal length: 200 mm<br>Inside diameter: 10 mm<br>Max pressure: 8 bar |
| PPR Valve | Type: Festo VPPM-8L-L-1-G14-0L8H-V1N<br>Max pressure: 8 bar |
| DAQ Card | ADVANTECH PCI-1711<br>AI/AO: 12 bits (resolution)<br>MEASUREMENT PCI-QUAD04 |
| Loadcell | Model: CDFSA<br>Rated capacity: 100 kg<br>Rated output: 1.0 mV/V |
| Rotary encoder | Type: E40H12-1024-3-V-5<br>Resolution: 1024 pulses |

are connected by a rod and through a pulley with a radius of $r$ = 0.025 m. Given two contraction forces, one from each muscle, the torque $\tau$ of the actuated joint reads

$$\tau = \tau_1 - \tau_2 = r(f_1 - f_2) \tag{16}$$

where $\tau_1$ and $\tau_2$ are the torques generated by each PAM.

The total torque can be expressed in terms of the joint angle $\theta$, using the kinematic relations

$$\theta = \left(\xi_1 - \xi_2\right)/r \tag{17}$$

Hence, the dynamic of the robot can be written as the following nonlinear second-order equation.

$$M\ddot{\theta} + C\dot{\theta} + K\theta + \tau_d = \tau - \tau_e \tag{18}$$

where $M = M_k r^2$, $C = (\zeta + 2r^2(b_{11}P_0 + b_{10}))$, $K = 2r^2(k_{11}P_0 + k_{10}))$, $\zeta$ = 0. 052 N.s/m is the viscous damping coefficient, $\tau$ is the vector of generalized joint coordinates, $\tau_d \in \mathbb{R}^n$ is a general nonlinear disturbance, $\tau_e \in \mathbb{R}^n$ is the external torque and $M_k$ denotes the link inertia which is estimated of inertia amounts to 0.032 kg.m$^2$. This value can be obtained from the CAD 3D model of the robot after specifying the materials of the parts of the model. The dynamic model of 1 DOF master and slave system based on APAM for the haptic system is given as follows

$$M_m\ddot{\theta}_m + C_m\dot{\theta}_m + K_m\theta_m = \tau_m - \tau_{md} \tag{19}$$

$$M_s\ddot{\theta}_s + C_s\dot{\theta}_s + K_s\theta_s = \tau_s - \tau_{sd} \tag{20}$$

where $m$ and $s$ denote the master and slave side, respectively. Let $i$ denotes $m$ or $s$, in (19) and (20). $\theta_i(t), \dot{\theta}_i(t), \ddot{\theta}_i(t)$, represents the joint position, velocity and acceleration, respectively. $\tau_i(t)$ is the applied control torque and $\tau_{id}(t)$ denotes the external torque, for $i = m, s$. According to [15], one of the fundamental properties of the bilateral teleoperation systems (19) and (20), matrices $\dot{M}_i - 2C_i$ are skew-symmetric.

### 2.4 Platform setup of the BHTS

In order to validate the genuine perspective on the efficiency of the proposed methods, the experimental testbench is established, in turn, CAD design in Figure 8, the slave and environment in Figure 9, the overview BTHS setup in Figure 10. The bilateral teleoperation system consists of two similar manipulators, a control stick for interaction with a human operator, and an environment test bench modeled by an adjustable spring structure and a damper. Each manipulator is actuated by a pair of PAMs (MAS-10-200N-AA-MC-O by Festo company) antagonistically connected through a pulley of radius 0.025 m. The length of each PAM at rest is 0.2 m. The control pressures of both master and slave systems are achieved by

two proportional pressure regulator valves (VPPM-8L-L-1-G14-0L8HV1N by Festo company). To obtain the joint position of the manipulators, two optical rotary encoders (E40H12-1024-3-V-5 by Autonis company) with a resolution of 1024 pulse/rev are mounted on the joint structures. Besides, pressure sensors integrated inside the pressure regulators are utilized to obtain the pressure information of the PAMs. The human interacting torque is measured by a torque sensor (Bongshin CDFSA) in the master system. Meanwhile, the interaction force of the slave manipulator with the environment is determined by a force sensor, which is installed in the environment unit. The specifications of the testing devices are shown in

Table 3. The overall experiment validation section is evaluated the effectiveness of the proposed control algorithm in the real test bench based on a real-time Windows target toolbox on the MATLAB-Simulink environment. The sampling time t of the real-time process is chosen to be 0.005 second.

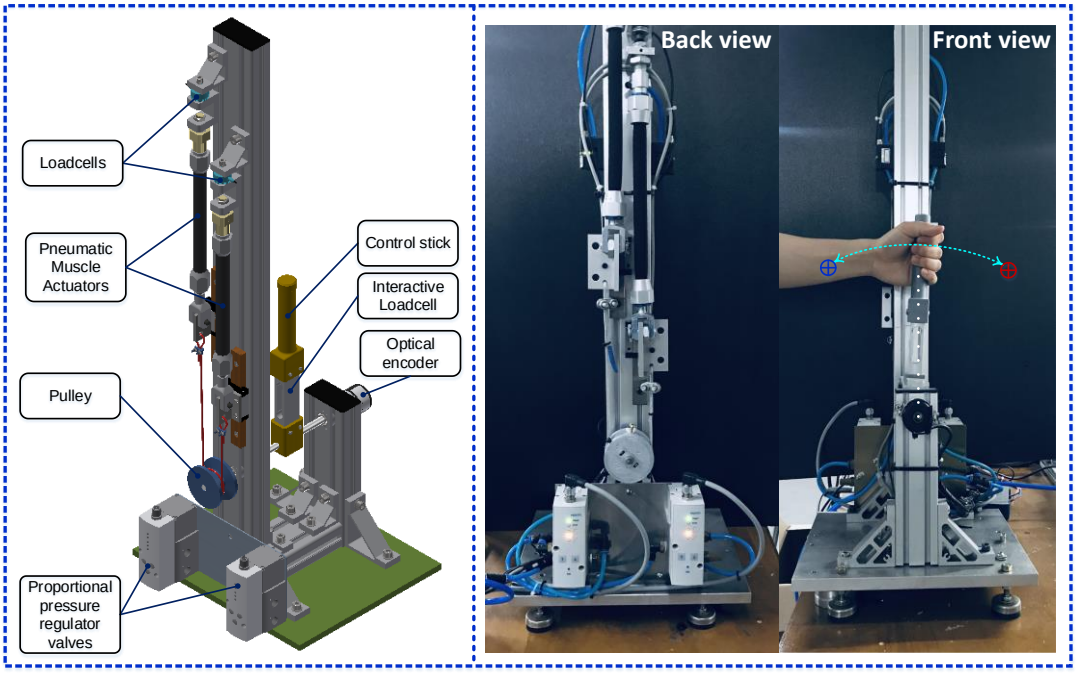


*Figure 8. The 3D CAD design and the test rig setup of the master system.*

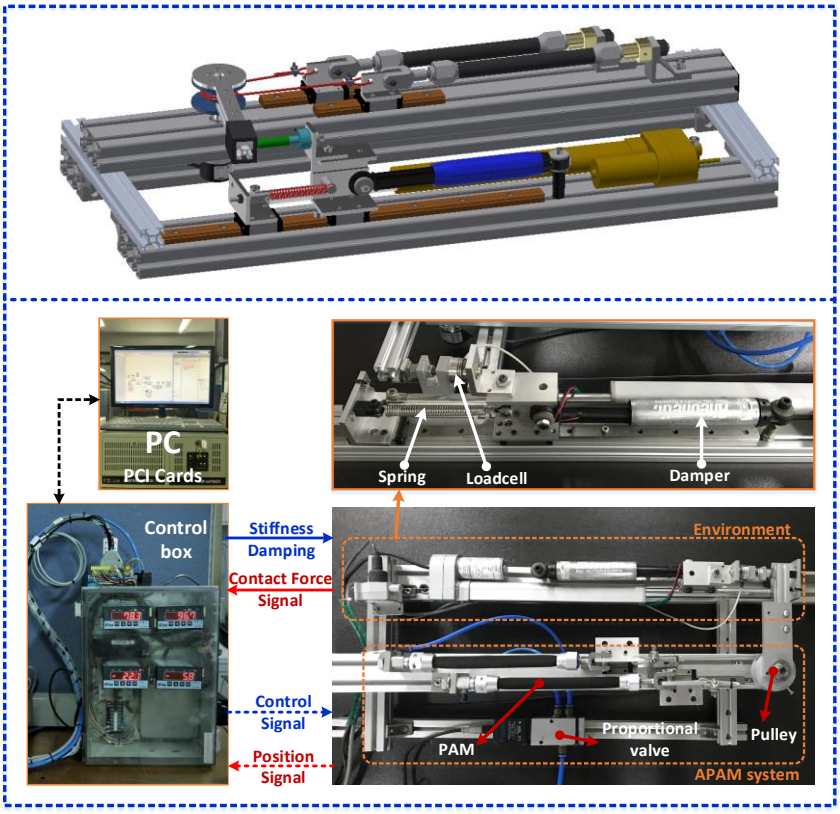


*Figure 9. The 3D CAD design and the test rig setup of the slave system.*

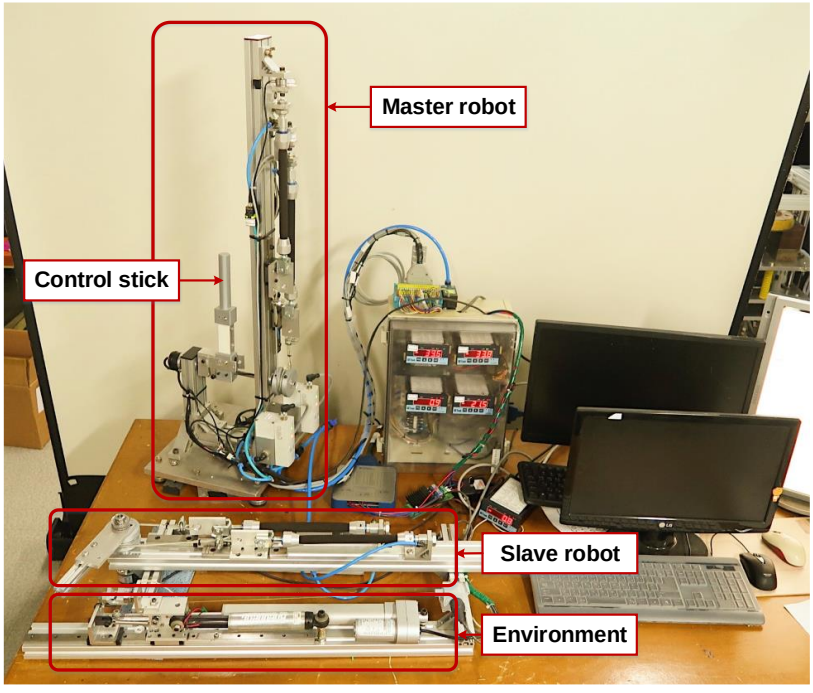


*Figure 10. Photograph of the experimental apparatus of the overview BHTS.*

# Chapter 3

# ADAPTIVE GAIN INTEGRAL TERMINAL SLIDING MODE CONTROL SCHEME OF A APAM SYSTEM BASED ON TDE

## 3.1 Introduction

### 3.2.1 Overview

In order to achieve high tracking accuracy for the PAM system, various control strategies have been presented recently. Advanced Proportional-integral-derivative (PID) controllers have been commonly used for the PAM system such as a nonlinear PID controller combined with a neural network scheme [16], an advanced nonlinear PID controller [17]. Nevertheless, the efficiency of such control schemes is limited only to a specific region since their weak robustness against high nonlinearity and time variation of system parameters. To overcome this drawback, model-based control strategies have been developed recently for the PAM system [18, 19]. The work in [18] developed a model-based cascaded sliding mode control (SMC) and Ba and Ahn [19] designed an indirect SMC based on an online identification scheme for estimation of the internal functions of the PAM dynamics. However, external disturbances have not been fully discussed in these works. To cope with this problem, an adaptive backstepping sliding mode control technique was used to control a PAM-based robot with a disturbance observer utilized to estimate and compensate the uncertainties and disturbance in the system dynamics in [20]. Notwithstanding, such control schemes only guarantee the asymptotical convergence of the tracking errors.

It is worth noting that the finite-time stability can enhance the steady-state tracking accuracy of the nonlinear systems. Thus, a finite time sliding mode algorithm namely terminal sliding mode control (TSMC) has been introduced and applied in various control problems [21-29]. Compared to the traditional linear sliding surface, the nonlinear sliding surface in TSMC can provide some advanced characteristics such as fast transient response, high steady-state tracking performance and finite-time convergence of tracking errors. As with the SMC, the TSMC comprises of two phases, the system is forced to reach the sliding surface in the reaching phase in a finite time and is kept staying there in the sliding phase. However, the presence of the reaching phase could

degrade the performance of the TSMC thanks to the lack of robustness against disturbances at the beginning [30].

Besides, it is worth pointing out that most of all above-mentioned types of the SMC need the prior information of the bounded value of the disturbance. One of the significant methods is to estimate the uncertainty and disturbance in the system to solve that problem. A variety of intelligent approaches were presented to seek suitable estimation strategies for the nonlinear systems such as adaptive fuzzy controller [31-33], neural network [34], adaptive control [35, 36] and radial basis function neural network [37]. Nonetheless, the above approaches require complex algorithms or a large number of tuning parameters and depend largely on the experience of experts, while most of the PAM applications require controllers with easy practical implementation. Therefore, the controller is employed with a simple model based on time-delay estimation (TDE). The choice of use of TDE is that it can estimate the unknown dynamics with a simple control scheme and effectively cancel the nonlinear dynamics of the PAM system. The TDE, however, cannot estimate accurately the uncertainties in the system dynamics in the real experiments due to measurement noise and nonlinear behaviors. Therefore, the robust control gain must be sufficiently large to attenuate the time delay estimation error.

### 3.2.2 The proposed control scheme for the PAM system

To deal with the aforementioned problems, this chapter proposes a novel adaptive gain ITSMC with TDE scheme for the PAM system. The main components of the proposed control scheme are a nominal control scheme, an uncertainty estimator, and a discontinuous robust control scheme. In the nominal control scheme, a novel backstepping TSMC (BTSMC) scheme is designed with the nonlinear sliding surface that can provide outstanding features such as fast transient response, high steady-state tracking performance and finite-time convergence of tracking errors. Meanwhile, a novel ITSMC scheme with an adaptive gain is designed in the discontinuous control scheme. In this design, the integral term in the sliding function could ensure the system starts in the sliding manifold in an initial period of time to avoid the effect of the reaching phase, which may degrade the effectiveness of the terminal sliding mode control at the beginning [38, 39]. For estimation of the nonlinearity and disturbance in the system, a time-delay estimation technique is employed, which becomes the third component in the final control signal and makes the controlled system become model-free. Moreover, an adaptation gain for the ITSMC scheme is proposed to estimate the ideal robust gain, which is just enough to compensate for the estimation error and thereby reducing the chattering phenomenon in the control signal.

Comparing to the existing approaches, the main contribution of this work can be summarized as follows:

- To the authors' best knowledge, there are no approaches for the control of PAMs using the ITSMC. Moreover, this work proposed for the first time the hybrid control based on ITSMC and TDE. The objective of this work is to investigate the interesting above-mentioned properties of the proposed approach.
- Compared to the conventional integral SMC, a novel ITSMC robust control scheme with adaptation gain and TDE based uncertainty estimator are developed to attenuate the chattering of the control signal.
- The stability and finite-time convergence characteristic of the controlled system are theoretically analyzed by the Lyapunov theory and experimentally demonstrated in different challenging work conditions.

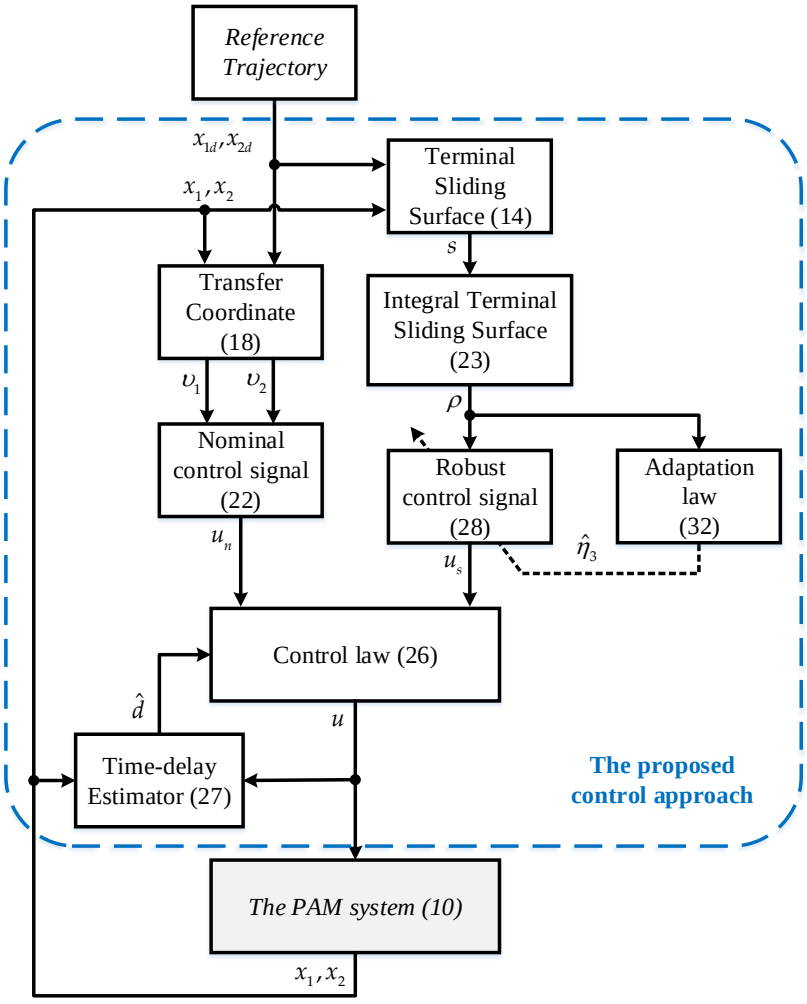


*Figure 11. Structure of Adaptive Gain ITSMC with TDE scheme.*

### 3.2 Proposed control description

In this section, the adaptive gain ITSMC is developed for the PAM system (18) to guarantee the finite-time convergence of the tracking errors in the presence of uncertainties and disturbances. The structure of the designed control algorithm is shown in Figure 11. The proposed control scheme is structured from a combination of a continuous nominal control scheme, a discontinuous robust control scheme and a TDE based uncertainty estimator. The nominal control system consists of a transfer coordinate block to change the variable coordinate and a backstepping terminal sliding model-based control block, which is designed to guarantee the robust performance of the nominal system. The uncertainty and disturbance in the system dynamics are approximated using the TDE technique, whereas the robust control system is comprised of two filtered blocks to calculate the integral sliding surface and a robust control block with adaptive gain to deal with the uncertainties and disturbance in the controlled system. The detail of the designed control approach is presented as the following

#### 3.2.1 The Integral Terminal Sliding Mode Controller

The goal of this section is to develop a control scheme based on the integral terminal sliding mode control such that the state variables $x_1$ and $x_2$ can track their corresponding reference values $x_{1d}$ and $x_{2d}$ accurately. Let the tracking error defined as $e_1 = x_1 - x_{1d}$ and $e_2 = x_2 - x_{2d}$, then a terminal sliding surface is chosen as:

$$s = e_2 + k_1 e_1 + k_2 e_1^{\alpha} \tag{21}$$

where $\alpha = \alpha_1/\alpha_2$, $\alpha_1$ and $\alpha_2$ are positive odd integers satisfying the relation [40], $0 < \alpha_1/\alpha_2 < 1$, $k_1$ and $k_2$ are designed positive constants. Taking the derivative of (21), one obtains

$$\dot{s} = k_1 e_2 + \alpha k_2 e_1^{\alpha-1} e_2 + f_0(x_1, x_2) + g_0(x_1) u + d - \ddot{x}_{1d} \tag{22}$$

In the integral terminal sliding mode approach, the following form of the control signal is designed to guarantee the tracking accuracy of the nominal system and compensate the uncertainties and disturbances in the system

$$u(t) = u_n(t) + u_s(t) \tag{23}$$

where $u_n(t)$ denotes the nominal control signal, which is responsible for the performance of the nominal system, which is defined later, and $u_s(t)$ denotes the robust control signal which deals with the uncertainties and disturbances.

The nominal system of (11) is represented by the following form:

$$\begin{cases} \dot{x}_1 = x_2 \\ \dot{x}_2 = f_0(x_1, x_2) + g_0(x_1) u_n \end{cases} \tag{24}$$

The following step is designed as the control signal $u_n(t)$ to assure the finite-time convergence of the tracking error $e_1$ in the system (24). Firstly, the following auxiliary variables are defined:

$$\begin{cases} \upsilon_1 = e_1 = x_1 - x_{1d} \\ \upsilon_2 = x_2 - \beta_1 \end{cases} \tag{25}$$

The time derivative of the $\upsilon_1$ is computed as:

$$\dot{\upsilon}_1 = x_2 - \dot{x}_{1d} \tag{26}$$

Then virtual control signal $\beta_1(t)$ can be designed as:

$$\beta_1(t) = \dot{x}_{1d} - \eta_1 \upsilon_1 - \kappa_1 \upsilon_1^{\gamma_1} \tag{27}$$

where $\eta_1$ and $\kappa_1$ are positive designed parameters and $\gamma_1 = p_1/q_1$, where $p_1$ and $q_1$ are odd integers and $p_1 < q_1$. Taking the time derivative of the variable $\upsilon_2$, one obtains:

$$\begin{aligned} \dot{\upsilon}_2 &= \dot{x}_2 - \dot{x}_{1d} + \eta_1 \dot{\upsilon}_1 + \kappa_1 \gamma_1 \upsilon_1^{\gamma_1 - 1} \dot{\upsilon}_1 \\ &= f_0(x_1, x_2) + g_0(x_1) u_n - \ddot{x}_{1d} + \eta_1 \dot{\upsilon}_1 + \kappa_1 \gamma_1 \upsilon_1^{\gamma_1 - 1} \dot{\upsilon}_1 \end{aligned} \tag{28}$$

Therefore, the nominal control signal $u_n(t)$ can be designed as:

$$u_n = \left(g_0(x_1)\right)^{-1} \left[ \ddot{x}_{1d} - \upsilon_1 - f_0(x_1, x_2) - \eta_1 \dot{\upsilon}_1 - \kappa_1 \upsilon_1^{\gamma_1 - 1} \dot{\upsilon}_1 - \eta_2 \upsilon_2 - \kappa_2 \upsilon_2^{\gamma_2} \right] \tag{29}$$

where $\eta_2$ and $\kappa_2$ are positive designed parameters and $\gamma_2 = p_2/q_2$, where $p_2$ and $q_2$ are odd integers and $p_2 < q_2$.

**Theorem 3.1:** *For the system described in* (24), *the transferred coordinate defined in* (25), *the virtual signal* $\beta_1(t)$ *designed as* (27), *and the control signal designed as* (29), *then the tracking error* $e_1(t)$ *can converge zero in a finite time*.

**Proof:** *See in Appendix* 3.1.

In order to achieve the robustness of the control system against uncertainties and disturbances, the objective of the following step is to design an appropriate robust control signal $u_s(t)$. Motivating from the integral type sliding mode control design in [41], the proposed integral sliding surface is designed as follows:

$$\rho = s(t) - s(t_0) - \int_{t_0}^{t} \left( k_1 e_2 + \alpha k_2 e_1^{\alpha - 1} e_2 + f_0(x_1, x_2) + g_0(x_1) u_n - \ddot{x}_{1d} \right) d\tau \tag{30}$$

In the above integral sliding surface formula, the presence of the additional integral term results in a higher degree of freedom in the design of the proposed control algorithm than traditional terminal sliding mode control. In addition, the term of $-s(t_0)$ provides an interesting characteristic that $\rho(t_0) = 0$, such that the reaching phase is removed. Therefore, the proposed control system achieves greater robustness than the traditional terminal sliding mode with the reaching phase. Then the robust control signal $u_s(t)$ is selected as

$$u_s(t) = -\left(g_0(x_1)\right)^{-1}\left[\eta_3 sign(\rho) + \kappa_3\rho + \kappa_4\rho^{\gamma_3}\right] \quad (31)$$

where $\kappa_3$ and $\kappa_4$ are positive designed parameters, $\eta_3 \geq \delta_d$, $\gamma_3 = p_3/q_3$, where $p_3$ and $q_3$ are odd integers, and $p_3 < q_3$.

**Theorem 3.2***: Considering the system defined in* (12) *satisfying Assumption* 2.1 *the terminal sliding surface chosen as* (21)*, the integral sliding surface designed as* (30)*, and the robust control signal is designed as* (31)*, then the system is finite-time stable*.

**Proof***: See in Appendix* 3.2.

In practice, it is difficult to determine the value of $\delta_d$. Thus, in the conventional sliding mode control, the robust control gain $\eta_3$ is selected to be large to compensate for the lump disturbance. However, a large control gain in the discontinuous signal in (31) leads to a large chattering phenomenon in the final control signal, which could harm the actuator system. Therefore, a time delay scheme and an adaptive gain scheme are developed in the next section to solve this problem

### 3.2.2 The Proposed Adaptive Gain ITSMC with TDE

It is quite intricated and time-consuming to obtain the estimation of the nonlinearity $d(t)$ using traditional methods for such systems with complex and time-varying uncertainties and disturbances. Hence, the TDE scheme is utilized to estimate the nonlinear term $d(t)$ in a simple way. As the time delay $t_d$ is chosen to be adequate small, the following condition is satisfied:

$$d(t) \cong d(t - t_d) \quad (32)$$

Therefore, the control law for the PAM system can be rewritten as the following:

$$u(t) = u_n + u_s - g(x_1)^{-1}\hat{d} \quad (33)$$

where the nominal control signal $u_n$ is designed as in (28), $\hat{d}$ is the estimation of the nonlinear term $d(t)$ and can be calculated as:

$$\hat{d} = d(t - t_d) = \dot{x}_2(t - t_d) - f_0\left(x_1(t - t_d), x_2(t - t_d)\right) - g_0\left(x_1(t - t_d)\right)u(t - t_d) \quad (34)$$

In reality, the disturbance $d(t)$ is hard to approximate accurately even for a small-time period $t_d$ due to the measurement noise and nonlinearity characteristic. Thus, the time delay estimation error $\varepsilon_d = d - \hat{d}$ exists and degrades the robustness of the controlled system. To overcome this problem, the robust control signal $u_s(t)$ can be redesigned as follows:

$$u_s(t) = -\left(g_0(x_1)\right)^{-1}\left[\hat{\eta}_3 sign(\rho) + \kappa_3\rho + \kappa_4\rho^{\gamma_3}\right] \quad (35)$$

where $\hat{\eta}_3$ is the estimation value of the robust control gain $\eta_3$. Assuming that the time delay estimation error is bounded by $|\varepsilon_d| \leq \vartheta$, where $\varepsilon_d$ denotes a positive value. The proof of the boundedness of $\vartheta$ is provided in Appendix 3.3. In order to guarantee the stability of the control system, the following adaptive law for the robust control gain is designed:

$$\dot{\hat{\eta}}_3 = \frac{1}{\mu}\left|\rho(t)\right| \tag{36}$$

where $\mu > 0$ is the adaptation parameter. Basing on the Lyapunov stability criterion, the stability and finite-time convergence of the tracking error are proved in Appendix 3.3 to be guaranteed in spite of the presence of the uncertainties and disturbances.

**Remark 3.1**: *The proposed adaptive gain ITSMC in* (35) *and* (36) *is not ready for the practical implementation. Since the measurement noises and other non-idealities always occur in the real experiments, it is very hard to ensure the integral sliding surface* $\rho(t) = 0$. *Therefore, the adaptive law for the robust gain described in* (36) *is modified as follows:*

- *If* $|\rho(t)| \geq \delta > 0$, *then* $\hat{\eta}_3(t)$ *is the solution of the equation* (36).
- *Otherwise,* $\hat{\eta}_3(t)$ *is given as the following.*

$$\hat{\eta}_3(t) = \hat{\eta}_3(t_m)\left|\chi\right| + \eta_0 \tag{37}$$

*where* $\delta$ *is the threshold value,* $\eta_0$ *is a positive value,* $t_m$ *is the largest time such that, by defining* $t_m^*$ *the time just before* $t_m$, $|\rho(t_m^*)| \geq \delta$ *and* $|\rho(t_m)| < \delta$, *and* $\chi$ *is the average value of the function sign*$(\rho(t))$, *which is given as:*

$$\sigma\dot{\chi} + \chi = sign\left(\rho(t)\right) \tag{38}$$

*where* $\sigma > 0$.

**Remark 3.2**: *Assuming that* $\rho(0) \neq 0$, *the updating law is shown in* (36), (37), *and* (38) *works as follows.*

- *While the condition* $|\rho(t)| \geq \delta > 0$ *exists, the adaptive gain* $\eta_3(t)$ *is increasing up to a value big enough to compensate the unknown bounded disturbances until reaching the sliding mode in the real experiment, as the condition* $|\rho(t)| < \delta$ *is met. Denoting the time instant when the sliding mode has been reached for the first time as* $t_1$.
- *In the sliding mode* $|\rho(t)| < \delta$, *the adaptive gain* $\eta_3(t)$ *is calculated following equation* (37) *and* (38), *with* $t_m = t_1$. *It is worth noting that the adaptive gain will be decreased and then adjusted with respect to the current uncertainties and disturbances.*

- *If the time-varying disturbance greater than the value $\eta_3(t_1)$, then the system is out of the sliding mode and the robust gain $\eta_3(t)$ is updated by following* (36)*, which is increasing until the condition $|\rho(t)| < \delta$ is met.*

**Remark 3.3:** *The robust gain $\eta_3$(t) has an upper-bound $\eta^*$, and there exists a finite time $t_F >$* 0 *so that the sliding mode is established, i.e., $|\rho(t)| < \delta$. The detail of the finite-time stability for the system using the updating law as in* (36), (37), *and* (38) *is given in* [38].

**Remark 3.4***: In order to reduce the chattering phenomenon, the sign function in* (34) *is replaced by the following saturation function.*

$$sat\left(\rho(t)\right) = \begin{cases} sign\left(\rho(t)\right) & if\ \left|\rho(t)\right| \geq \varepsilon_\rho \\ \rho(t)/\varepsilon_\rho & otherwise \end{cases} \tag{39}$$

*where $\varepsilon_\rho$ is a small positive real number.*

### 3.3 Experimental Validation

In this section, the effectiveness of the proposed controller is verified through various experimental tests on a real-time PAM system, which has been introduced in Section II. The system operating process is developed based on a real-time Windows target toolbox on the MATLAB-Simulink environment. The sampling time *t* of the real-time process is chosen to be 0.005 second. The performances of the proposed control approach are compared to those of a conventional PID controller, an ITSMC without the adaptation gain scheme, under the same working conditions. The parameters of the PID gains were initially turned by the Ziegler-Nichols method based on the stability boundary. The parameters of the PAM model are shown in Table 2. The parameters of the backstepping terminal sliding mode designed for the nominal system is chosen as $\eta_1 = 3$, $\eta_2 = 1.5$, $\kappa_1 = 10$, $\kappa_2 = 2$, $\gamma_1 = 5/7$, and $\gamma_2 = 5/7$. The parameters of the ITSMC are designed as $k_1 = 2$, $k_2 = 5.5$, $\alpha = 9/11$, $\eta_3 = 2.5$, $\kappa_3 = 10$, and $\kappa_4 = 2$. The adaptation gain scheme is designed with the following parameters $\mu = 10$, $\delta = 0.05$, $\sigma = 0.1$, and the remain parameters of the proposed controller are selected as the same as the ITSMC. It is obvious that smaller time delay $t_d$ will bring in a better estimation, therefore $t_d$ is usually selected as one or few sampling periods. In this work, the time delay parameter $t_d$ is selected equal to the sampling period *t*. In order to validate the effectiveness of the proposed control algorithm in the real test bench as seen in Figure 11, the following case studies are investigated.

1. A low-frequency sinusoidal trajectory with no load;
2. A high-frequency sinusoidal trajectory with no load;
3. A multistep trajectory with no load;

4. A high-frequency sinusoidal trajectory with two loading cases: 2-kg-mass and 7-kg-mass.

To conduct the effective verification of the proposed controller, the schematic of this actuation arrangement is illustrated in Figure 12, a pair of the PAMs is connected follow as the antagonistic configuration to create dragging to pull and push a plate along the linear guide in a working range of −10 to +10 mm. Additionally, controlled pressure is achieved by two proportional pressure regulator valves supplying compressed air two PAMs respectively. The pressure sensors, which are integrated inside the pressure regulators, provide a measurement accuracy of ±0.0035 bar. Besides, the displacement of the plate is measured horizontal axis through a linear encoder and provides measurement accuracy of ±0.005 mm. The control setup for the system is deployed as a standalone device using a PC programmable through a combined PCI-1711 card and QUAD-04 card. The specification of the experimental devices is listed in Table 3.

### 3.3.1 Case study 1

In the first case study, the reference trajectory was a sinusoidal signal with an amplitude of 8 mm and a frequency of 0.2 Hz. The parameters of the PID controller were selected as $K_p$ = 3.5, $K_i$ = 28 and $K_d$ = 0.1. The experimental results obtained by applying, in turn, the PID, TSMC, and proposed controller to the testing system are shown in Figure 13. The tracking performance of the comparative controllers, as well as zoom-in performances, are shown in the first graph,

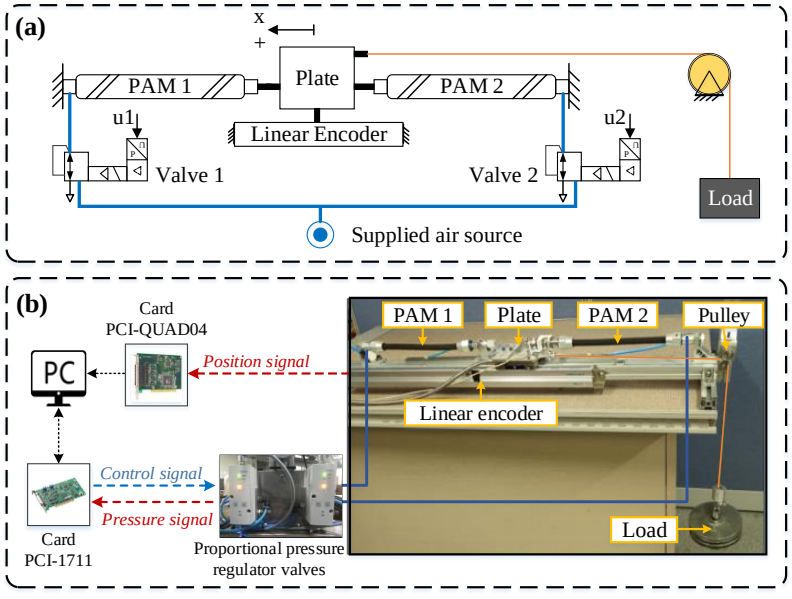


*Figure 12. (a) Working principle and (b) Configuration of the experimental system.*

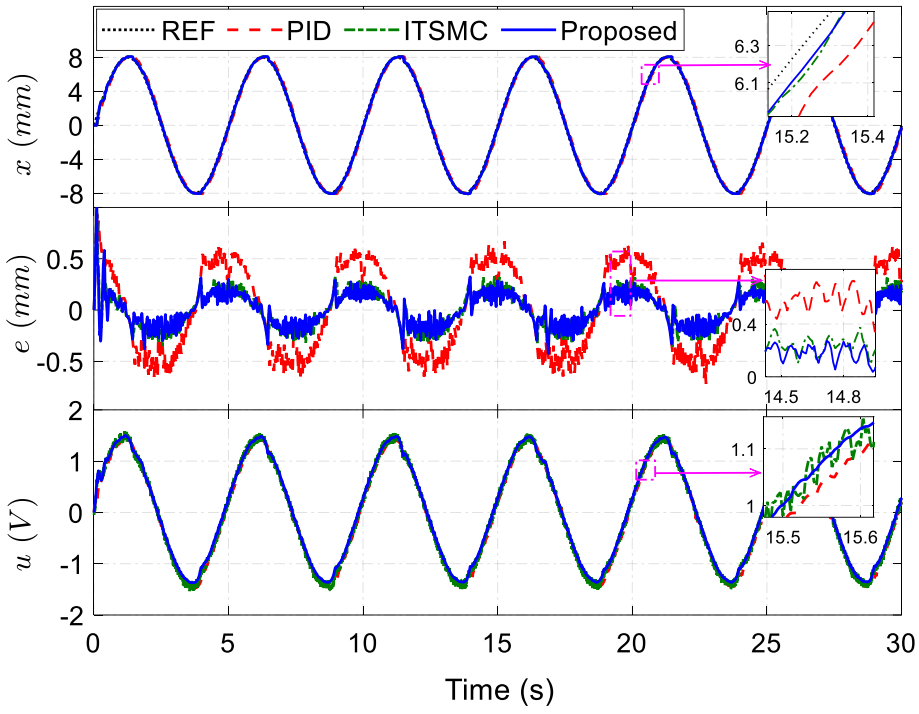


*Figure 13. Comparison of control performance with respect to case study 1.*

whereas the tracking errors and the control input signals are shown in the second and third graphs, respectively. As can be seen in Figure 13, the conventional PID controller provided a suitable control input to compel the system trajectory to its reference as closely as possible. Thus, an acceptable range of control error (±0.6 mm) was accomplished when employing the PID controller with a fixed gain. However, this controller gave the worst tracking performance due to its lack of robustness against nonlinearities or uncertainties. Meanwhile, with the robust control design, the ITSMC improved the control performances with much smaller tracking errors. The tracking errors of the ITSMC are mostly limited to an acceptable range of ±0.3 mm. Furthermore, the proposed controller algorithm provided better performance with the tracking errors mostly within ±0.25 mm. It can be observed that the proposed control signal is smooth as expected and has much less control chatters than that of the conventional ITSMC. It comes not only from the advantage of TDE but also from the use of the adaptation gain scheme, which can estimate the ideal robust gain of the discontinuous signal.

### 3.3.2 Case study 2

In order to further investigate the advantage of the designed control structure, a high-frequency sinusoidal signal with a frequency of 1 Hz and an amplitude of 8 mm is selected as a reference trajectory. The PID controller's gains were chosen as $K_p$ = 4.5, $K_i$ = 40 and $K_d$ = 0.1. Applying the PID controller, ITSMC, and the proposed control algorithm, the tracking performances,

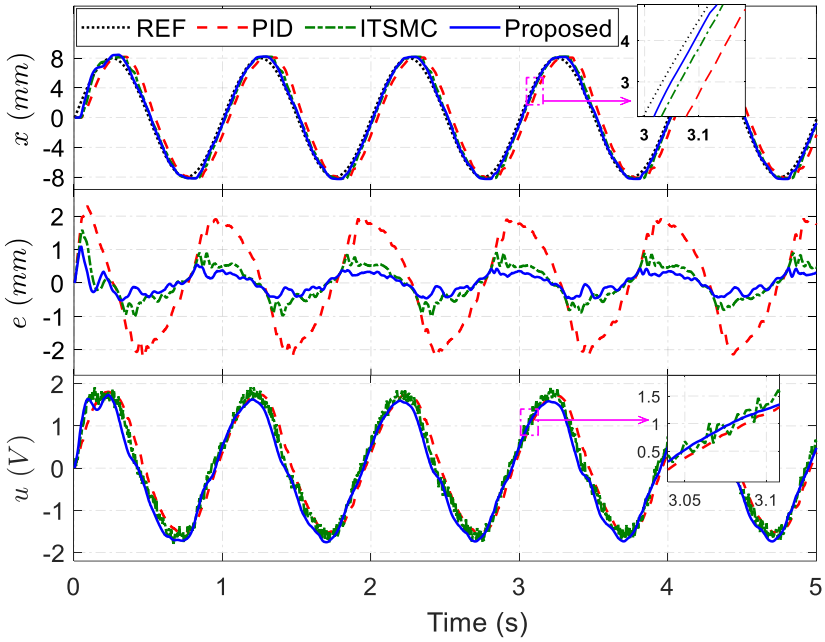


*Figure 14. Comparison of control performance with respect to case study 2.*

tracking errors, and control signals of the corresponding controllers are depicted in Figure 14. As shown in this figure, it is clear that the PID performance was significantly degraded with the bound of the tracking error with respect to 1 Hz sinusoidal reference nearly four times that of the case study 1, from 7.5% at 0.2 Hz to 30.8% at 1 Hz. Meanwhile, the ITSMC shows its better robustness performance with the bound of tracking errors increased from 3.8% at 0.2 Hz to 11.5% at 1 Hz. In contrast, the proposed controller still maintained its merit with the tracking errors is kept in a small range, 3.1% at 0.2 Hz and 8.1% at 1 Hz. With regard to the chattering phenomenons, it is shown that the chattering phenomenon was significantly attenuated in the proposed control signal compared to the ITSMC signal, whereas the excellent tracking performance was still ensured. This once again validates the advantage of the proposed control method.

### 3.3.3 Case study 3

In this case study, the comparative controllers are tested with a multistep reference trajectory to verify their performances with respect to the irregular tracking commands. The parameters of the PID controller were chosen as $K_p$ = 1.5, $K_i$ = 18 and $K_d$ = 0.05 for this case study. The comparison between the PID controller, ITSMC, and the proposed control algorithm with respect to the multistep reference signal is depicted in Figure 15. As can be seen in this figure, the response speed of the designed controller is better than those of ITSMC and the PID controller. The proposed controller provided the fast response with an average rise time is about 0.08 second

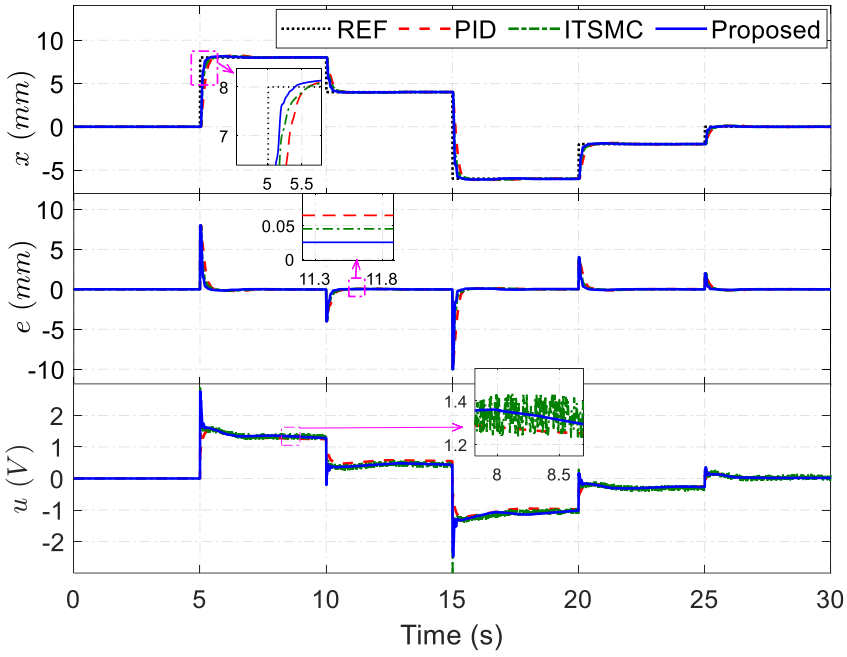


*Figure 15. Comparison of control performance with respect to case study 3.*

whereas those of ITSMC and PID controller are 0.15 second and 0.32 second, respectively. The proposed control algorithm also gave the best performance in terms of overshoot and settling time whereas the PID controller gave the worst. In addition, the average absolute values of steady-state errors of the PID controller and ITSMC are about 0.1 mm and 0.04 mm, respectively, whilst the bound of the tracking errors of the proposed controller are less than 0.02 mm. On the whole, the proposed control algorithm showed the best performance in the comparative controllers, with excellent tracking trajectory accuracy, fast response speed, small steady-state error, and abolished chattering behavior.

### 3.3.4 Case study 4

In order to investigate the robustness of the proposed control algorithm against external disturbances, a 2-kg-mass and 7-kg-mass, in turn, is attached to the plate through a pulley as seen in Figure 12. The reference trajectory is chosen as the same as in case study 2. The control performances of the comparative controllers in two loading conditions are shown in Figure 17. It can be seen in this figure that the PID controller became much worse in the loading condition, especially with 7-kg-load condition. The tracking errors of the PID controller in 2-kg-load condition and 7-kg-load condition were ±2.4 mm and ±3.2 mm, respectively. These results come from the lack of robustness of the PID control algorithm against the disturbance. Meanwhile, thanks to the robust control scheme, the tracking errors of the ITSMC were a little increased compared to the free-load condition, ±1.1 mm with 2-kg-load and ±1.22 mm with 7-kg-load.

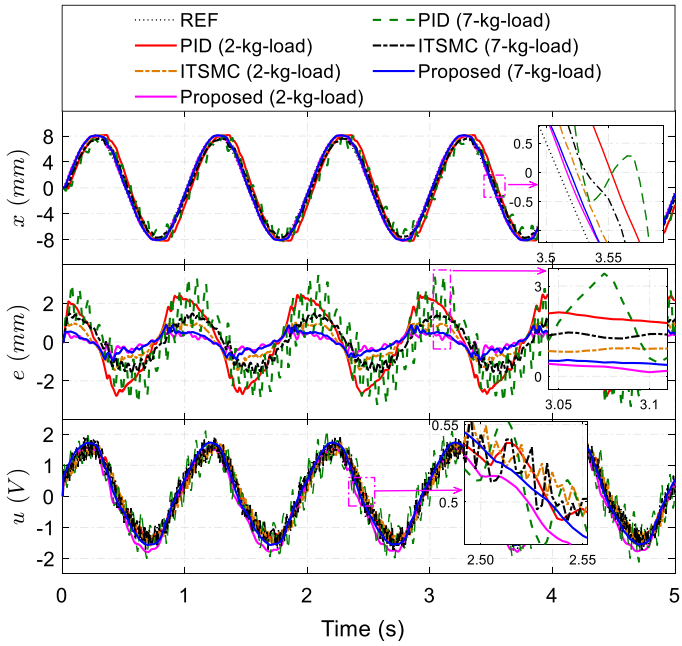


*Figure 17. Comparison of control performance with respect to case study 4.*

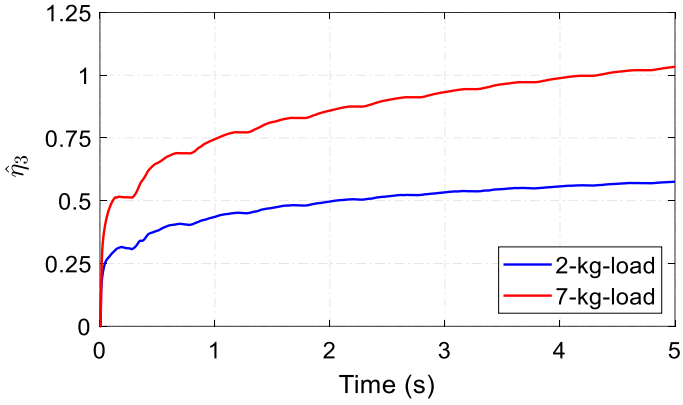


*Figure 16. Histories of robust control gain in the loading case study 4.*

However, the best performances were obtained by using the proposed control algorithm, which has both robust and adaptable properties. The results in Figure 17 show that the proposed control method always maintains the tracking errors within a small range (less than 0.8 mm) despite loading conditions. In addition, the chattering behavior of the proposed control signals in two loading cases was shown as tremendously less than that of ITSMC. This comes as no surprise from the advantage of the adaptation gain scheme (36), which estimates the ideal robust control gain to effectively compensate the disturbances in the system dynamics. The histories of the adaptive gains for the 2-kg-load condition and 7-kg-load condition are shown in Figure 16.

In order to a quantitative comparison between the tracking performances of the control strategies, the integral absolute error $(L_2[e] = \sqrt{\left(\int_0^T |e|^2 \, dt\right)/T})$ and control effort $(L_2[u] = \sqrt{\left(\int_0^T \|u\|^2 \, dt\right)/T})$ performance indices from the above-listed experiments are summarized in Table 4, where *T* is the total experimental time. As shown in this table, the effectiveness of the proposed control method is once again confirmed with the smallest tracking errors however the smallest control efforts in all experimental tests.

*Table 4. Performance indices of comparative controllers*

| Controller | | PID | ITSMC | Proposed controller |
|---|---|---|---|---|
| Sine 0.2 Hz – 8 mm | $L_2[e]$ | 0.4102 | 0.1737 | 0.1574 |
| | $L_2[u]$ | 0.9961 | 1.0270 | 0.9602 |
| Sine 1 Hz – 8 mm | $L_2[e]$ | 1.1845 | 0.4996 | 0.3788 |
| | $L_2[u]$ | 1.1284 | 1.1152 | 1.0900 |
| Multistep | $L_2[e]$ | 0.8587 | 0.6846 | 0.6368 |
| | $L_2[u]$ | 0.7670 | 0.7333 | 0.7247 |
| Sine 1 Hz – 8 mm with 2-kg-load | $L_2[e]$ | 1.2578 | 0.8314 | 0.4779 |
| | $L_2[u]$ | 1.1414 | 1.1506 | 1.1287 |
| Sine 1 Hz – 8 mm with 7-kg-load | $L_2[e]$ | 1.5937 | 1.0827 | 0.5067 |
| | $L_2[u]$ | 1.1613 | 1.1729 | 1.1584 |

## 3.4 Chapter summary

This work began with a review of the limitation of control algorithms developed for the PAM systems. Then, to overcome the drawbacks of the previous approaches and improve the tracking performance of the PAM systems, a new proposed controller has been presented. The idea of the designed control approach is to define the control law as a sum of a nominal control scheme and a robust control scheme. The nominal control algorithm is developed based on the backstepping terminal sliding mode algorithm to achieve the finite-time convergence of the controlled nominal system whereas the robust control scheme is derived to reject the effect caused by disturbances. From the comparison of the experimental scenarios, the proposed control method provided the following important properties: 1) Finite-time convergence of the tracking errors, 2) Eliminating the reaching phase, 3) Robust performance against uncertainties and disturbances in the system dynamics, 4) Reducing the chattering phenomenon by adaptation gain scheme, 5) Fast transient response. The effectiveness of the designed control algorithm is theoretically confirmed by Lyapunov stability theory and experimentally validated through superior performance to other control methods on a real PAM system.

# Chapter 4

# ADAPTIVE FINITE-TIME FORCE CONTROL SCHEME OF A APAM SYSTEM WITH TDE

## 4.1 Introduction

### 4.1.1 Overview

The vital roles of the robot applications in the manufacturing industry are increasingly demonstrated. With the deep participation in human society, control considering interactions with the environment is more expected. In several special duties, the robot is in contact with the unknown environment and works on them leading to appear an obscure variable force interaction. Additionally, some position-controlled robots may damage themselves, environments or humans that are collided to reach their desired positions. Therefore, measuring this interactive force is necessary for control, analysis, or decision purposes.

To start with, a compliant actuation is one of the viable components, such as series elastic actuators (SEA) [42] or variable stiffness actuators (VSA) [43] with passive spring systems in the joint, when considering elastic joints and no structural enforcement. More recently different pneumatic artificial muscle (PAM) systems have also been developed [4, 44, 45]. Inherently, they are high air-compliant, low weight to force ratio. In addition, they can store energy, demonstrate robust absorption of impact and require no gearing. From the perspective of control, impedance control is the most widely used method for force-sensitive control, dating back to Hogan's original work. [46]. It helps the robot to behave like a mass-spring-damper mechanism with respect to interaction forces in its most typical form. Therefore by choosing acceptable impedance settings, maximal contact forces can be constrained within the control bandwidth.

The precise regulation of contact forces is usually of great importance during grasping and manipulation, apart from compliant control. Generally, force control is split into direct and indirect force control [47]. Set-point movements that make use of the closed-loop impedance relationship are used by using impedance control to apply desired forces to artifacts and the environment. Since impedance control is not designed to control contact forces accurately, it is an indirect technique. Only through accurate knowledge of contact geometry and contact mechanics can precise force monitoring be achieved. A clear description of the stability analysis

of current direct force control methods using calculated or projected contact forces [48]. The approaches to stiffness and impedance control have been widely given in recent years for PAM actuators force [2, 3, 49]. However in the event of a sudden touch failure, when the compliance of the robot-environment interaction generates force, it may become potentially harmful. In addition, even those advanced force controllers have carried out a time problem in the generation of force can not be guaranteed, which can also affect the accuracy of the produced force.

In order to address the above limitations, an active compliant end-effector control has been employed to control the generated force, while the position control is developed on the robot or the numerical machine. Ma et al. [50] presented a 3-DOF parallel mechanism to generate force. An impedance control based PID technique was designed for force control of this mechanism. The force tracking error was still significant. Fan et al. [51] developed a novel end effector for active contact force control and vibration in the robot. A gravity-compensated force control-based PI control was applied to reach the contact force between the end-effector and the environment to the desired value. However, highly nonlinear properties in the PAM system, such as the dead-zone effect, the nonlinear friction force, and the compressibility of air, that will lead to uncertainties of the system. Consequently, the advanced controllers [52-54] have been developed to improve the control performance. Nonetheless, almost these researches [14-17] have been focused on position tracking issues.

Besides, the force sensing technique plays a vital role in such force control design since the control performance is affected by the precision of the force detection. In conventional approaches, the force information is obtained from force sensors [55]. However, the usage of force sensors has some drawbacks such as high cost, inconvenience to install, the capability of being damaged by impacts, and narrow bandwidth due to their sensitivity to noise. Hence, force observers have been designed to get force information in many approaches. Nonlinear disturbance observer (DO) is a well-known estimation method for external force and have been employed to estimate the force signal of the bilateral teleoperation system in [56]. In another approach presented in [57], both force and state information was estimated using an extended active observer to eliminate the effect of parameter uncertainties and measurement noise in the control performance. An extended state observer with an adaptive gain was also designed to obtain the force and state information without using force sensors in the bilateral teleoperation system in [58]. Even though these observers provide a simple way to estimate the external force, their disadvantage is that the effects of noise due to velocity computation could deteriorate the

force sensing. To handle this issue, the combination of force observer with a Kalman filter was introduced in [59]. Moreover, the *dithering* strategy is integrated with the wideband disturbance observer and Kalman filter to eliminate the effect of static friction in the performance of the force-sensing [60]. However, the Kalman filter cannot guarantee the finite-time convergence of the estimation errors, which could lead to difficulty in ensuring global control stability.

### 4.1.2 The proposed control idea

Based on the above analysis, this chapter firstly proposes an adaptive finite time force control based TDE for an intelligent deburring system driven by the APAM regardless of a dynamic model, and external disturbance. The proposed control is developed from the FITSMC framework with TDE and adaptive switching terms. One more of the objectives is to propose a novel observer namely a friction-free disturbance combined state observer (FSOB) which can obtain the force and state information of the system using only position sensors in the presence of static friction and noise. To fulfill this goal, this chapter designs a new force combined state observer based on a wideband observer and Levant's differentiator (LeD), which can eliminate the dither component and noise effect in a finite time, so that the closed-loop control system can be realized with full state available. Finally, the method is applied to antagonistically driven PAM joints in a series of experimental trials. To the best of the authors' knowledge, the investigation of unified torque/force impedance control and safe contact-loss handling in the domain of PAM actuators has nonexistent yet in the past. The main contributions of this chapter are summarized as follows:

- A friction-free disturbance observer combined with a state estimation scheme is proposed in this work to obtain not only the force information but also the joint angular velocities of the systems. The effect of noise and static friction can also be eliminated using the proposed observer.
- The control performances of the closed-loop system, such as fast response, high accuracy, and robustness with the modeling error and unknown environment are improved. The FITSMC guarantees the finite convergence of the sliding variable and control error. The TDE technique is employed to solve the modeling error and unknown environment. However, the TDE is limited by approximating the lumped uncertainties. In order to overcome this challenge, an adaptive switching term is deployed to adjust the switching gain in the FITSMC online. Moreover, the stability of the closed-loop control is theoretically demonstrated by the Lyapunov approach.

- In order to verify the reliability and superiority of the proposed control, some experiments are conducted on different working conditions.

## 4.2 Controller descriptions

### 4.2.1 Proposed Friction Free Force combined State Observer

In this section, as shown in Figure 18, the proposed control algorithm for the manipulated joint-based APAM to achieve the above objectives is considered to be an environmental touch. Using the DO the presence of high static friction torque degrades the efficiency of force control. Friction cancelation can improve the performance of force estimation. In [61], the dithering technique is used to compensate for friction, in which a periodic signal is applied to the control torque signal with an appropriate frequency and amplitude to produce vibrations on the actuator and to eliminate the effect of static friction. Nevertheless, this approach has the downside of adding periodic interruption to the force observer. In this work, the FSOB is designed to not only estimate the force signal and decrease the friction and oscillatory activity in the force signal but also to estimate the joint angular velocity with a dither signal. Information on the frequency of the additional signal to suppress the periodic element in the force signal is acquired by the FSOB design. The periodic torque $\tau_e$* is given as the following.

$$\tau_e^* = \frac{\omega_e^2}{s^2 + 2\xi_e\omega_e s + \omega_e^2}\tau_e \tag{40}$$

where $\omega_e$ is the predetermined angular frequency of the additional periodic signal and $\xi_e$ indicates the damping ratio. Thus, the state-space model of the DO is given as follows

$$\begin{cases} \dfrac{d}{dt}\theta = \dot{\theta} \\ \dfrac{d}{dt}\dot{\theta} = M_n^{-1}\left(\tau - \tau_e^* - C_n\dot{\theta} - K_n\theta\right) \\ \dfrac{d}{dt}\ddot{\tau}_e^* = -2\xi_a\omega_a\ddot{\tau}_e^* - \omega_a^2\dot{\tau}_e^*; \dfrac{d}{dt}\dot{\tau}_e^* = \ddot{\tau}_e^*; \dfrac{d}{dt}\tau_e^* = \dot{\tau}_e^* \end{cases} \tag{41}$$

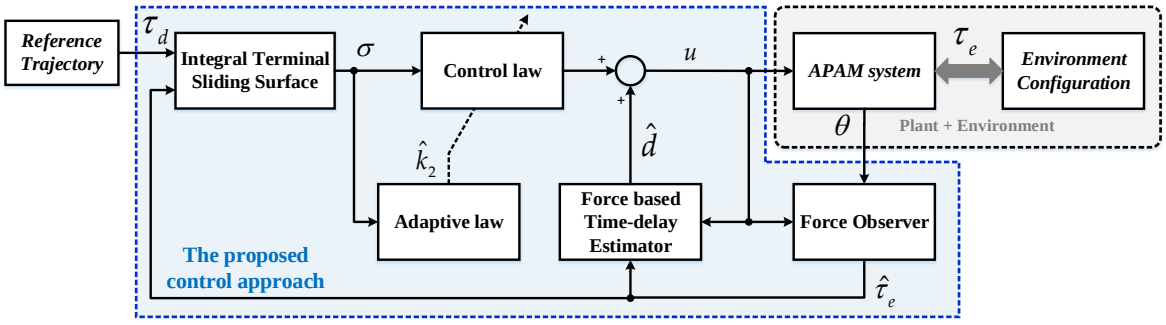


*Figure 18. Structure of the proposed control.*

Let the state variable define as $\eta = \left[\theta, \dot{\theta}, \ddot{\tau}_e^*, \dot{\tau}_e^*, \tau_e^*\right]^T$ , then the model of the DO can be rewritten as the following

$$\begin{cases} \dot{z} = A_\Delta z + B_\Delta \tau \\ y = C_\Delta z \end{cases} \tag{42}$$

where

$$A_\Delta = \begin{bmatrix} 0 & 1 & 0 & 0 & 0 \\ -M_n^{-1}K_n & -I_n^{-1}C_n & 0 & 0 & -M_n^{-1} \\ 0 & 0 & -2\xi_e\omega_e & -\omega_e^2 & 0 \\ 0 & 0 & 1 & 0 & 0 \\ 0 & 0 & 0 & 1 & 0 \end{bmatrix};$$

$$B_\Delta = \begin{bmatrix} 0 & M_n^{-1} & 0 & 0 & 0 \end{bmatrix}^T; C_\Delta = \begin{bmatrix} 1 & 0 & 0 & 0 & 0 \end{bmatrix}$$

Since only the information of $\theta$ is obtained using the position sensor, then using a minimum-order observer method and the Ackermann technique, the FSOB is designed as follows:

$$\begin{aligned} \dot{x} &= A_k x + B_k \tau_e + D_k \theta \\ y &= x + \Gamma\theta \end{aligned} \tag{43}$$

where $x = \begin{bmatrix} \zeta_1 & \zeta_2 & \zeta_3 & \zeta_4 \end{bmatrix}^T; \dot{x} = \begin{bmatrix} \dot{\zeta}_1 & \dot{\zeta}_2 & \dot{\zeta}_3 & \dot{\zeta}_4 \end{bmatrix}^T$ $y = \begin{bmatrix} \dot{\theta} & \hat{\ddot{\tau}}_e^* & \hat{\dot{\tau}}_e^* & \hat{\tau}_e^* \end{bmatrix}^T$, $\hat{\ddot{\tau}}_e^*$, $\hat{\dot{\tau}}_e^*$, and $\hat{\tau}_e^*$ are the estimated value of $\ddot{\tau}_d^*$, $\dot{\tau}_d^*$, and $\tau_d^*$, respectively; $\Gamma = [k_1, k_2, k_3, k_4]^T$ is the state observer gain matrix which is designed by the pole-placement method [62]. The matrices $A_k$, $B_k$, and $D_k$ are given as the following.

$$A_k = \begin{bmatrix} -M_n^{-1}C_n - k_1 & 0 & 0 & -M_n^{-1} \\ -k_2 & -2\xi_e\omega_e & -\omega_e^2 & 0 \\ -k_3 & 1 & 0 & 0 \\ -k_4 & 0 & 1 & 0 \end{bmatrix}; B_k = \begin{bmatrix} M_n^{-1} \\ 0 \\ 0 \\ 0 \end{bmatrix}; D_k = \begin{bmatrix} -M_n^{-1}C_n k_1 - k_1^2 - M_n^{-1}K_n \\ -k_1k_2 - 2\xi_e\omega_e k_2 - \omega_e^2 k_3 \\ -k_1k_3 + k_2 \\ -k_1k_4 + k_3 \end{bmatrix} \tag{44}$$

$$\hat{\tau}_e = \frac{\hat{\ddot{\tau}}_e^* + 2\xi_e\omega_e\hat{\dot{\tau}}_e^* + \omega_e^2\hat{\tau}_e^*}{\omega_e^2} \tag{45}$$

From (40), the estimation torque without periodic component is given as the following. According to (41) - (45), the FSOB can eliminate the periodical disturbance in the force information. To deal with the noise problem in the estimation of $\ddot{\tau}_e^*$, $\dot{\tau}_e^*, \tau_e^*$, the LeD is employed as the following [40, 63, 64].

$$\begin{cases} \dot{\delta}_1 = \psi_1,\ \dot{\delta}_2 = \psi_2,\ \dot{\delta}_3 = \psi_3,\ \dot{\delta}_4 = \psi_4 \\ \psi_1 = -\alpha_1 \left|\delta_1 - \tau_e^*\right|^{3/4} sign\left(\delta_1 - \tau_e^*\right) + \delta_2 \\ \psi_2 = -\alpha_2 \left|\delta_2 - \psi_1\right|^{2/3} sign\left(\delta_2 - \psi_1\right) + \delta_3 \\ \psi_3 = -\alpha_3 \left|\delta_3 - \psi_2\right|^{1/2} sign\left(\delta_3 - \psi_2\right) + \delta_4 \\ \psi_3 = -\alpha_4 sign\left(\delta_4 - \psi_3\right) \end{cases} \tag{46}$$
$$\hat{\tau}_e^* = \delta_2,\ \hat{\dot{\tau}}_e^* = \delta_3$$

where $\psi_1$, $\psi_2$, $\psi_3$ and $\psi_4$ are the extended state variable, $\alpha_1$, $\alpha_2$, $\alpha_3$, $\alpha_4$ are designed positive parameters. By selecting the appropriate values of $\alpha_1$, $\alpha_2$, $\alpha_3$, and $\alpha_4$, the estimation values in (46) can reach the real values in finite time [63, 65] with small estimation errors.

**Remark 4.1**: *It is noted that the LeD can achieve finite-time convergence of the estimation errors no matter what the controller input. Therefore, the proposed control scheme and the state observer can be designed separately. Thus, the FSOB for the PAM system can be implemented with the full state available.*

### 4.2.2 The proposed nonlinear control design

The control objective is to generate the control input for the system of how its generating force, $\tau$ to achieve the external force $\tau_e$. Then the system model (18) can be rewritten as follows [44, 66]:

$$\tau = K_c u(t) \tag{47}$$

where $K_c$ is a control coefficient; $u(t)$ is the control input signal.

The system model (18) is represented by replacing (47) and (46) as follows:

$$M\ddot{\theta} + C\dot{\theta} + K\theta = K_c u(t) - \hat{\tau}_e \tag{48}$$

where $\hat{\tau}_e$ is the estimated force of the external force $\tau_e$. Defining a force tracking error between the estimated output force and the desired force as follows:

$$e_f = \tau_d - \hat{\tau}_e \tag{49}$$

Before the proposed force control for the APAM system is derived, the system dynamics (48) is rewritten as follows:

$$u(t) = K_c^{-1}\left[M\ddot{\theta} + C\dot{\theta} + K\theta + \hat{\tau}_e\right] \tag{50}$$

An integral terminal sliding mode surface (ITSMS) is defined as follows:

$$\sigma = e_f + \lambda_1 \int_0^t \left(e_f(\chi) + \lambda_2 sign(e_f(\chi))^{[v]}\right) d\chi \tag{51}$$

where $\lambda_i$, ($i$ =1, 2 > 0) are positive coefficients of the sliding surface; $v = p/q$; $q > p > 0$ are odd positive constants.

Its derivative with respect to time is presented as

$$\dot{\sigma} = \dot{e}_f + \lambda_1 e_f + \lambda_1 \lambda_2 sign(e_f)^{[v]} \tag{52}$$

Defining a lumped dynamics term, $d(t)$, as follows

$$d(t) \triangleq K_c^{-1}\left[M\ddot{\theta} + C\dot{\theta} + K\theta\right] + \left[K_c^{-1} - \hat{K}_c^{-1}\right]\hat{\tau}_e \tag{53}$$

**Assumption 4.1:** *In practice, the displacement and velocity of the APAM system are bounded. Then, the uncertain d is also bounded by* $\|d(t)\|_\infty \le d_\Delta$ *where* $d_\Delta$ *is a positive constant.*

**Assumption 4.2:** *The TDE error can be expressed by the following formula,* $\varepsilon \le \kappa_5^* sign(\sigma)^{[v]}$

Then, the APAM system dynamics is represented as follows:

$$u(t) = d(t) + \hat{K}_c^{-1}\hat{\tau}_e \tag{54}$$

From (51) and (54), the control law for the FITSMC can be presented as follows:

$$u(t) = \hat{d}(t) + \hat{K}_c^{-1}\left[\tau_d + \lambda_1^{-1} e_f + \lambda_2 sign(e_f)^{[v]} + \kappa_4 \sigma + \kappa_5 sign(\sigma)^{[v]}\right] \tag{55}$$

where $\kappa_4$, $\kappa_5$ are positive constants; $\hat{d}(t)$ is the estimation of $d(t)$.

The estimated lumped disturbance $\hat{d}(t)$ is the estimation of the nonlinear term $d(t)$ and can be calculated as

$$\hat{d}(t) \cong d(t - t_d) = u(t - t_d) - \hat{K}_c^{-1}\hat{\tau}_e(t - t_d) \tag{56}$$

where the time variable $t$ is ignored for simplicity, except for the time-delay value $t - t_d$.

The proposed control law based on the FITSMC with TDE is represented as follows:

$$u(t) = u(t - t_d) - \hat{K}_c^{-1}\hat{\tau}_e(t - T_d) + \hat{K}_c^{-1}\left[\tau_d + \lambda_1^{-1}\dot{e}_f + \lambda_2 sign(e_f)^{[v]} + \kappa_4 \sigma + \kappa_5 sign(\sigma)^{[v]}\right] \tag{57}$$

From (51), (53) and (59), the closed-loop dynamics can be expressed as

$$\begin{aligned} \dot{\sigma} &= \dot{e}_f + \lambda_1 e_f + \lambda_1 \lambda_2 sign(e_f)^{[v]} \\ &= \lambda_1\left[\hat{K}_c^{-1}(d - \hat{d}) - \kappa_4 \sigma - \kappa_5 sign(\sigma)^{[v]}\right] \end{aligned} \tag{58}$$

The bounded TDE error is defined as

$$\varepsilon = d - \hat{d} \tag{59}$$

The term $\kappa_4 \sigma + \kappa_5 sign(\sigma)^{[v]}$ on the right-hand side in (58) not only compensates for the TDE error but also provides fast convergence to the sliding surface.

In practice, when some disturbances suddenly arise in the system, the TDE is difficult to estimate completely. So, the TDE error which is significantly degraded the control performance. An adaptive switching gain law is investigated as

$$\dot{\hat{\kappa}}_5 = \frac{\eta_5}{\eta_4^{sign(|\sigma|-\varepsilon_\sigma)}} |\sigma|^{[v+1]} sign\left(|\sigma| - \varepsilon_\sigma\right) \tag{60}$$

are positive learning rates

$$u(t) = u(t-t_d) - \hat{K}_c^{-1}\hat{\tau}_e(t-T_d) + \hat{K}_c^{-1}\left[\tau_d + \lambda_1^{-1}\dot{e}_f + \lambda_2 sign(e_f)^{[v]} + \kappa_4\sigma + \hat{\kappa}_5 sign(\sigma)^{[v]}\right] \tag{61}$$

**Remark 4.2**: *When the external disturbance suddenly arises in the system, the sliding variable will leave the sliding surface and the force error will be significant. Based on the adaptive switching gain law* (60)*, the switching gain will increase significantly to suppress the abrupt disturbance and to force the sliding variable to reach the sliding surface. When the sliding variable closes to the sliding surface,* $|\sigma| \le \varepsilon_\sigma$*, the switching gain will decrease quickly to reduce the heavy computations in the control law* (60).

**Lemma 4.1:** *According to* [67] *consider a nonlinear system* $\chi = f(\chi)$*. Assume that there exists a smooth positive definite Lyapunov function* $V(\chi)$ *and some constants* $\alpha, \beta > 0$*, and* $1 > \gamma > 0$ *such that*

$$\dot{V}(\chi) + \alpha V(\chi) + \beta V^{\gamma}(\chi) < 0, t \ge 0 \tag{62}$$

*then the nonlinear system* $\dot{\chi} = f(\chi)$ *is global finite-time stable. The variable* $\chi$*, reaches zero from any given initial condition* $\chi(0) = \chi_0$ *in finite-time stability* $t_f$*, which can be calculated as follows:*

$$t_f = \frac{1}{\alpha(1-\gamma)} \ln \frac{\alpha V^{1-\gamma}(\chi_0) + \beta}{\beta} \tag{63}$$

**Lemma 4.2:** *Let* $x, y \in R$*, if* $x > 0$ *and* $0 < y < 0$*, the inequality condition* $(x^2)^y \le (x^y)^2$ *hold.*

**Lemma 4.3**: *When the control input* (57) *is developed on the APAM system* (48)*, the TDE error* (59)*, ultimately bounded if the TDE gain,* $\hat{K}_c$*, is selected to satisfy* [68] *the condition* $\left|1 - K_c^{-1}K_c\right| < 1$.

**Theorem 4.1**: *For the APAM system* (48)*, the closed-loop sliding surface is globally uniformly ultimate bounded if the integral terminal sliding mode control is selected as* (61) *and Lemma 4.1 is satisfied.*

**Proof:** *See in Appendix* 4.1.

**Theorem 4.2**: *For the FITSMC* (51) *and* (59)*, the sliding variable converges to* $|\sigma| \leq \delta$ *in the finite time of* (190).

**Proof:** *See in Appendix* 4.2.

**Theorem 4.3:** *The closed-loop APAM system* (48) *is globally uniformly ultimate bounded* (*GUUB*) *if the integral terminal sliding mode control is chosen as* (51), (60) *and* (61), *and* Lemma 4.1 *holds.*

**Proof:** *See in Appendix* 4.3.

### 4.3 Experimental results and discussion

In the experiments, the performance of the proposed force control is investigated to show the superiorities such as model-free controller, fast convergence, enhancing accuracy, and overcoming the drawback of TDE. Three references, pulse wave, multistep wave and sine wave, are utilized in the experiments. The pulse signal is set with an amplitude of 30 N, a period of 8 seconds, a pulse width of 50% and a bias of 70 N. The multistep is set with amplitudes of 70 N, 80 N, 100 N, 130 N, and 110 N from 0 to 20 seconds, and with an interval time of 4 seconds. Finally, the sin wave is set with the amplitude of 30 N, the bias of 95 N, frequency 0.1 Hz, and phase of $-2/\pi$. In order to verify the effectiveness of the proposed control, other controllers such as PID control, ISMC, FTISMC and FTISMC with TDE are conducted for comparison. As abovementioned, all controllers are developed on MATLAB simulation with a sampling time of 0.001 second. The parameters of these controllers are carefully selected on how to guarantee fairness in comparisons. The control parameters are tuning by the trial-error method as $K_p = 1$, $K_i = 5$, $K_d = 0.01$, $\lambda_1 = 5$, $\lambda_2 = 0.1$, $\kappa_4 = \kappa_5 = 1$, $K_c = 0.02$, $\nu = 9/11$, $t_d = 0.0005$, $\eta_4 = 0.5$, $\eta_5 = 25$.

**Remark 4.3**: *In the above controllers, the PID control, FITSMC with TDE, and the proposed control are designed without a system model while the ISMC and FITSMC require the system model. The ISMC and FITSMC are designed based on the nominal parameters of the system, which are determined by the identification method. When comparing the FITSMC with ISMC, the results are expected the finite convergent property of the FITSMC. Because the FITSMC with TDE is developed from the FITSMC and the proposed control is inherited from the FITSMC with TDE, the control parameters of these controllers will concern with together*.

**Remark 4.4**: *The pulse and multistep references are investigated to testify the fast convergence and enhancing the accuracy abilities of the proposed control with the different setpoint reference input.*

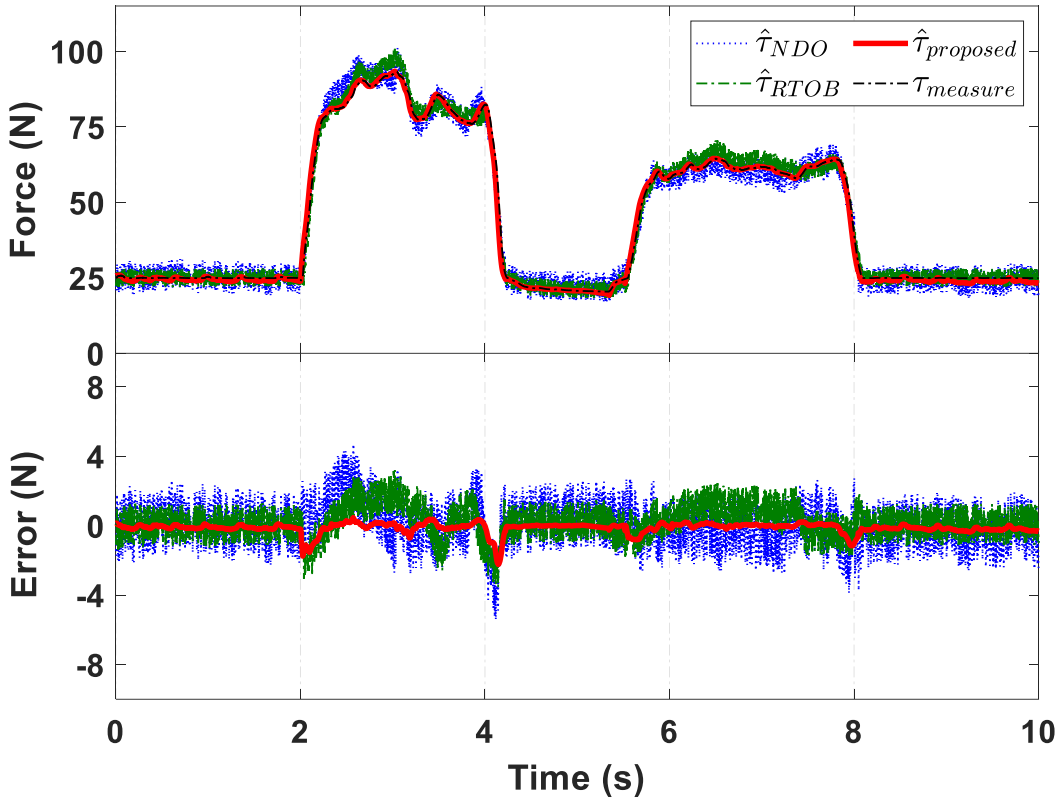


*Figure 19. Environment force estimation performances of three comparative observers.*

### 4.3.1 Estimation Force Validation

Three force observers are implemented to obtain the external force from the, which are the NDO used in [56], the reaction torque observer (RTOB) with Kalman filter used in [59], and the proposed FSOB. In the NDO design, the force observer gain for the system are chosen as $L_h = L_e = 10$. In the RTOB design, the cut-off frequency of the force observer is designed as $\beta = 1500$ rad/s. Meanwhile, the parameters of the proposed FSOB are designed as follows. The observer pole of the FSOB is chosen as 500 rad/s while the dither signal with an amplitude of 1 N, frequency of 5 Hz and damping ratio of 0.001 is added to the control signal. The parameters of LeD is chosen as $\alpha_1 = 20$, $\alpha_2 = 12$, $\alpha_3 = 5$, $\alpha_4 = 1.5$.

The estimation performances of the three comparative observers for environment torque is depicted in Figure 19. As shown in this figure, all three observers can fairly obtain the force information with acceptable estimation errors. However, these results show that the steady-state errors of NDO and RTOB are largely due to the effect of static friction in the bilateral operation system. Meanwhile, the performance of the proposed FSOB is much improved with small steady-state estimation errors and effective noise suppression. Therefore, this force estimation information can be employed in the force feedback control scheme.

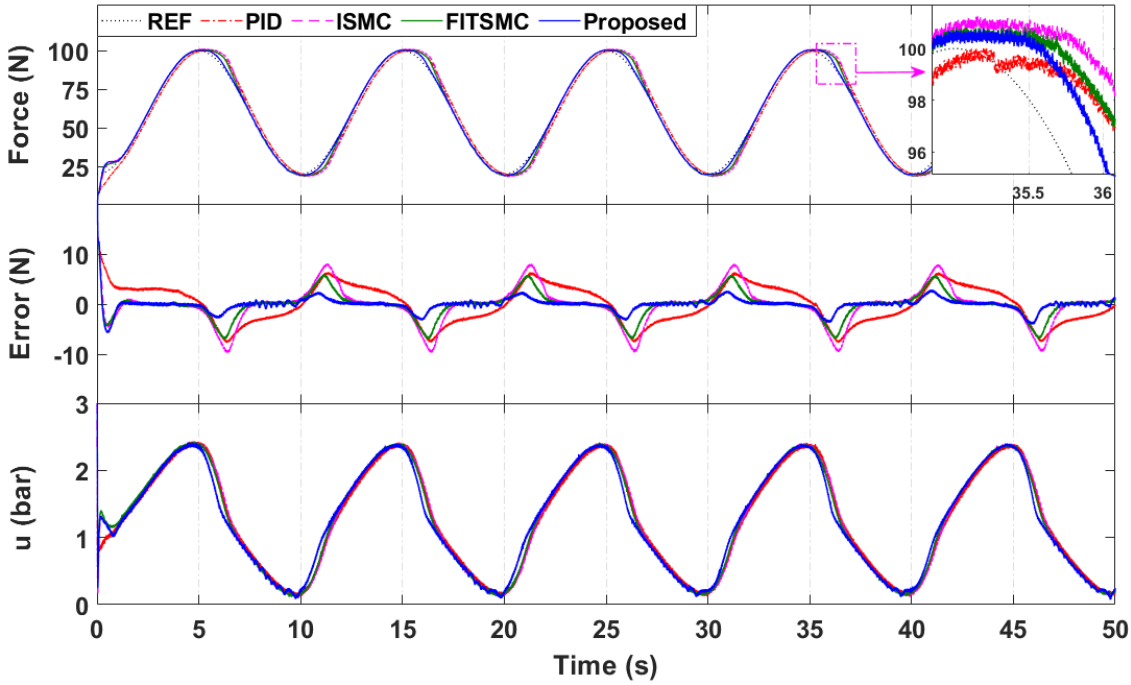


*Figure 20. Comparison of control performance with respect to scenario 1.*

**Remark 4.5**: *It is noted that the LeD can achieve finite-time convergence of the estimation errors no matter what the controller input. Therefore, the proposed control scheme and the state observer can be designed separately. Thus, the FSOB for the bilateral teleoperation system can be implemented with the full state available.*

### 4.3.2 Scenario 1

In this scenario, the sin reference set with the amplitude of 75 N, a bias of 25 N, frequency 0.1 Hz, and phase of $-\pi/2$ is applied in the testbench. The performance of the proposed force control is investigated without external disturbance. All experiments are implemented when the end-effector is kept in a static state. Three types of references are applied to verify the effectiveness of the proposed control. Figure 20 presents, in turn, the force performances, the errors and the control signals of the PID, ISMC, FITSMC, FITSMC with TDE, and the proposed control. From these results, it is easy to see that the controllers developed by the FITSMC framework make faster responses than the PID and ISMC. Because the proposed control is an integrated more advanced method than ITSMC and FITSMC, it gives the best time convergence in all controllers. It can seem that some vibrations exist in the proposed control.

### 4.3.3 Scenario 2

In order to further investigate the advantage of the designed control structure, a desired frequency sinusoidal signal is increased from 0.1 Hz to 0.4 Hz and the force range from 25 N

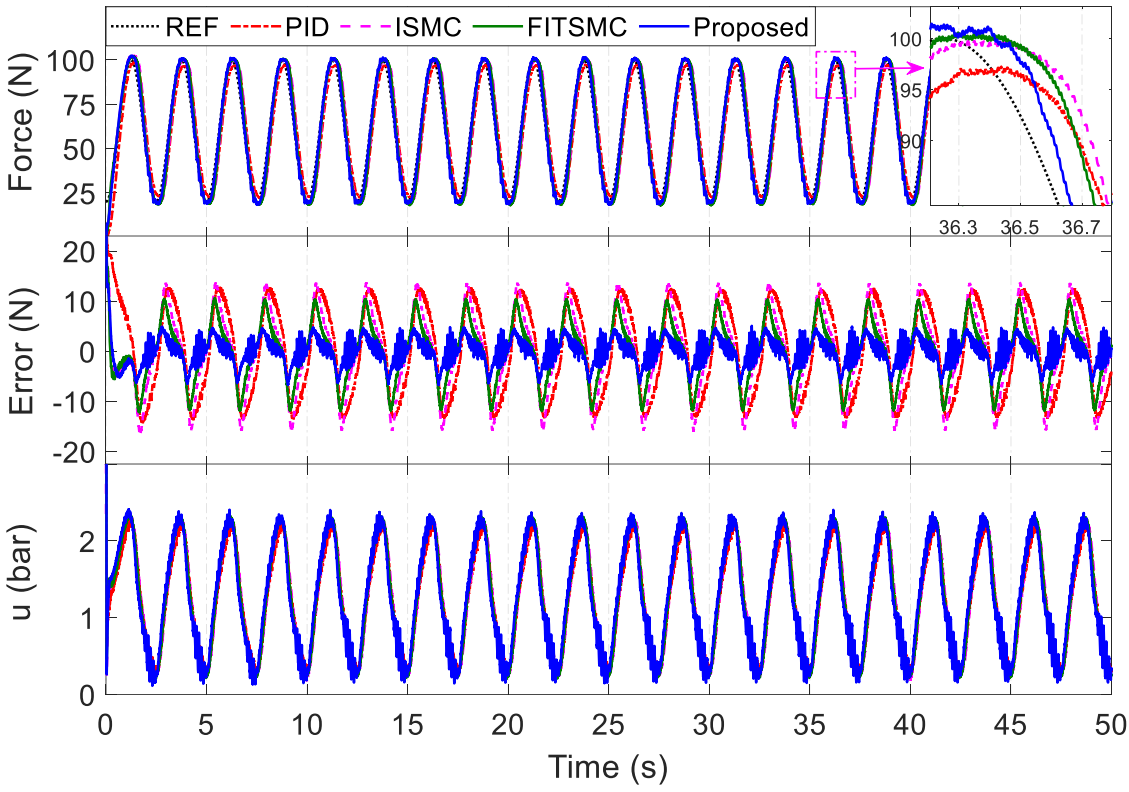


*Figure 21. Comparison of control performance with respect to scenario 2*

to 100 N is selected as a reference trajectory. Also applying the PID, ISMC, FITSMC, FITSMC with TDE, and the proposed control algorithm, the tracking performances, tracking errors, and control signals of the corresponding controllers are depicted in Figure 21. As shown in this figure, it is clear that the PID performance was significantly degraded with the bound of the tracking error with respect to 0.4 Hz sinusoidal reference nearly two times that of scenario 1, from 7.5% at 0.1 Hz to 14% at 0.4 Hz. Meanwhile, the FITSMC shows its better robustness performance with the bound of tracking errors increased from 7.8% at 0.1 Hz to 10.5% at 0.4 Hz. In contrast, the proposed controller still maintained its merit with the tracking errors is kept in a small range, 3.1% at 0.1 Hz and 7.1% at 0.4 Hz. With regard to the chattering phenomenons, it is shown that the chattering phenomenon was significantly attenuated in the proposed control signal compared to the FITSMC signal, whereas the excellent tracking performance was still ensured. This once again validates the advantage of the proposed control method.

**Remark 4.6**: *The vibration reduction in the control responses are not considered in this research. This issue will be investigated in future work.*

#### 4.3.4 Scenario 3

Next, Figure 22 provides the force responses of the controllers with a multistep reference which are smoothed by a low pass filter with a bandwidth of 0.2 (rad/s). The force errors also prove the superiorities of the proposed control in fast convergence. The control signal of the proposed control still occurs with some vibrations. As a result, their force errors presented to point out the drawback of the TDE in uncertain compensator, which cannot well approximate

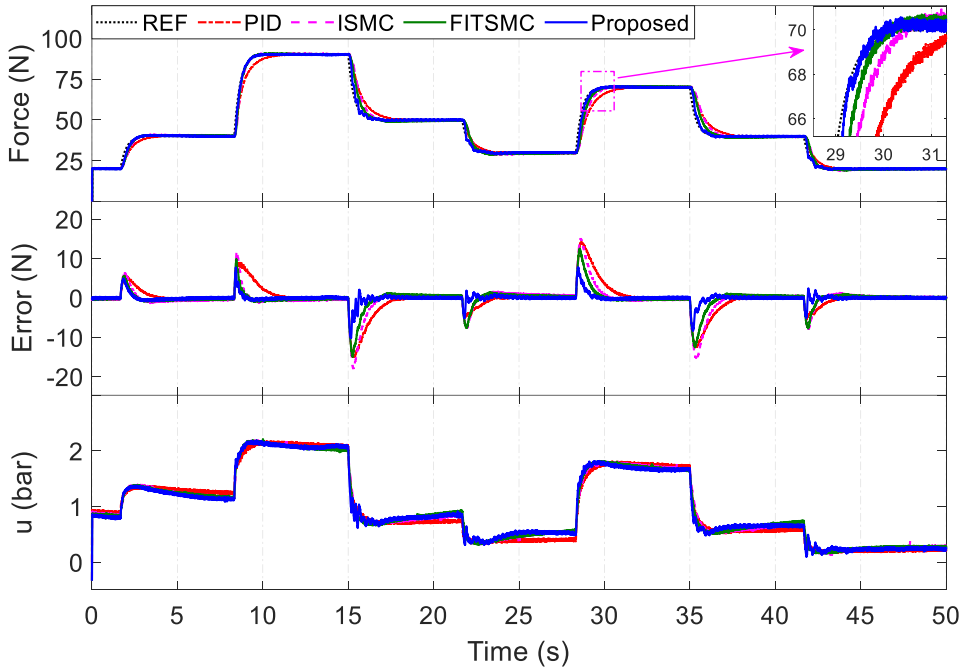


*Figure 22. Comparison of control performance with respect to scenario 3.*

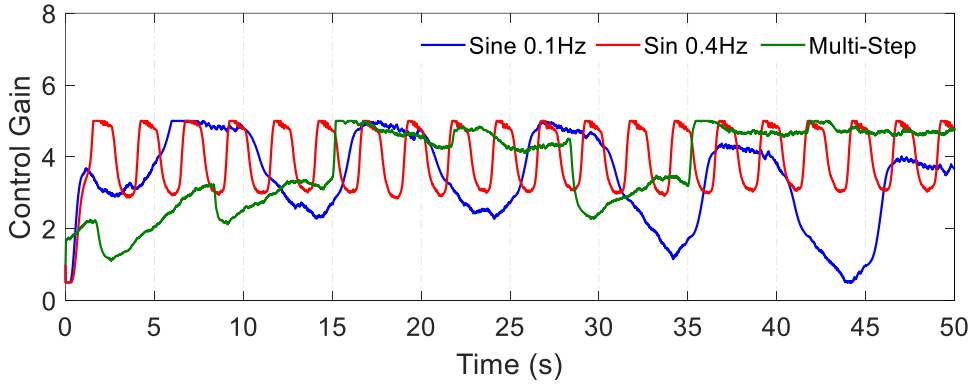


*Figure 23. Control gain in scenarios.*

the Coulomb friction model. In order to overcome the limitation of the TDE, an adaptive law is produced to adjust the switching gain of the FITSMC. The effectiveness of the adaptive law is clearly presented with the force error of the proposed control. Similar to the above experimental cases, the control signal of the proposed control still has some vibration. The adaptive gain responses of the proposed control in three study cases are presented in Figure 23, which

fluctuate up and down as explained in control design. In order to further prove the effectiveness of the proposed method, the RMSE method, a statistical method, is conducted on force errors. The results provided that the controllers developed from FITSMC with TDE improved the accuracy better than others. The RMSs of the FITSMC with TDE and the proposed control in sin reference are 0.9440 and 0.5158 at 0.1 Hz, and 2.0632 and 1.19807 at 0.4 Hz , and 2.0618 and 1.7685 in multistep reference. As a result, the effectiveness of the FITSMC with TDE and the proposed controller are similar in pulse and multistep reference. The superiority of the proposed control is highlighted in the sin reference.

## 4.4 Chapter summary

This chapter presented an adaptive finite time force control for the APAM system. The proposed control was developed based on FITSMC and force-based TDE framework. The Force based TDE provided a simple structure to estimate the lumped uncertainties in the system. The FITSMC used the estimated lumped uncertainties from TDE to guarantee the fast response and high accuracy of performance. Furthermore, an adaptive switching gain law is also employed to deal with the reconstructed error of the FBTDE. Stability and robustness of the force control were theoretically demonstrated by the Lyapunov approach. Finally, some experimental scenarios were conducted on a test bench. The experimental results were compared to other controllers to verify the reliability and superiority of the proposed method. The force tracking performance was mentioned in this study. Next work, this device will be integrated on a robotic manipulator with position control to verify the effectiveness of the proposed control in the automated finishing process.

# Chapter 5

# MODEL-FREE CONTROL FOR OPTIMAL CONTACT FORCE OF A APAM SYSTEM IN UNKNOWN ENVIRONMENTS USING RL

## 5.1 Introduction

### 5.1.1 Overview

With the lightning speed of technological evolution, robot-environment interaction has rapid and widespread development in recent years [69]. Therefore, the movement and interaction of robots in dynamically changing and harsh environments is hardly feasible when applying the precise kinetic planning of the foothold. The collision of the robot with an environment can be viewed as a mechanical admittance and impedance. Based on its design, the robot may have admittance or impedance type interfaces [70, 71]. In order to achieve effective force, the parameter values of the impedance model have to similar to the environmental parameters [72]. In other instances, the efficiency of impedance control is independent of operator parameters which are usually chosen beforehand [73]. The robot-environment interaction control can be temporarily divided into two types as position control and force control [71, 74-76]. These factors motivate the improvement of impedance control. According to [77] a linear quadratic regulator (LQR) controller based on an impedance model [78] is employed for the robot-environment interaction to provide the ideally optimal desired force e.i. it means that minimizes the position error. The LQR, however, requires the environmental dynamics information. Thus, the great interactive efficiency of the robot is not ensured due to the modeling error [79] under an unknown environment. In reality, the force and torque control was critical because the majority of the robot arms or legs were controlled by stiff joints. So the real-time information about the contact dynamics and forces should be considered. In addition, the kinematic domain had to be carefully intended to interact with the environment. Although today's industrial robots could easily be taken into sufficient for most tasks, autonomous robots will be faced with difficulties to obtain either a perfect status estimation or a perfect map of the environment for themselves [70, 80], so on. Some robot and environmental dynamics prediction approaches are also available, for instance, adaptive recognition, neural networks [81], adaptive impedance control [82]. Additionally, the recursive least squares (RLS) technique can be used to perform

the optimal interactive force. However, this solution requires three separate steps performance consisting of, the first one, the environment is defined. Then the second step, the environmental parameters are estimated to solve the LQR control problem. And the final step, the position and force controllers are applied to achieve the control purposes. By using the recursive solution of the Lyapunov equation[17] in two stages, the task space can also be handle with a minimum process (combining steps two and three). The RL [18] techniques are commonly used in task space control. namely adaptive dynamic programming (ADP) is also referred to where data computed along system trajectories, which is analyzed [83]. In [84], the most popular approaches are introduced as Temporal Difference methods, which describes a model-free strategy of an optimal iterative solution. Besides, for time-varying environments, the RL methods [79, 83] can be used to calculate the significantly optimal impedance model in an impedance/admittance control. In [86, 87], the critical algorithm is used to obtain an optimal impedance model. Moreover, the energy storage tank method [88, 89] or linear parametrization method [90] is often used to calculate environmental parameters. Therefore, those techniques are complicated and only ensure tracking of position while the interactive force is free in the meantime.

### 5.1.2 The proposed control idea

In this chapter, an ideal interactive force of the slave subsystem in an unknown environment is presented. To learn the ideal desired force on-line, the RL technique is used to minimize the interactive force. The integral RL technique is then employed in order to perform both position and force tracking simultaneously. The force controller helps to produce the new desired position that feeds the FNTSMC-based position controller. To compare the method with the LQR solution, real-time experiments are applied. The results obtained demonstrate that the approach is efficient in unknown environments for robot interaction control.

## 5.2 Control Strategy

### 5.2.1 Robot Position/Force control

Hence, the system model (18) is represented as follows:

$$M\ddot{\theta} + C\dot{\theta} + K\theta = \tau - r_0 F_e \tag{64}$$

where $M$, $C$, $K$, denote the varying load, damping coefficient and the stiffness coefficient, respectively; $F_e$ is the robot-environment interaction force and $\tau$ the generated torque coordinates and $r_0$ is the distance of the interactive force and the center APAM joint. Let calculating as

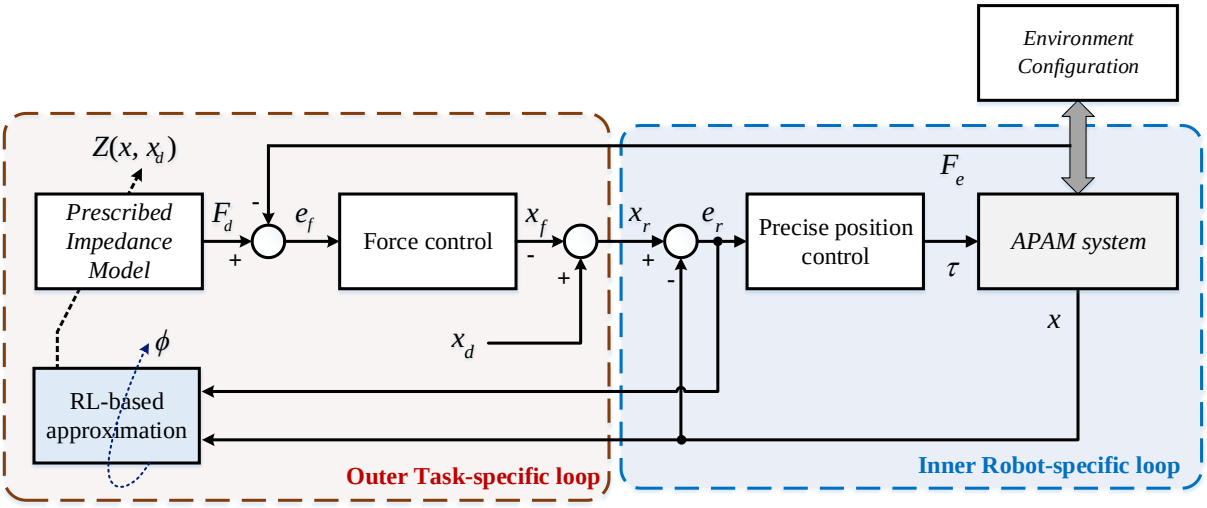


*Figure 24. Structure of the proposed optimal contact force control.*

$$x = r_0 \sin\theta \tag{65}$$

where $x \in \mathbb{R}^m$ is the position of the robot end-effector in task space.

Figure 24 displays the robot-environment interface scheme in which the environment model is modeled [81]:

$$F_e = -C_e\dot{x} + K_e(x_e - x) \tag{66}$$

where $C_e$, $K_e$ and $x_e$ are the damping, stiffness of the environment, the environment position is located, respectively. When the slave-environment interaction occurs, i.e., $x \geq x_e$, (66) can be become:

$$\dot{x} = Ax + BF_e \tag{67}$$

where $A = -C_e^{-1}K_e$ and $B = -C_e^{-1}$. According to [92] and [93], the typical target impedance model describes the force-position relation by the error function of the desired and a virtual reference position

$$Z(e_r) = Z(x_r, x_d) = F_d \tag{68}$$

$$e_r = x_r - x;\ x_r = x_d - x_f \tag{69}$$

where $x_r$, $x_d$ and $x_f$ represent the virtual reference trajectory and desired reference, the virtual reference trajectory, which is the position control input, respectively; $F_d$ is the desired force; according to (67), $Z(\bullet)$ is the impedance model. However, the objective is to determine the impedance model $Z^*(e_r)$ e.i. to optimize the desired force $F_d^*$ as well as the minimum position error $e_r(t)$. It is worth noting that this approach does not use environmental information. The impedance model for the environment model (67) is designed as

$$\dot{e}_r(t) = Ae_r(t) + BF_d(t) \tag{70}$$

Especially, the desired force $F_d(t)$ in (70) is the control input. To achieve good tracking performance and fast response of systems, a fast finite time nonsingular terminal sliding mode control is employed for the system in the task space. The position control signal in task space is introduced as follows:

$$\tau = \bar{M}\ddot{e}_r(t) + \bar{C}\dot{e}_r(t) + \bar{K}e_r(t) - \eta_\Delta sign(\sigma) - \rho_1\sigma - \rho_2\sigma^{[v]} + F_e(t) \tag{71}$$

where $\bar{M}, \bar{C}, \bar{K}$ are the nominal values of the inertia term $M$, damping term $C$, stiffness term $K$, respectively; $\eta_\Delta$ is the bound value of the unexpected disturbances; $\rho_1$, $\rho_2$ are the positive constants for the reaching phase; $0 < v < 1$; $\alpha = p/q$, $p$ and $q$ are positive odd integers satisfying $q > p$; $\sigma$ is a sliding surface, which is defined as follows:

$$\sigma = \lambda e_r^{[\alpha]}(k) + \dot{e}_r^{[\alpha]}(t) \tag{72}$$

where $\lambda$ is a positive parameter of the sliding surface. The sufficient condition for the stability of the system is discussed in [44, 91].

Awareness of the impedance parameters (68) is not needed for the purpose of this work, but instead, the force calculation of the contact force Fe is used, which provides an indirect way of knowing the dynamic properties of the environment. The PI force control is applied to change the desired location for the inner loop as follows, as the force signal is available:

$$x_f(s) = K_{Pf}e_f(t) + K_{If}\int_t^\infty e_f(\tau)d\tau \tag{73}$$

where $e_f = F_d - F_e$ is the force tracking error differencing of the desired force $F_d$ and the interactive force $F_e$; $K_{Pf}$, $K_{If}$ are the proportional and the integral gain, respectively. Stability of the force controller (73) is discussed in [94, 95].

### 5.2.2 Optimal desired force

***a) Linear Quadratic Regulator solution***

The optimal desired force is determined when the dynamics of the environment are known as the following. The purpose is to optimize the desired force $F_d^*$, e.i. the minimal the position error $e_r$:

$$F_d^*(t) = \kappa_e e_r(t) \tag{74}$$

which $\kappa_e \in \mathbb{R}^{m\times m}$ is gain of the feedback control, which can minimize by the cost function:

$$J_s = \int_t^\infty \left(e_r^T(\tau)Re_r(\tau) + F_d^T(\tau)GF_d(\tau)\right)\gamma(\tau - t)d\tau \tag{75}$$

where $R = R^T \geq 0$ is the weight of the tracking error and $G = G^T > 0$ is the weight of the interaction force, respectively, $0 < \gamma \leq 1$ is an element factor and $F_d$ is a feedback control policy in (70). The gain vector $\kappa_e$ can be calculated by the ARE [83] and $P$ is the solution.

$$A^T PA + S + P + A^T PB\kappa_e = 0 \tag{76}$$

Then the feedback control gain $\kappa_e$ can be calculated as:

$$\kappa_e = -\left(B^T PA\right)^{-1} B^T PB + \gamma^{-1} G \tag{77}$$

Since the environment model is a first-order design, only the virtual stiffness gain [76] is required for the controller $\kappa_e$ but this gain is an offline LQR solution. Thus it needs an online solution.

***b) Reinforcement Learning solution***

The model of impedance includes knowledge of the dynamics of the system to calculate the ARE solution. Nevertheless, without any previous environment dynamics information, it is possible to find an optimal or near-optimal solution to this problem via the RL theory. The cost function is established:

$$V_s = \int_t^\infty \left(e_r^T(\tau) R e_r(\tau) + F_d^T(\tau) G F_d(\tau)\right) e^{-\gamma(\tau - t)} d\tau \tag{78}$$

Based on the cost function (78), and a Leibniz's rule, with respect to the time derivative:

$$\dot{V}_s = \int_t^\infty \frac{\partial}{\partial t}\left(r(\tau) e^{-\gamma(\tau - t)}\right) d\tau - e_r^T R e_r - F_d^T G F_d \tag{79}$$

where $r(t) = e_r^T(t) R e_r(t) + F_d^T(t) G F_d(t)$ is a reward of the utility. The (78) function can be obtained as:

$$V_s^*\left(e_r(t)\right) = \min_{F_d}\left\{\int_t^\infty \left(e_r^T(\tau) S e_r(\tau) + F_d^T(\tau) R F_d(\tau)\right) e^{-\gamma(\tau - t)} d\tau\right\} \tag{80}$$

$$\min_{F_d}\left\{\dot{V}_s^*\left(e_r\right) + e_r^T R e_r + F_d^T G F_d - \int_t^\infty \frac{\partial}{\partial t}\left(r(\tau) e^{-\gamma(\tau - t)}\right) d\tau\right\} = 0 \tag{81}$$

The (78) function satisfies:

$$\begin{aligned} V_s^* &= \min_{F_d} V_s \\ &= \min_{F_d} \int_t^\infty \left(e_r^T(\tau) S e_r(\tau) + F_d^T(\tau) R F_d(\tau)\right) e^{-\gamma(\tau - t)} d\tau \\ &= e_r^T P e_r \end{aligned} \tag{82}$$

where $P$ is the solution to the new ARE for the online solution as

$$e_r^T\left(A^T P + PA + R - \gamma P\right) e_r + 2 e_r^T PBF_d + F_d^T G F_d = 0 \tag{83}$$

Thus, the optimal force is determined to minimize the function, which is rewritten as follows:

$$F_d^* = \kappa_e e_r = -G^{-1} B^T P e_r \tag{84}$$

Based on (83), (84), those condition has existed the cost function can form

$$V_s^*(e_r) = Q^*(e_r, F_d) = X^T H X \tag{85}$$

where $X = [e_r\ F_d]^T$ is state-action matrix; $Q$ is the value function and $H$ is a positive parameter matrix as formed:

$$H = \begin{bmatrix} H_{11} & H_{12} \\ H_{21} & H_{22} \end{bmatrix} \tag{86}$$

where $H_{11} = (A - \gamma I/2)^T P + P(A - \gamma I/2)$; $H_{12} = PB$; $H_{21} = B^T P$; $H_{22} = R$.

According to (82) and applying $\delta Q^*/\delta F_d = 0$, (84) becomes

$$F_d^*(t) = \kappa_e e_r(t) = -H_{22}^{-1} H_{21} e_r(t) \tag{87}$$

Thus, if the (A, B) is stable and the ($S^{1/2}$, $A$) is measurable, a special positive solution P exists for (82). To use an online tool, Lyapunov recursion technique can use the off-policy integral reinforcement learning (IRL) algorithm[83, 96] to search for the solution of the new ARE given (83) by an iterative political iteration algorithm, which includes the first iteration step is the policy evaluation and second iteration step is the policy improvement. An IRL Bellman equation is used in the first step to determine the value function related to a fixed policy; environmental dynamics are not involved in the analogous form of the Bellman equation. In the second step, using the value obtained within the policy assessment level, an enhanced policy is used.

In this section, the IRL Bellman equation proposed in[83, 96] was used; it only requires the information proven from device state measurement and an integral infinite reinforcement interval of the utility function to determine a control policy. The IRL is normally

$$V_s = \int_t^{t+\Delta t} e^{-\gamma \Delta t} V_s\left(e_r(t+\Delta t)\right) + r(\tau) e^{-\gamma(\tau - t)} d\tau \tag{88}$$

Fixed policy $F_d(t)$ satisfies with time $t \geq 0$ and $\Delta t > 0$:

$$V_s(t+\Delta t) = Q(t+\Delta t) \tag{89}$$

Combining (89) and (88) the $Q$-function update law can be introduced as

$$Q(t) = \int_t^{t+\Delta t} e^{-\gamma \Delta t} Q(t+\Delta t) + r(\tau) e^{-\gamma(\tau - t)} d\tau \tag{90}$$

However, the analytical solution of the integrator (90) is impossible at all times. The discretization approximation method is therefore needed for the temporal difference error (TD) to be minimized.

### *c) IRL Approximation solution*

A normalized RBFs is employed as the function $Q$ in this session. (90) is then measured as $\delta(t)$

$$\delta(t) = Q\left(e_r(t), F_d(t)\right) - \int_t^{\infty} r(\tau) e^{-\gamma(\tau - t)} d\tau \tag{91}$$

Let define $\zeta$ as follows:

$$\zeta(t) = \dot{\delta}(t) = e_r^T(t) R e_r(t) + F_d^T(t) G F_d(t) + \dot{Q}\left(t\right) - Q\left(t\right) \tag{92}$$

Based on [97], the backward Euler is employed to approximate as

$$\dot{Q}\left(t\right) = \frac{1}{\Delta t}\left[Q\left(t\right) - Q\left(t - \Delta t\right)\right] \tag{93}$$

According to (93) and (92), the temporal difference error $\zeta$ minimization becomes

$$\begin{aligned} \zeta(t) = \dot{\delta}(t) &= r(t) + \frac{1}{\Delta t}\left[Q\left(e_r(t), F_d(t)\right) - Q\left(e_r(t - \Delta t), F_d(t - \Delta t)\right)\right] - Q\left(e_r(t), F_d(t)\right) \\ &= r(t) + \frac{1}{\Delta t}\left(1 - \gamma \Delta t\right)\left[Q\left(e_r(t), F_d(t)\right) - Q\left(e_r(t - \Delta t), F_d(t - \Delta t)\right)\right] \\ &= r(t - \Delta t) + \frac{1}{\Delta t}\left(1 - \gamma \Delta t\right)\left[Q\left(e_r(t + \Delta t), F_d(t + \Delta t)\right) - Q\left(e_r(t), F_d(t)\right)\right] \end{aligned} \tag{94}$$

The correct output of the behavior is given. The temporal difference error $\zeta$ acts as the direction of the gradient. The Q(•) feature, however still needs to be determined. Since the system is run in a state-action continuously, it is impossible for all time. According to [98] the $Q(\bullet)$ function approximator is formed by the NRBFs, its estimation can be shown as:

$$\hat{Q} = \sum_{i=1}^{N} \psi_i\left(e_r, F_d\right) \phi_i = \Psi^T\left(e_r, F_d\right) \phi \tag{95}$$

where $\phi_i$ is the different parameters; $\Psi$ is NRBF values. The tyle of NRBFs can be defined as follows:

$$\begin{aligned} &\psi_i(e_r, F_d) = \frac{\psi_i'(e_r, F_d)}{\sum_{i=1}^{N} \psi_i'(e_r, F_d)}, \\ &\text{with } \psi_i'(e_r, F_d) = \exp\left(-0.5\left[e_r - c_i, F_d - c_i\right]^T \beta_i^{-1}\left[e_r - c_i, F_d - c_i\right]\right) \end{aligned} \tag{96}$$

where $\psi_i$ are the NRBFs; $c_i = [c_1, c_2, \ldots, c_i, \ldots, c_N]^T \in \mathbb{R}^N$ is the $i^{th}$ RBF the center, and $\beta_i \in \mathbb{R}^{N \times N}$ is the symmetrical positive matrix width. To get $c_i$ and $N$, $c_i$ are the centers of the clusters and $N$ is the number of RBFs, the input state into $N = K$ clusters is partition based on the $K$-means clustering algorithm. The method obtains $K$ and enables the use of NRBFs approximators.

By having random centers, the approximator gives various parameters $\phi$ to obtain the same parameters, it is important to set the center values. Updating the parameters $\phi$ in the gradient descent method is now used to minimize (94), $E = 0.5\psi^2$. The gradient concerning the parameter vector $\phi$ is

$$\frac{\partial E(t)}{\partial \phi(t)} = \frac{\zeta}{\Delta t}\left[\left(1-\gamma\Delta t\right)\frac{\partial \hat{Q}\left(t+\Delta t\right)}{\partial \phi(t)} - \frac{\partial \hat{Q}\left(t\right)}{\partial \phi(t)}\right] \tag{97}$$

The TD(0) algorithm is used for simplicity, using only the previous parameters,

$$\dot{\phi}(t) = -\upsilon(t)\frac{\partial E(t)}{\partial \phi(t)} = \frac{\upsilon(t)}{\Delta t} \times \frac{\partial \hat{Q}\left(e_r(t), F_d(t); \phi(t)\right)}{\partial \phi(t)} \tag{98}$$

where $\upsilon(t)$ is the learning rate. The IRL as convergence is given as

$$\hat{F}_d(t) = \arg\min_{F_d} \hat{Q}(e_r, F_d; \phi) \rightarrow \arg\min_{F_d} \Psi^T(e_r, F_d)\phi \tag{99}$$

where $\phi$ is modified by (98), $\Psi^T(e_r, F_d)$ is derived from RBFNN and $\zeta$ is determined from the K-means algorithm (94).

**Theorem 5.1**. *1) This point of equilibrium is global stability; 2) The learning rate in* (98) *satisfies* $\upsilon(t) \in (0,1]$, $\sum_t^\infty \upsilon(t) = \infty$, $\sum_t^\infty \upsilon^2(t) < \infty$, *the point of equilibrium* $\phi^*$ *exists such that the learning rate in (99) satisfies*

$$\min_{F_d} \hat{Q}(e_r, F_d; \phi) = \min_{F_d} \hat{Q}^*(e_r, F_d; \phi^*) = \Psi^T(e_r, F_d)\phi^* \tag{100}$$

**Proof**. *See in Appendix* 5.1.

Nevertheless, at time t, the received reward cannot give the decision of the policy not until the final results come due to delay. Hereby, the parameter update rule (99) is just one step ahead. To be able to take advantage of the previous states and perform actions online, the eligibility traces are used to alter the temporal value of the $Q(\bullet)$ function.

$$Q\left(t\right) = \begin{cases} e^{\gamma(t-\Delta t)}, & t \le \Delta t \\ 0, & t > \Delta t \end{cases} \tag{101}$$

Then, (101) recalculate the impulse reward at time $t = \Delta t$ and the reward function $r(t + \Delta t)$. (98) is changed as:

$$\dot{\phi}(t) = \upsilon(t)\frac{\zeta(\Delta t)}{\Delta t}\int_{-\infty}^{\Delta t} e^{\gamma(t-\Delta t)}\frac{\partial \hat{Q}\left(t\right)}{\partial \phi(t)}dt \tag{102}$$

Positive infinity is the lower limit of the integral since in the state-action pair. As the eligibility trace of $\phi$ the exponentially integral weight is considered

$$\dot{\phi}(t) = \upsilon(t)\zeta(t)\Delta(t); \quad \dot{\Delta}(t) = -\delta_{\Delta}\Delta(t) + \frac{1}{\Delta t} \times \frac{\partial \hat{Q}\left(e_r(t), F_d(t); \phi(t)\right)}{\partial \phi(t)} \tag{103}$$

The modified RL with the decay factor $\delta_\Delta$ in (103) is the same with $Q(\delta_\Delta)$-function (98) and the convergence (103) is shown in Appendix 5.1.

### 5.3 Validation results

In this section, the slave robot-environment interaction system actuated APAM is used to verify the proposed algorithm, see Figure 24. The environment is located at the position $x_e$ = 35 mm. The initial Cartesian position is $x(0)$ = 5 mm. The parameters for the dynamic environment in (66) are set as $C_e$ = 0.5 N.s.mm$^{-1}$, $K_e$ =2 N.mm$^{-1}$. The distance of the contact force $r_0$ = 165 mm. The desired position is $\theta_d$ = 14 deg, which corresponds to $x_d$ = 39.917 mm. The weight of the ARE (83), for the previous environment parameters with $R$ = 1 and $G$ = 10, is used to calculate the stabilizing gain in (87) as $\kappa_e$ = 0.0025 in the LQR control design is chosen beforehand. The Recursive Least Squares (RLS) algorithm is used [85] to estimate the environment parameters, which can be expressed as:

$$\begin{aligned}
&\hat{\Upsilon}_e(t) = \hat{\Upsilon}_e(t-1) + \left[\mathbb{N}(t)F_e(t) - q^T(t)\hat{\Upsilon}_e(t-1)\right] \\
&\mathbb{N}(t) = \mathbb{C}(t-1)q(t)\left(\beta_{RLS} + q^T(t)\mathbb{C}(t-1)\mu_e(t)\right)^{-1} \\
&\mathbb{C}(t) = \beta_{RLS}^{-1}\left[I - N(t)q^T(t)\right]\mathbb{C}(t-1)
\end{aligned} \tag{104}$$

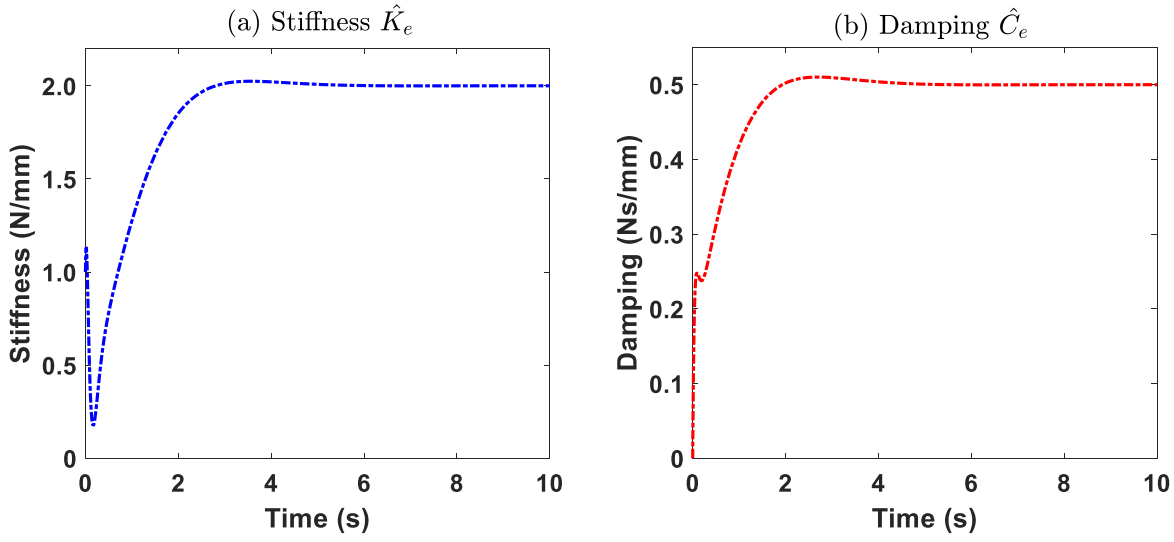


*Figure 25. Environment parameter estimation with RLS.*

where $q = [-\dot{x}, -x]^T$ is the regression vector, $\Upsilon = [C_e, K_e]$ is the parameter vector $0 < \beta_{RLS} \leq 1$ is a forgetting factor, $\mathbb{C}(t)$ is the covariance matrix, $\mu_e = \lambda_{min}(M(x))\ \lambda_{min}(K_p)/3$. In Figure 25, the estimates converge asymptotically to the following values $\hat{K}_e \approx 2.011$ N.mm$^{-1}$ and $\hat{C}_e \approx 0.502$ N.s.mm$^{-1}$ with $T = 0.001$, which stands to $A = -4.006$ and $B = -0.002$. Besides, the tuned gains

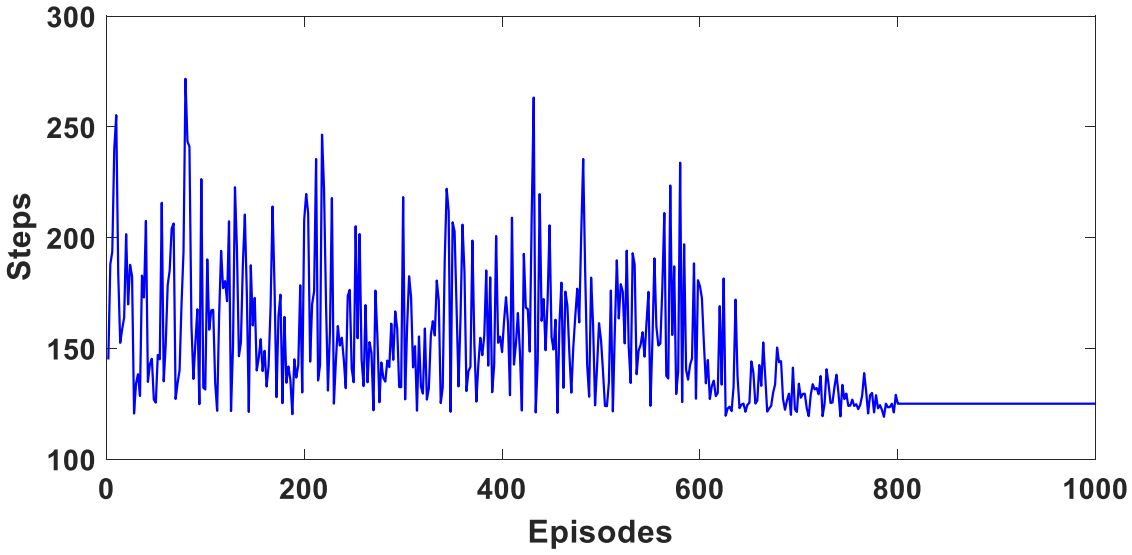


*Figure 26. RL in unknown environments during the learning process.*

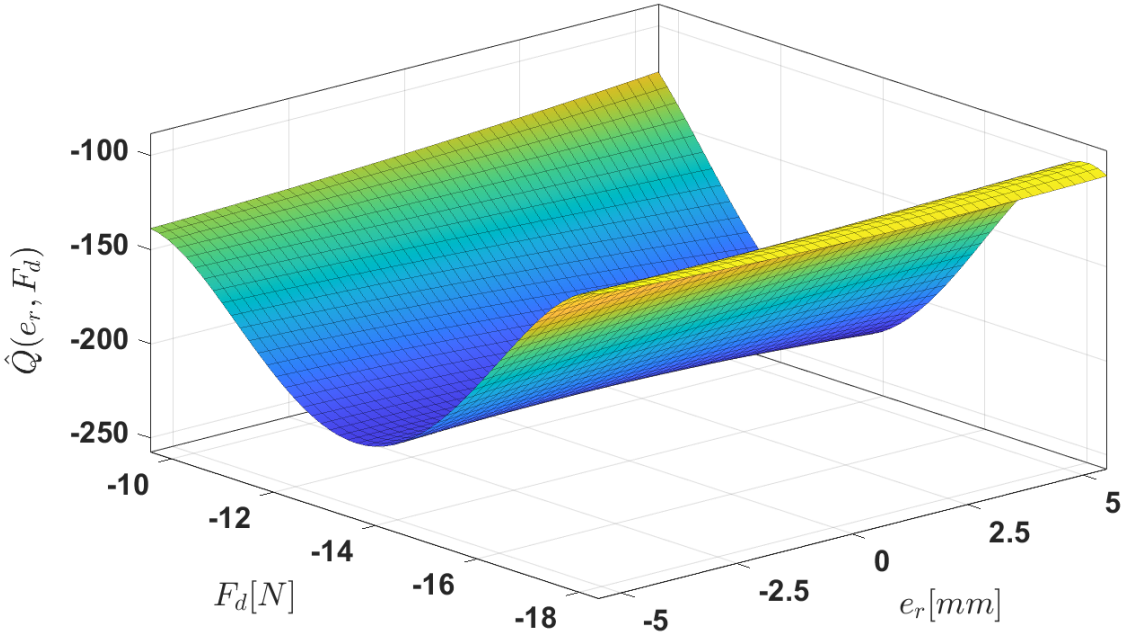


*Figure 27. Learning curves.*

are $C_a$ = 0.5 N.s.mm$^{-1}$, $K_a$ =2 N.mm$^{-1}$. The control parameters are tuning by the trial-error method as $K_{Pf}$ = 0.001, $K_{If}$ = 0.02, $\lambda$ = 0.2, $\rho_1$ = 0.5, $\rho_2$ = 20, $\nu$ = 9/11, $\alpha$ = 5/7.

For the RL algorithms, the following learning parameters are used: learning rate $\upsilon$ = 0.9, discount factor $\gamma$ = 0.9, trace decay factor $\delta_\Delta$ = 0.65, the greedy exploration $\varepsilon$ = 0.1 with a greedy decay factor $\varepsilon$-decay = 0.99. The learning process including 1,000 steps per episode in 1,000 episodes loop. Before training, the better number of clusters is $K$ = 10. The RBF width is 0.5$\beta^2$, $\beta$ = 0.1 for the approximator. For each input, 10 RBFs are set, and each RBF has 10 nodes i.e., one RBF with 10 nodes is used for the tracking state, and one RBF with 10 nodes is for the desired force, so there are 100 hidden nodes. RBF parameters are selected according to the feasible operating range of each input. The RBF centers are set at a certain value or equilibrium point in such a way that the value of the RBF is greater when it is close to that point. The number of RBFs depends on the dimension of the input state, a wrong estimate is obtained with few RBFs, on the other hand, it is obtained a good estimate by increasing the number of RBFs, but

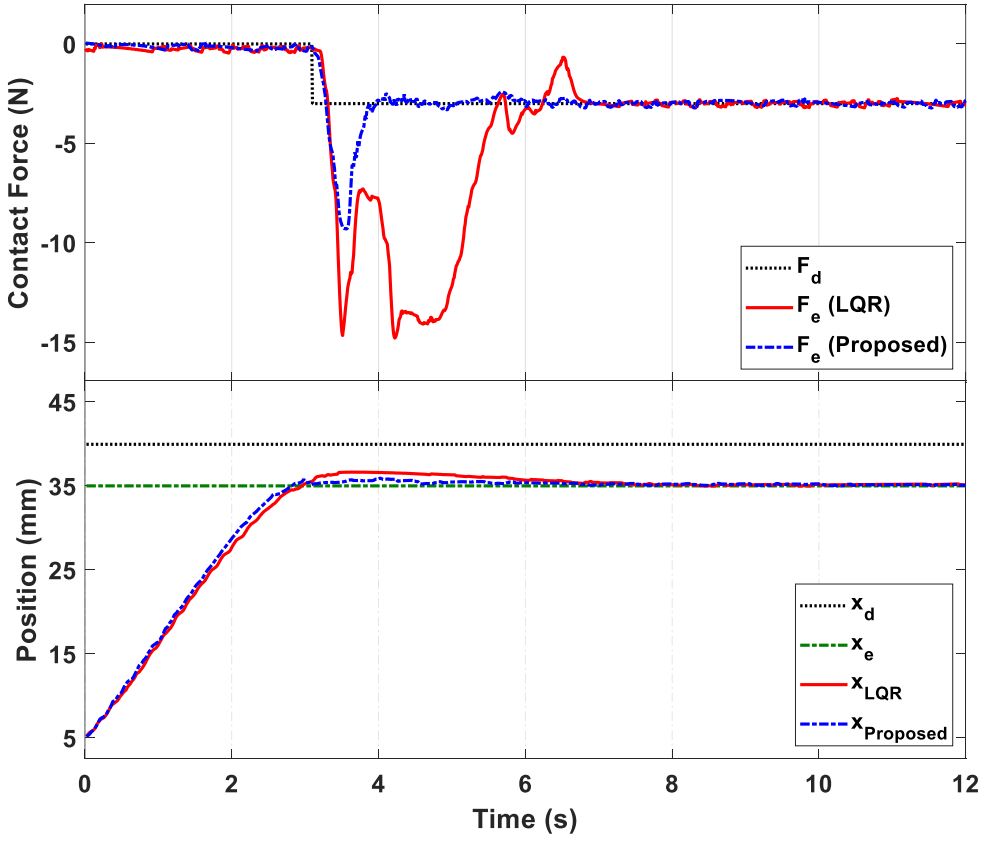


*Figure 28. Desired force and position tracking response.*

it can present overfitting. The use of the trace factor of eligibility δ smooths the surface. In the experiment, actual experiment trials are performed 30 times, each lasting 12 s. The convergent has the approximation-based RL as shown in Figure 26. The suggested method speeds up the learning process by eliminating states that are not useful for regulation of position/force.

Figure 28 shows the effects of the monitoring of location and power. Both the LQR and the proposed RL method converge to the similarly optimum ideal force $F_d^*$ as these results. According to the optimum ideal force $F_d^*$, the PI force regulation adjusts the position $x_d$ to the virtual relation. Digital reference tracking is assured by FTSMC. In the case of the LQR, knowledge of the environmental parameters is mandatory in order to obtain the ARE solution (76). This problem can be easily solved by using any identification algorithm such as the RLS method. However, the experiment trials have to involve three steps including the environmental identification as the first step, then the ARE solution using environmental predictions as the second one, final, apply the robot interaction controller. The proposed RL algorithm, on the other hand, achieves almost optimal performance without the environment dynamics information. To approximate the $Q(\bullet)$ function, the K-means technique is used to partition RBF approximation. Figure 27 shows the learning curve of the $Q(\bullet)$ function and to accelerate the convergence of the proposed control scheme.

The RL leads to be avoided when the robot-environment interaction occurs, which also impacts location tracking as seen in the slight overshoot of Figure 28. It is obvious that, compared to the stiffness of the end effector, the initial condition of the desired position is near or the stiffness of the area is weak, then the desired force would also be small at the transient time. Suddenly, the algorithm adjusts the desired force from zero to the desired optimal force (no interaction exists).

## 5.4 Chapter summary

The suggested RL based on the K-means clustering algorithm achieves near-optimal performance in this session without the environment dynamics information. Via the RL approximation, which is equal to the desired force, the learning impedance model is approximated. Then, a proposed robust controller has been presented to improve the tracking performance of the slave subsystem. The idea of the designed control approach is to obtain through optimal control theory and used in comparison with the method proposed. If the number of RBFs to be used is equivalent to the number of clusters of the K-means algorithm, which generates the input data of the approximators based on the NRBF. In order to verify the

feasibility of the proposed method using the slave robot prototype, experimental studies have been performed. From the comparison of the tracking performance in various uncertainty conditions, the proposed control method shows robust performance against uncertainties and disturbances in the system dynamics and flexible transient response. The stability and performance of the controllers can be reduced, which are unavoidable, due to modeling accuracies.

# Chapter 6

# HUMAN-ROBOT INTERACTIVE CONTROL FOR A APAM CONFIGURATION-BASED HAPTIC INTERFACE USING IRL

## 6.1 Introduction

### 6.1.1 Overview

With the rise in the demand for physical human-robot interaction (HRI) for safety, reliability and efficiency in industry, entertainment, teleoperation, household, and healthcare, etc it implies that practical applications show a broad potential growth. In order to explain this, HRI systems deal with humans who may have very different abilities and capabilities, unlike ordinary industrial robotics where the world is organized and recognized. Therefore, robots should adapt themselves to the level of human abilities and capabilities in HRI systems and make up for potential human errors. To be more specific, a simple setup with the control stick is designed. Using a small damping coefficient, a professional operator can manage faster control stick motions. On the other hand, if the damping coefficient is weak, an inexperienced human operator may not manage rapid movements and can damage the machine or itself. The damping coefficient of the control stick should be calibrated such that the system response is suited to the level of the operator's ability. To ensure conformity with the safety index, human force and precision, this improves the efficiency of the overall HRI system. Another problem is how to provide humanitarian assistance and protection using minimal knowledge of human and robot dynamics while minimizing performance sacrifices in order to design such an intelligent HRI system. In order to be able to accomplish the above, studies of human factors have shown that human learning has two components [99-101] in synchronized motion with a robot. In [102], the proposed control learns a system dynamics model and task performance simultaneously to compensate for nonlinearities of the system as well as guaranteed effective output. Recently, to enhance its efficiency and protection, adaptive impedance techniques were also applied to handle the HRI system problem. According to modifying various variables of the impedance parameters, series of control strategies were introduced, for example, stability [103], the input torque [104, 105], a cost function minimization [106], and human purpose integration [107, 108]. However, the skill variations of different operators have not been taken

into account in these approaches. Impedance regulation techniques have recently been developed for HRI systems, based on human factor studies [109-112]. These approaches take account into the skill differences of humans by changing the robot impedance corresponding with the described human model dynamics. In addition, the stability of the impedance parameter tuning is guaranteed based on a Lyapunov function. In other words, the stability of a regulated device is a basic request and the impedance parameters should be modified to maximize its long-term efficiency. The modification of the impedance model according to the calculation of the operator behavior was carried out by references [59, 113, 114]. These approaches were not concerned with maximizing the long-term combined efficiency of the human-robot systems. In order to determine the optimum impedance model parameters. In [79, 115, 116], an adaptive impedance method is introduced. An intelligent HRI system is built in this chapter with adjustable robot behavior. The human model information or estimate solution as well as describe the characteristics of human impedance is no need in the proposed approach, unlike [109, 110, 117].

### 6.1.2 Proposed idea

According to the above discussion, an intelligent HRI system can be built to achieve this objective by employing model-free control based on learning in order to provide assistance and safety using minimal human/system dynamics. An adaptive operator-cooperative control scheme for the HRI method, which has two loops, is proposed here in this work. Firstly, the inner loop controller does not use any task expertise. Secondly, the outer loop controller contains the operator dynamics information, specific-task performances. In this loop, the goal is to drive the robot to track an impedance model signal as perceived by an operator. The operator, therefore only needs to communicate with the expeditious impedance model. To make up for the unknown nonlinearities of the system, a new neuro-adaptive algorithm has been created. This is not the same as the bulk of the robot impedance control work aimed at guiding a robot to follow a prescribed trajectory and/or causing a prescribed impedance model to follow the trajectory error dynamics. The inner loop architecture does not require trajectory details and the specified robot impedance model information. This leaves the flexibility to integrate task details into the design of an outer loop. Given the configuration of the robot space, the optimal impedance model parameters are needed in the task space to ensure movement observing and also help the minimal effort of the human to perform the task. Last, the optimal impedance model parameters are determined by the LQR solution. In this proposed structure, the unknown human dynamics, as well as the optimum overall performance of the human-robot system, must

be taken into account. RL [118-122] is used without any human information to address the LQR query. In the subsequent parts, the details of the control design are in turn presented.

### 6.2 Developed a Human-Robot Interaction System.

In this section, a preliminary concept design of the human-robot collaboration is introduced in Figure 29. Specifically, $m_h$, $k_h$, $b_h$ are the mass, damping, and stiffness of the human hand-arm, and $m_u$, $b_u$ and $k_u$ represent the mass, damping, and stiffness of the haptic device, respectively. In the robot system, it consists of a pair of the PAMs of an antagonistic configuration are connected to a pulley through a cable. The pulley is toughly linked to the central steel shaft, which can be swiveled in the aluminum frame assisted bearings. Another side of the steel shaft is to set the optical rotary encoder to measure the motion of the control stick. To allow for the measurement of human-robot interaction, a loadcell is mounted between the steel shaft and the handle of the control stick. The control pressures of APAM are achieved by two proportional pressure regulator valves. From the control perspective, the HRI's built control strategy here is inspired by the human-in-the-loop investigation. Firstly, to obviate the human requirement and learn the robot-oriented model, a computed torque controller is used. Secondly, to magnify the human's effort, the assistive inputs are practiced such that the human

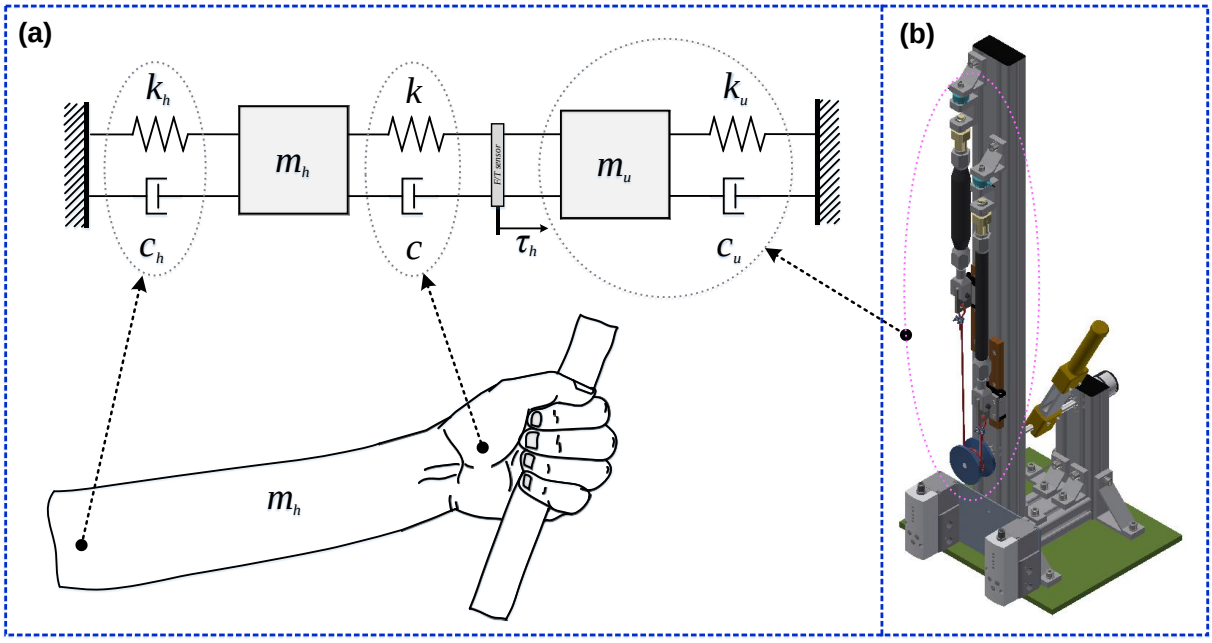


*Figure 29. (a) A human hand model in human-robot interaction. (a) Working principle of the human-robot system based-APAM.*

completes a specified task with the maximum results and minimal effort. The control is built to

be structured with double loops in order to achieve these purposes, as shown in Figure 30. The robot-space control needs no understanding of the mission carried out. The outer one is a task-space loop comprising both the human and the master subsystem dynamics and task awareness. The robot-space architecture is to make the unidentified robot acts the same as the desired impedance model sensed by humans. Hence the human interacts with the impedance model. The trajectory is not necessary to be tracked in the robot-space loop, it means that may offer freedom in the outer loop to combine task information. The learned impedance model can be obtained from the task-space loop in view of the robot-space architecture, which may minimize the tracking error and also assist individuals with minimum effort to perform the task. Taking unknown human dynamics into account is significant, and the expected performance of the human-robot cooperation system depends on the mission. Consider the dynamical model is driven by APAM configuration in (18) Cartesian space [123].

Then the prescribed impedance model can be formed as

$$\theta_m = \frac{K_h \tau_h}{M_d s^2 + C_d s + K_d} \tag{105}$$

where $\theta_m$ denotes the output position of the desired impedance model; $M_d$, $C_d$ and $K_d$ denote the desired inertia, damping, and stiffness parameter matrices, respectively; $\tau_d$ is a general nonlinear disturbance; and $\tau_h$ is the human control effort with the human input force gain $K_h$.

### 6.2.1 Robot-Specific Inner-Loop Control

The aim of the robot-space control is to construct the force $\tau$ in (18) to drive the robot (18) from the human force $\tau_h$ to the Cartesian coordinates $\theta$ following impedance model (105). No information is required for the impedance model parameters. This enables one to separate the robot-space control from the task-space control. Such that, the following model-following error is expected to zero regardless of the values of, $M_d$, $C_d$, and $K_d$.

Defining a force tracking error as follows between the system's output position and the desired impedance model output as follows:

$$e_h = \theta_m - \theta \tag{106}$$

Notice that this is not an error that fits a trajectory. Therefore, the robot-space controller is not a trajectory design unlike other work on robot torque control, this is a model-following design. Thus the task information is no needed in this work. The next section takes all task-specific details into account. Write the input control torque as

$$\tau = u_c - K_h \tau_h \tag{107}$$

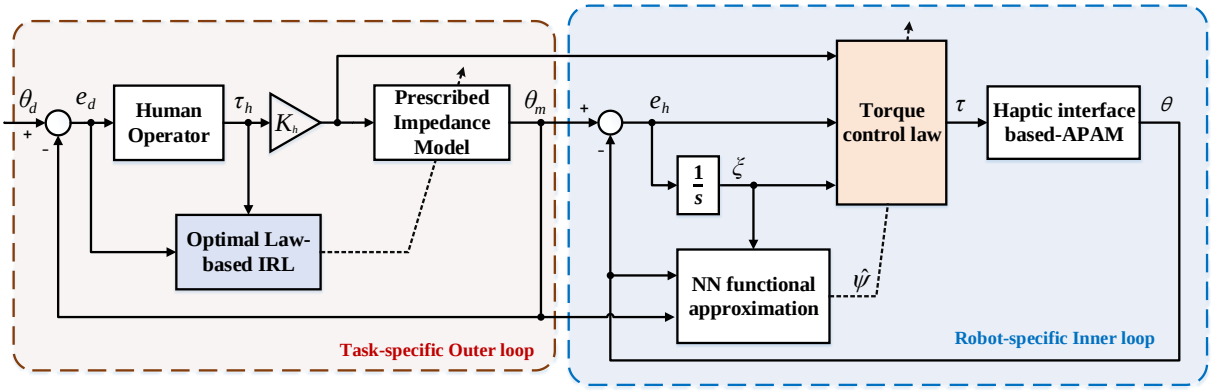


*Figure 30. Control scheme with double loops for the human-robot interaction control.*

The design of a control torque is now needed to make the robot react like the impedance model prescribed (107). The torque of control is defined as follows:

$$u_c = \hat{\psi}(q) + K_s \sigma_h - u_r(t) \tag{108}$$

$$\begin{cases} \hat{\psi}(q) = \hat{W}_1^T \phi(\hat{W}_2^T q) \\ \sigma_h = \dot{e}_h + \mu_1 e_h + \mu_2 \int_0^t e_h(\tau) d\tau \end{cases}$$

where $u_r(t)$ is a robust signal to be defined that provides robustness in the Taylor series in the face of higher-order conditions, $K_s$ is the control gain, $\sigma_h$ is the sliding mode error, and $\hat{\psi}(q)$ is the NN with $q = [\theta, \dot{\theta}, \dot{\theta}_m, \ddot{\theta}_m, e_h, \dot{e}_h, \xi]^T$, $\xi = \int_0^t e_h(\tau) d\tau$ and an element compensation $\psi(q)$ as:

$$\psi(q) = M(\ddot{\theta}_m + \mu_1 \dot{e}_h + \mu_1 e_h) + C(\dot{\theta}_m + \mu_1 e_h + \mu_2 \xi) + K\theta_m + \tau_d \tag{109}$$

In detail, the following form is the two-layer NN, which is an approximation of the continuous function $\psi(q)$ on a compact set.

$$\psi(q) = W_1^T \phi(W_2^T q) + \xi(q) \tag{110}$$

where $W_1$, $W_2$, $\varepsilon$ are a matrix of first, second-layer NN weights and the error of the functional approximation, respectively. The $W_1$ and $W_2$ are nominal weight factors. Consequently, $\psi(q)$ consists of $W_1$ and $W_2$, which are approximated by $\hat{W}_1$ and $\hat{W}_2$ respectively. We obtain.

$$Z = \begin{bmatrix} W_1 & 0 \\ 0 & W_2 \end{bmatrix} \Rightarrow \hat{Z} = \begin{bmatrix} \hat{W}_1 & 0 \\ 0 & \hat{W}_2 \end{bmatrix} \tag{111}$$

The ideal NN weights are presumed to be bound by $\|Z\| \leq \bar{Z}$. The following theorem shows that the suggested control input (109) with the instruction given by (110) ensures that the model is bound by the error $e_h$ and the NN weights.

**Theorem 6.1**: *Consider the dynamics of the system* (18) *and the impedance model defined (107). Let the control input be designated as (109) and* (110)*. Let the NN weights update rule be given by*

$$\dot{\hat{W}}_1 = F\hat{\phi}\sigma_h^T - F\hat{\phi}'\hat{W}_2^T q\sigma_h^T - kF \| \sigma_h \| \hat{W}_1 \tag{112}$$

$$\dot{\hat{W}}_2 = Gq(\hat{\phi}\hat{W}_1\sigma_h)^T - kG \| \sigma_h \| \hat{W}_2 \tag{113}$$

*where* $\hat{\phi} = \phi(\hat{W}_2^T q), \hat{\phi}' = d\phi(y)/dy|_{y=\hat{W}_2^T q}, F = F^T > 0, G = G^T > 0$ *and k is a small positive design parameter. Let the robustifying term be*

$$u_r(t) = -K_q(\| \hat{Z} \| + \bar{Z}) \tag{114}$$

*where* $K_q$ *is a positive value. Then,* $e_h(t)$ *in* (106) *and the approximate weights of the NN are essentially equally bound*.

**Proof**: *See in Appendix* 6.1.

### 6.2.2 Task-Oriented Outer-Loop Control

The design of the outer task loop controller is illustrated in Figure 30 in this section. In the previous section, Theorem 6.1 was shown that the robot-specific controller makes the nonlinear unknown robot (18), which follows the simplified impedance model (107) as interpreted by the operator. The optimal parameters given in (107) of the impedance model are determined to lend the human with minimal effort to perform tasks as well as a minimal tracking error. In detail, the task-space controller aims to find the optimum values of the specified impedance parameters $B_d$, $K_d$, the operator gain $K_h$ (or $M_d$ if $K_h$ = 1) in (105) to minimize the human control effort $\tau_h$ and optimize the tracking performance depending on the task. So, the issue of optimizing the robot impedance model parameters is translated into an output feedback control and then RL is used to drawback the given problem without the human dynamics model requirement. According to [99], the human transfer function from $e_d$ to $\tau_h$ is assumed to be

$$G(s) = \frac{e_d}{\tau_h} = \frac{\kappa_p + \kappa_d s}{1 + k_e s} \tag{115}$$

where $\kappa_p$, $\kappa_d$ and $k_e$ are the control gains, which are no determined before.

In order to drive the tracking position error to zero, the adaptive impedance loop that defines the optimum impedance parameters is used. The optimal prescribed impedance parameters in (107) are calculated for a given human task in order to minimize the tracking position error and the human effort force. After translating the optimal model parameters into an optimal control problem, Figure 30 depicts the block diagram of the outer loop. The online learning algorithm

based on the integral RL (IRL) method is successively implemented in order to find a suboptimal output feedback controller by minimizing a predefined performance index, as the following.

***a) Linear Quadratic Regulator solution***

The tracking error is thus defined as the tracking error using the output position $\theta_m$ of the desired impedance model (105) and the initially desired subsystem command $\theta_d$.

$$e_d = \theta_d - \theta_m \in \mathbb{R}^n \tag{116}$$

$$\bar{e}_d = \bar{\theta}_d - \bar{\theta} = [e_d^T \quad \dot{e}_d^T]^T \in \mathbb{R}^{2n} \tag{117}$$

with $\bar{\theta} = [\theta_m^T \quad \dot{\theta}_m^T]^T \in \mathbb{R}^{2n}, \bar{\theta}_d = [\theta_d^T \quad \dot{\theta}_d^T]^T \in \mathbb{R}^{2n}$.

Thus, the human transfer function (115) can be rewritten as

$$\dot{\tau}_h = A_h \tau_h + B_h \bar{e}_d \tag{118}$$

where $A_h = -k_e^{-1}, B_h = k_e^{-1}\begin{bmatrix} \kappa_p & \kappa_d \end{bmatrix}$ and $\bar{e}_d$ is defined in (117).

According to the definition in (117), let define the cost-function

$$J_m = \int_t^\infty \left( \bar{e}_d^T Q_d \bar{e}_d + \tau_h^T Q_h \tau_h + u_e^T R u_e \right) d\chi \tag{119}$$

where $Q_d = Q_d^T > 0$, $Q_h = Q_h^T > 0$, $R = R^T > 0$, and $u_e$ is a control input, as follows:

$$u_e = K_1 \bar{e}_d + K_2 \tau_h \tag{120}$$

Here, the efficiency index (119) relies linearly on the tracking error $\bar{e}_d$, the human effort $\tau_h$, in which $K_1$ contains $B_d$, $K_d$ and $K_2$ contains $M_d$. Next, the augmented state is defined as

$$X = \begin{bmatrix} \bar{e}_d \\ \tau_h \end{bmatrix} \in R^{3n} \tag{121}$$

Therefore, the cost function (119) can be formed as

$$V_7(X(t)) = J_m = \int_t^\infty (X^T Q X + u_e^T R u_e) d\chi \tag{122}$$

where $Q = \text{diag}(Q_d, Q_h) \geq 0$, such that $(Q^{1/2}, A)$ is detectable and $u_e = KX$ with $K = [K_1 \; K_2]$. Based on the augmented state (119), the prescribed impedance model (105) can be obtained as

$$\dot{\bar{\theta}} = A_q \bar{\theta} + B_q u \tag{123}$$

where $A_q = \begin{bmatrix} 0 & I_{n\times n} \\ 0 & 0 \end{bmatrix}; B_q = \begin{bmatrix} 0 \\ I_{n\times n} \end{bmatrix};$ and $u$ is the control input as formed:

$$u = M_d^{-1}(-K_q \bar{\theta} + K_h \tau_h) \tag{124}$$

where $K_q = [K_d\ B_d]$.

Substituting (117) into (124) gives

$$\begin{aligned} u &= M_d^{-1}(K_q[\bar{e}_d - \bar{\theta}_d] + K_h\tau_h) \equiv u_e + u_d \\ &\begin{cases} u_e = M_d^{-1}(K_q\bar{e}_d + K_h\tau_h); \\ u_d = -M_d^{-1}K_q\bar{\theta}_d. \end{cases} \end{aligned} \tag{125}$$

To ensure perfect tracking, The below steady-state term is employed:

$$\dot{\bar{\theta}}_d = A_q\bar{x}_d + B_q u_d \tag{126}$$

And taking the derivative of $\bar{e}_d$ and substituting (117) into (126) gives

$$\dot{\bar{e}}_d = A_q\bar{e}_d + B_q u_e \tag{127}$$

According to the augmented state (118), (121) and (127), it obtains

$$\dot{X} = AX + Bu_e \tag{128}$$

where new augmented matrices $\dot{X} = \begin{bmatrix} \dot{\bar{e}}_d \\ \dot{\tau}_h \end{bmatrix}, A = \begin{bmatrix} A_q & 0 \\ B_h & A_h \end{bmatrix}, B = \begin{bmatrix} B_q \\ 0 \end{bmatrix}$, $u_e$ is the optimal feedback control in (125), which can be rewritten as

$$u_e = M_d^{-1}(K_q\bar{e}_d + K_h\tau_h) = -KX \tag{129}$$

where $K$ is the optimal value to minimize the cost function (119). And based on the algebraic Riccati equation (ARE) [83] to obtain $P$, then the control gain is defined as follows:

$$K = M_d^{-1}\begin{bmatrix} K_q & K_h \end{bmatrix} = R^{-1}B^T P \tag{130}$$

$$A^T P + PA + Q - PB^T R^{-1}BP = 0 \tag{131}$$

The following Riccati differential equation must be solved

$$-\dot{P} = A^T P + PA + Q - PB^T R^{-1}BP; \qquad P\left(t_f\right) = P_{t_f} \tag{132}$$

Its solution will converge to the solution of the ARE as $t_f \to \infty$.

**Theorem 6.2***: An LQR problem is the optimal feedback control (130) to reduce the output index (124) according to the augmented method (130), and its solution is given by* [119]*:*

$$u_e^* = \underset{u_e(\chi), t\le\chi\le\infty}{\arg\min}\, V\left(t, X(t), u_e(\chi)\right) = -R^{-1}B^T PX \tag{133}$$

*if there exists a symmetric positive-definite matrix $P = P^T > 0$ satisfying the Riccati equation* (131)*. Then, substituting* (133) *into the dynamic system* (128)*, it obtains*

$$\dot{X} = \left(A - B\left(R^{-1}B^T P\right)\right)X \tag{134}$$

*being globally exponentially stable about the origin.* (134) *guarantees that all the variables of the closed-loop system are bounded and the tracking performance is achieved.*

**Proof***: See in Appendix* 6.2.

***b) Optimal Parameters of the Prescribed Impedance Model Using IRL***

The RL technique is a quantitative approach to learning from encounters with the surrounding environment and how an agent or actor can take steps to maximize the cost of their long-term environmental interactions, inspired by learning mechanisms found in mammals. In the control sense, the dynamic system is the environment, the agent corresponds to the controller, and the control signals correspond to the actions. The aim of the RL is to find a strategy that minimizes the long-term costs anticipated. The RL does not require exact knowledge of system dynamics, unlike conventional optimal control solutions. Instead the RL relies heavily on knowledge gained from monitoring actions and engaging directly with the complexities of the system.

In order to satisfy persistently exciting (PE) qualitatively, a small exploratory probing noise consisting of sinusoids of varying frequencies are added to the control input to ensure the adequate exploration of state space, which is necessary for proper convergence to the optimal value function [124, 125]. Solving (133) includes the knowledge of matrix A in (130) and therefore the comprehension of the human model. In order to solve the optimal control of linear systems, several model-free RL algorithms were built without needing any knowledge of system dynamics[96, 126, 127]. Let K be the system's stabilizing state-feedback gain (130) such that (136) is a stable system of closed loops. Then the corresponding quadratic infinite-horizon cost is given by

$$V_7(X(t)) = \int_t^\infty X^T(\chi)\left(Q + K^T R K\right) X^T(\chi) d\chi = X^T P X \tag{135}$$

where $P$ is the real symmetric positive definite solution of the Lyapunov matrix equation as $(A - BK)^T P + P(A - BK) = -(K^T R K + Q)$. Then $V_7(X(t))$ serves as a Lyapunov function for (128) with controller gain $K$. The value function (135) can be written in the following form.

In this chapter, the integral RL (IRL) Bellman equation [125, 128, 129] is used, instead of the Lyapunov equation, to evaluate a policy without requiring any knowledge of the system dynamics. Note that for time interval $\Delta T > 0$, the value function (122) satisfies

$$V_7(X(t)) = \int_t^{t+\Delta T} X^T(\chi)\left(Q + K^T R K\right) X^T(\chi) d\chi - V_7(X(t+\Delta T)) \tag{136}$$

In terms of the steady-state, it is well known that the value function for the LQR problem is quadratic. The use of this quadratic form in (138) results in the equation of IRL Bellman

$$X(t)^T PX(t) = \int_t^{t+\Delta t} X^T(\chi)\left(Q + K^T RK\right) X^T(\chi) d\chi + X^T(t+\Delta t) PX(t+\Delta t) \tag{137}$$

Using (139) to find an improved policy for the policy evaluation phase and a revised law in the form of (138), the following IRL-based algorithm is obtained for resolving (133).

***Algorithm* 1:** *Online IRL Solution for Outer-loop Control*

1) Set $u_e{}^0 = -K_1{}^0 X$ for an admissible control input
2) Policy evaluation: find the $P^i$ using the off-policy Bellman equation to give a control policy $u_e{}^i$,

$$X(t)^T P^i X(t) = \int_t^{t+\Delta t} X^T(\chi)\left(Q + \left(K^i\right)^T RK^i\right) X^T(\chi) d\chi + X^T(t+\Delta t) P^i X(t+\Delta t) \tag{138}$$

3) Policy improvement: the control policy in 2nd step is updated by

$$u_e^{i+1} = -R^{-1} B_1^T P^i X. \tag{139}$$

For continuous-time systems, Algorithm 1 formulates a new policy iteration algorithm. An initial K1 stabilizing control gain is necessary. Note that the implementation of this algorithm does not include the matrix A of the plant. The proof of convergence of Algorithm 1 is provided in Appendix 6.2.

**c) Online implementation of the adaptive algorithm based on policy iteration**

The implementation of the iteration scheme given by (135) requires knowledge only of the *B* matrix that appears directly in the policy update. The system *A* matrix information is embedded in the states $x(t)$ and $x(t + \Delta t)$, so the system matrix is never needed for either of the two stages of the policy iteration scheme to be computed.

The term $\Phi^T(t)P^i\Phi(t)$ is written to find the parameters (matrix $P^i$) of the cost function associated with the policy $K^i$ in (138) as

$$\Phi(t)^T P^i \Phi(t) = (\bar{p}^i)^T \bar{\Phi}(t) \tag{140}$$

where $\bar{\Phi}(t)$ denotes the quadratic polynomial basis vector of the Kronecker product with the elements $(\Phi^i(t)\ \Phi^j(t))^{i=1,n;j=i,n}$ and $\bar{p} = v(P)$ with $v(\bullet)$ a vector-valued matrix function. This works on symmetric matrices and returns a column vector by stacking the components of the symmetric matrix's diagonal and upper triangular portions into a vector in which the off-diagonal components are taken as $2P^{ij}$ [131]. Substituting (140) into (138), which is rewritten as

$$(\bar{p}^i)^T\left(\bar{\Phi}(t)-\bar{\Phi}(t+\Delta t)\right)=\int_t^{t+\Delta t}\left(\Phi^T(\chi)(Q+(K^i)^T RK^i)\Phi(\chi)\right)d\chi \tag{141}$$

The vector of unknown parameters and $\bar{\Phi}(t)-\bar{\Phi}(t+\Delta t)$ is in this equation and function as a regression vector $\bar{p}^i$. Often known as the reinforcement on the time interval, the right-hand side goal function denoted $\Xi(\bar{\Phi}(t),K^i)$ on the time [$t$, $t$ + $\Delta t$]), $\Xi(\bar{\Phi}(t),K^i)=\int_t^{t+\Delta t}\Phi^T(\chi)$ ($Q$ + $(K^i)^T RK^i)\Phi(\chi)$ $d\chi$ is measured. Considering $\dot{V}_m(t)$ = $\Phi^{\mathrm{T}}(t)Q\Phi$ ($t$) + $u^{\mathrm{T}}(t)Ru(t)$ as a definition for a new state $V(t)$, augmenting the system (128), the value of $d(\bar{X}(t),K^i)$ can be measured by taking two measurements of this newly introduced system state since $\Xi(\bar{\Phi}(t),K^i)$ = $V_m(t + \Delta t)$ − $V_m(t)$. This new state signal is the output of an analog integration block having as inputs the quadratic terms $\Phi^T(t)Q\Phi(t)$ and $u^{\mathrm{T}}(t)Ru(t)$ which can also be obtained using an analog processing unit. The parameter vector $\bar{p}^i$ will then yield the matrix $P^i$, and it is found by minimizing the error between the target function, $\Xi(\bar{\Phi}(t),K^i)$, and the parameterized left-hand side of (141). Assessing the right-hand side at $N \geq n(n + 1)/2$ (the number of independent elements in the matrix $P^i$) points $\bar{\Phi}^i$ in the state space, the least-squares solution is obtained as

$$\bar{p}^i=(\Phi\Phi^T)^{-1}\Phi\Upsilon \tag{142}$$

where $\Phi = [\Phi_\Delta^{-1}\ \Phi_\Delta^{-2}\ \ldots\ \Phi_\Delta^{-N}]$; $\Upsilon = [\Xi(\Phi^{-1},K^i)\ \Xi(\Phi^{-2},K^i)\ \ldots\ \Xi(\Phi^{-N},K^i)]^T$; $\Phi_\Delta^{-i}(t) = \Phi^{-i}(t) - \Phi^{-i}(t + \Delta t)$. After a sufficient number of data points are obtained along a single state trajectory, with the usual existence of an excitation requirement, the least-squares problem can be solved in real-time.

## 6.3 Validation results

### 6.3.1 Simulation results

Simulation and experimental results are given in this section to check the efficiency of the system proposed. Hereby, a haptic interface-actuated APAM device acts like a given impedance model using the robot-space control design process, see chapter 2. In the following, it is first seen how the suggested method of robot-space control design makes the robot, regardless of its impedance parameters, function like a prescribed impedance model. Then, how to find the optimized values of the impedance parameters recommended making the tracking error correct.

The human force in the inner loop is believed to be sinusoidal in both directions. For the specified impedance model, a set of impedance gains is assumed to imply that the master device behaves like the impedance model regardless of the impedance model parameters. The NN parameters are turned $K_s$ = 20, $F$ = 10, $G$ = 1, $\mu_1 = \mu_2$ = 5, $k$ = 0.1 and $\bar{z}$ = 100. The hidden-

layer neurons were selected 10 layers. It is easy in the software to specify a new number of hidden layer neurons, and each simulation run took of 60 s. Similar simulation iterations may be made to determine effective numbers for the various design gains. There was no need for the initial NN training or learning process and the weights were simply initialized at zero. Figure 31 shows the error between the trajectories of the impedance model and the robot system.

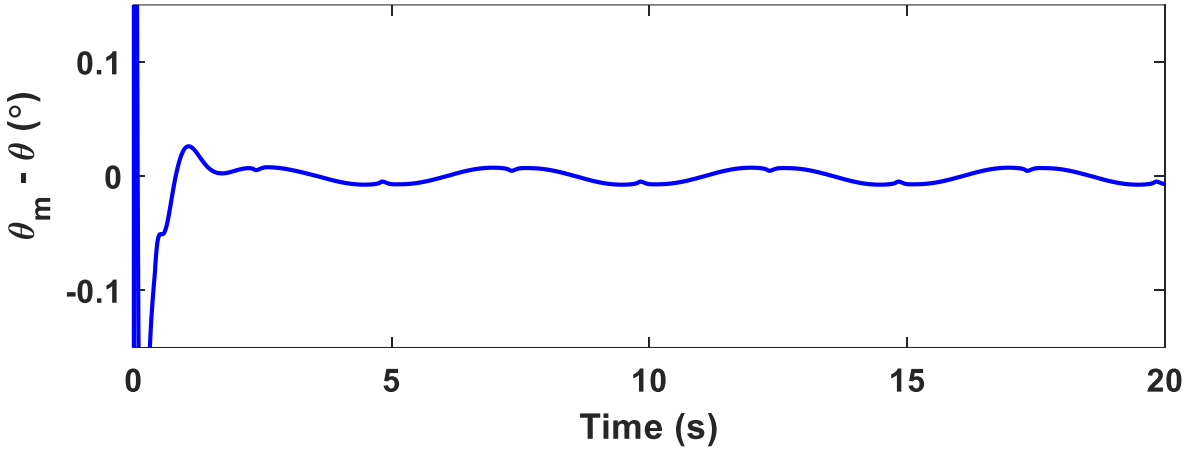


*Figure 31. The tracking error of the robot trajectory and the prescribed impedance model.*

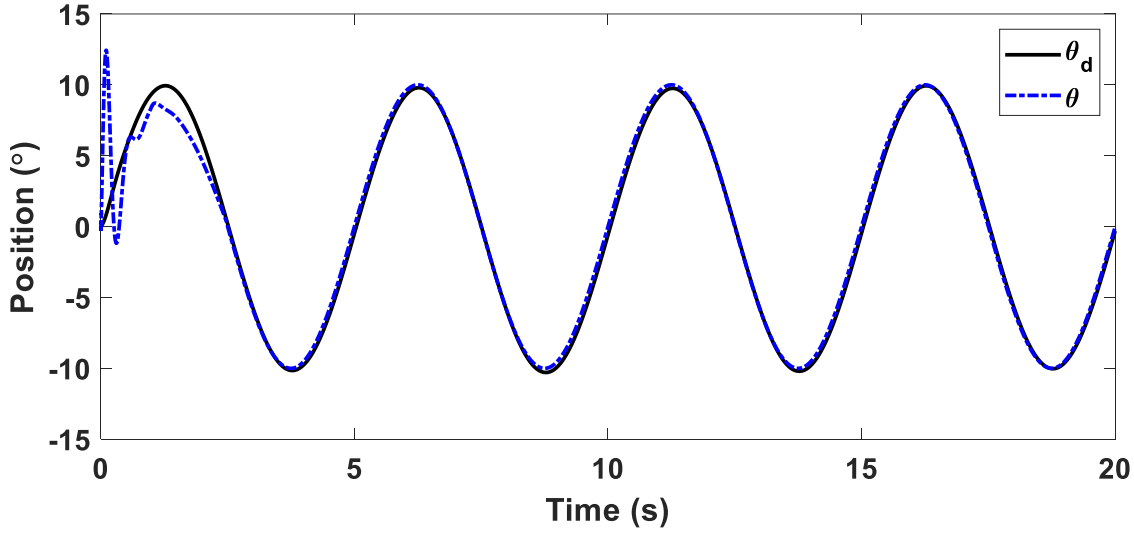


*Figure 32. Reference versus the output trajectory during and after learning.*

In the outer loop, a point-to-point trajectory is assumed to be sinusoidal by setting a goal point with the human transfer function parameters, in turn, $\kappa_p = 20$, $\kappa_d = 10$ and $k_e = 0.18$ s. The objective is to move $\theta$ to the desired point $\theta_d$. That is, $\theta_d = 10\sin(0.2\pi t)$. Notice that in general, these parameters are not constant and can differ from human to human. Using the IRL in (142) the impedance model parameters are now optimal. The proposed online IRL Algorithm 1 has now been shown to have the same set of optimal parameters and thus the same output as the offline method, but without requiring knowledge of human dynamics. Assuming $\kappa_d = K_{nd} + \Delta K_d$ and $\kappa_p = K_{np} + \Delta K_p$, where $K_{nd}$ and $K_{np}$ are nominal expert human parameters and $\Delta K_d$ and $\Delta K_p$ shift from one operator to another. It is worth noting that matrix $A_q$ in $A$ in (128) is known and so the ARE (131) can be solved by matrix $A$ including only nominal human dynamics values. This gives us a very suitable initial value for the kernel matrix $P$ of the value function. The interval of reinforcement is chosen as $\Delta t = 0.02$ s. During the learning process, Figure 32 shows the performance of the device and the reference trajectory. From the beginning of the simulation, the proposed algorithm begins the learning process and finishes it after 2.5 s, when the control policy is modified. After that as needed, the performance of the device is very close to the reference trajectory.

### 6.3.2 Experimental results

On a haptic interface device shown in Figure 8, a realistic experiment is now being conducted. The operator holds the control stick in this experiment to carry out a push-pull movement towards the blue and red points along the pulley axis mounted by the optical encoder. Using an interactive load cell connected between the APAM joint and the control stick, human strength is measured. The controller is implemented using the framework of the real-time control system, which runs at 1000 Hz and communicates with the sensors and actuators. In comparison, the system is applied to the impedance controller without the RL. The impedance model parameters in (105) are $M_d = 1$ Kg, $B_d = 7.18$ N.s.mm$^{-1}$, $K_d = 15.76$ N.mm$^{-1}$, $K_h = 0.046$, which are chosen beforehand. The impedance model in the inner loop illustrates the trajectory of the robot in Figure 33. The comparison experiment results of the outer loop controllers are shown in Figure 34. The real trajectory does not track the desired trajectory perfectly from this figure at the beginning of the experiments, since the prescribed impedance model is initialized with a set of non-optimal parameters. The outer loop controller learns the optimal impedance parameters after a short period of interaction and thus the HRI device successfully monitors the desired trajectory. It implies that human-robot collaboration can be done perfectly, and with little deviation, the actual trajectories track the desired trajectory. Figure 35 demonstrates how

the human force is decreased after the learning is carried out and the outer-loop controller finds the optimum set of the specified impedance model. It is evident that the efficiency of the control is worse than the suggested adaptive control using IRL. In addition, under a restriction for initial

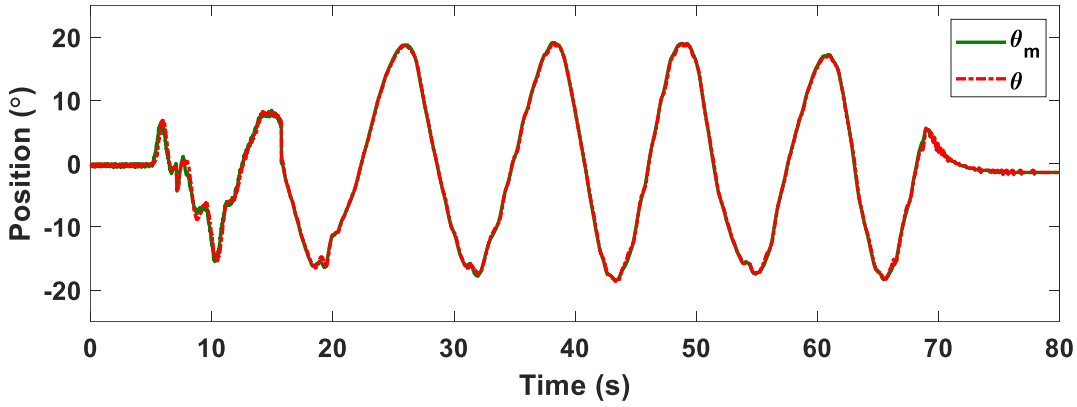


*Figure 33. The output trajectory and the prescribed impedance model in the inner loop.*

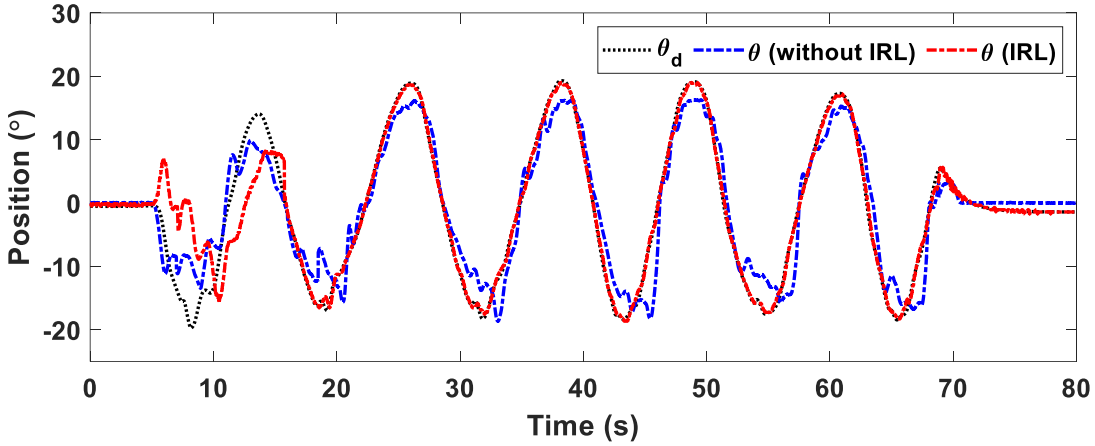


*Figure 34. The desired trajectory and the output trajectory in the outer loop.*

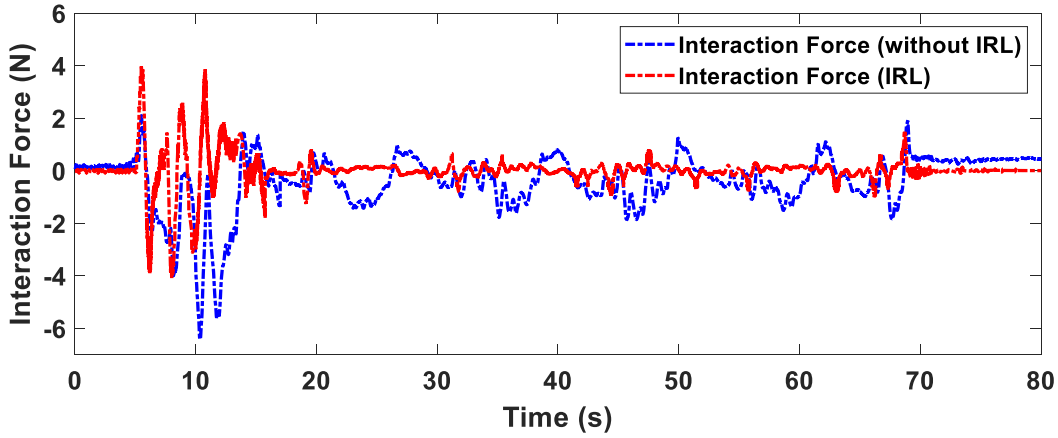


*Figure 35. Interaction force.*

position errors, the trajectory tracking is done without violating the constraint and all closed-loop signals remain constrained.

## 6.4 Chapter summary

To build an integrated assistive human-robot interaction device, a novel control approach is presented. There are two loops in the proposed control system. In the inner loop, to make the unknown nonlinear robot function like a prescribed impedance model, a neuro-adaptive controller is used. The suggested inner loop does not require the task's expertise or the impedance parameters prescribed. The robot-specific control design is thus decomposed from the task-specific design. The optimum parameters of the prescribed impedance parameters are found in the second loop, which involves the person, the robot and their interaction, depending on the human capacity and the task provided to help the human being perform the task with less effort and optimal efficiency. Finally, detailed studies have been carried out to check the efficacy of the proposed control in the cooperative human-robot mission.

# Chapter 7

# FORCE SENSORLESS REFLECTING CONTROL FOR BILATERAL HAPTIC TELEOPERATION SYSTEM

## 7.1 Introduction.

### 7.1.1 Overview

In recent years, the teleoperation techniques have been developed to reach a high level of sophistication and rapidly played an important role in numerous practical applications, such as robotic surgery, nuclear source detection, robotic construction [11, 55, 58, 132-137]. Besides, these systems required the possibility of physical interaction with the remote environment to provide the feeling of the present there, called haptic. From a design perspective, many actuators are employed in the haptic teleoperation systems to supply sensory feedback. Specifically, motor-driven actuators [138] are widely used given their characteristics of safety and capability of providing suitable force for small haptic devices according to the required state. However, they are incompatible with the applications that have extensively magnetic interference because of producing their own magnetic fields. Meanwhile, the pneumatic artificial muscle actuators (PAMs) possessed the advantages of a lightweight, reasonable safety and a high power-to-weight ratio, which have been considered as one of the most promising solutions for haptic devices in many applications such as robot-assisted surgery, rescue robots, etc [3], [16, 139]. In this work, a bilateral haptic teleoperation system actuated by a pair of antagonistic PAM (APAM) configuration was first designed.

The teleoperation system can be called a bilateral system as the human not only operates the master system and transmits the command trajectories to the slave system and interacts with an environment but the interaction signals between the slave and the environment can also be feedbacked to the human through the master. Both master and slave robots are controlled bilaterally with the same actions of force and motion movements. The bilateral teleoperation hereby is normally assessed through two critical indices of stability and transparency. To be more specific, stability requires the closed-loop system to be stable under different environmental conditions. Transparency presents how well the haptic feedback cues provide the human operator slave-environment interaction. Numerous control strategies have been

introduced to balance the trade-off between these indices [7], [8]. Besides, much effort has been made to seek robust control methods to obtain satisfactory control performance. For example, based on the system model [9], the conventional PID controller for a robotic arm was designed. An advanced PID controller combined with a neural network scheme [7] and an intelligent phase plane switching controller [10]. However, the above approaches are only efficient in several specific regions without high nonlinearity and time variation of system parameters. To improve these restrictions, a variety of advanced methods was proposed such as a fuzzy approach [11], [12], a neural network [13], a time-delay-based control [14], [15] and a radial basis function neural network [16]. Nonetheless, the above approaches require complicated algorithms or a large number of tuning parameters and depend largely on the experience of experts. It is worth noting that sliding mode control (SMC) is one of the most powerful methods to enhance the nonlinear systems with uncertainties and disturbances [17], [18]; however, the SMC can only asymptotically achieve stability for the controlled system. Taking advantage of SMC, the terminal SMC (TSMC) has been developed with its superiorities such as finite-time convergence and high tracking accuracy [19] - [23]. Successively, the modified version of TSMC namely the fast nonsingular TSMC (FNTSMC) is developed to not only guarantee a fast convergence rate in the sliding phase when the system states are far away from the equilibrium [24], but also avoiding a singularity of switching from terminal sliding surface to linear sliding surface [25]. From a haptic control perspective, the APAM actuated haptic device is a challenge since its dynamic contains high uncertainties.

Additionally, the transparency of a bilateral teleoperation system requires not only accurate master-slave position tracking but also exact force perception. Thus, force information is a crucial element to enhance the robotic system performance with a force reflecting control scheme [58]. The force sensing technique plays a vital role in such force control designs since the control performance is affected by the precision of the force detection. In conventional approaches, the force information is obtained from force sensors. However, the usage of force sensors is not always available or feasible in practical applications owing to some drawbacks such as high cost, inconvenience to install, the capability of being damaged by collisions and narrow bandwidth due to their sensitivity to large noise [55, 140]. Therefore, the force information can be obtained by force observers and has been proposed in many approaches [141-143]. In [56], a nonlinear disturbance observer (NDOB) is a well-known estimation method for estimating the external force signal of the bilateral teleoperation system. In another approach presented in [57], an extended active observer (EAOB) estimated both force and state

information to improve control performance by removing the effect of measurement noise and parametric uncertainties. An extended state observer with an adaptive gain was also designed to obtain the force and state information without using force sensors in the bilateral teleoperation system in [58]. Even though these observers provide a simple way to estimate the external force, their disadvantage is the effects of noise as the velocity computation could deteriorate the force sensing. To handle this issue, the combination of force observer with a Kalman filter was introduced in [59], [60]. However, the Kalman filter cannot guarantee the finite-time convergence of the estimation errors, which could lead to difficulty in ensuring global control stability. With the wish to develop a simple, fast and robust online estimation, the novel adaptive force observer (AFOB) is proposed to estimate external forces without using any load cell. It is worth noting that the globally exponential stability still guarantees the good performance of the bilateral teleoperation system. That results are used to design robust controllers for the bilateral teleoperation in the presence of parameter uncertainties.

### 7.1.2 Proposed control idea of the bilateral haptic teleoperation

According to the above analysis, this chapter proposes control schemes based on a combination of AFOB and FNTSMC scheme in a manipulated smart deburring regardless of a dynamic model and parametric uncertainties for the master and slave systems, which can guarantee the stability with fast convergence error and tight tracking performance. Motivated by the preceding discussions, as well as shortcomings in the existing literature, the main originalities of this chapter can be summarized as follows.

- From my knowledge, there are no studies for the bilateral haptic teleoperation based on the APAM configuration. Moreover, this work proposed for the first time the hybrid control based on a fast finite-time NTSMC and AFOB. The objective of this work is to investigate the interesting above-mentioned properties of the proposed approach.
- The stability and finite-time convergence characteristic of the closed-loop control are theoretically analyzed by the Lyapunov approach.
- The experimental results are conducted on a designed PAM actuated haptic system and the effectiveness of the proposed control method is verified in the different working conditions.

## 7.2 The Nonlinear Bilateral Controller Design

In this section, the bilateral control of force and motion in the PAM based haptic system is presented. The concept of bilateral control is introduced on the basis of the exchanged information between the master side and the slave side. The force sensing to the human operator

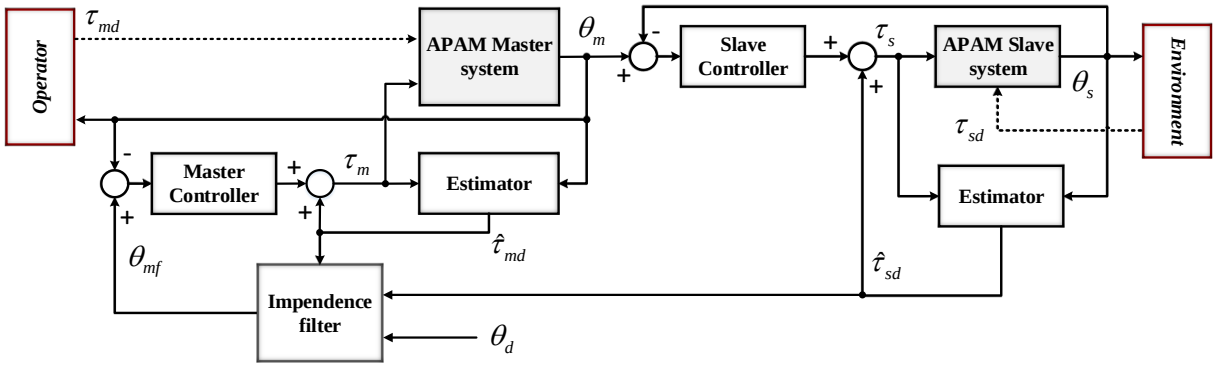


*Figure 36. The proposed bilateral control scheme for APAM actuated haptic system.*

is supplied through the master system. Meanwhile, the slave system is employed to interact with environments. The bilateral control design for the overall haptic system can be achieved the global stability of the closed-loop system. Particularly, the PAM based slave system $\theta_s$ can track the desired trajectory of the master side $\theta_m$ with guarantee the error as small as possible. Consequently, the great transparency is demonstrated through a good impedance performance of the master system so that the human can have the actual feeling of the contact force with the environment vividly when the system is in a steady state.

To start with, the proposed control algorithm of a bilateral haptic teleoperation system is shown in Figure 36. The operator applied torque and the environment torque is approximated using the proposed adaptive force observers. Then, the estimated contact force $\hat{\tau}_{sd}$ is transmitted to the master subsystem. Through the impedance filter block, the desired trajectory of the master system is derived to attain the desired impedance performance and provide good force feedback performance for the operator. The fast nonsingular terminal sliding mode scheme is designed separately for the master system to drive the master position to track the generated reference trajectory as fast and accurately as possible. The master output position $\theta_m$ is then sent back to the slave system and becomes the reference for the slave-side position tracking control. The robust control scheme is designed for the slave system to achieve great tracking performance in the presence of uncertainties and nonlinearities. Subsequently, the global stability of the overall system and good transparency performance including position tracking and force feedback is simultaneously achieved.

### 7.2.1 Control Contact Force Estimation Using Adaptive Observer

In this section, a novel AFOB approach is designed to estimate the force information for the system without the adoption of a force sensor. The force information is employed for a force reflecting the control scheme in the next section. Firstly, the following auxiliary variables are

defined:

$$x_{1i} = \theta_i, x_{2i} = \dot{\theta}_i, \tag{143}$$

As found in [40], the nominal system of (6) and (7) is represented by the following form

$$\dot{x}_{2i} = \Lambda_i - \bar{M}_i^{-1}\bar{\Delta}_i + \sigma_i \tau_{id} \tag{144}$$

where $\sigma_i = -\bar{M}_i^{-1}, \Lambda_i = \bar{M}_i^{-1}(\tau_i - \bar{C}_i x_{2i} - \bar{K}_i x_1)$ with $\bar{M}_i$, $\bar{C}_i$, $\bar{K}_i$ are the nominal values of the inertia term $M_i$, damping term $C_i$, stiffness term $K_i$, respectively; $\bar{\Delta}_i$ is the total of unknown disturbance and modeling errors;

**Assumption 7.1:** *The norm of* $\bar{\Delta}_i$ *is bounded by the following inequation.*

$$\left\|\bar{\Delta}_i\right\| \le \bar{\omega}_i, \tag{145}$$

*where* $\bar{\omega}_i$ *is a positive constant.*

Let the filtered variable $\sigma_i^*, \Lambda_i^*$ and $x_{2i}^*$ as

$$\begin{cases} m\dot{\sigma}_i^* + \sigma_i^* = \sigma_i, & \sigma_i^*(0) = 0 \\ m\dot{\Lambda}_i^* + \Lambda_i^* = \Lambda_i, & \Lambda_i^*(0) = 0 \\ m\dot{x}_{2i}^* + x_{2i}^* = x_{2i}, & x_{2i}^*(0) = 0 \end{cases} \tag{146}$$

where $m$ is a positive value. Ideally, an invariant manifold is then raised to design an unknown input observer.

The following auxiliary variables are defined.

$$\vartheta = \frac{(x_{2i} - x_{2i}^*)}{m} - \Lambda_i^* - \sigma_i^* \tau_{id} \tag{147}$$

From (146) and (147), the time derivative of $\vartheta$ is obtained as

$$\begin{aligned} \dot{\vartheta} &= -\frac{1}{m}\left(\frac{x_{2i} - x_{2i}^*}{m} - \Lambda_i^* - \sigma_i^* \tau_{id}\right) - \frac{\bar{M}_i^{-1}\bar{\Delta}_i}{m} - \sigma_i^* \dot{\tau}_{id} \\ &= -\frac{1}{m}\left(\vartheta + \bar{M}_i^{-1}\bar{\Delta}_i + m\sigma_i^* \dot{\tau}_{id}\right). \end{aligned} \tag{148}$$

**Lemma 7.1:** *Consider the system* (144) *with the filter* (146)*, the variable* $\vartheta$ *is ultimately bounded for any finite a positive value of m and decreases in an exponential sense. Additionally, the manifold* $\lim_{a\to 0}(\lim_{t\to\infty}[\vartheta]) = 0$ *is invariant for* $m \to 0$.

**Proof:** *The proof of the Lemma* 7.1 *is shown in Appendix* 7.1.

According to the swapping lemma in [144] and applying a filter 1*/(ms* + 1*)* on both sides of (146) for any finite $m > 0$, it obtains:

$$\frac{1}{m}(x_{2i}-x_{2i}^{*})=\Lambda_i^{*}+\sigma_i^{*}\tau_{id}+\frac{m}{ms+1}\sigma_i^{*}\dot{\tau}_{id}+\frac{1}{ms+1}\bar{M}_i^{-1}\bar{\Delta}_i \tag{149}$$

where the last two terms $\psi = [m/(ms + 1)][\sigma_i^{*}\dot{\tau}_{id}] + [1/(ms + 1)][\bar{M}_i^{-1}\bar{\Delta}_i]$ from the filtering external torques of $[\sigma_i^{*}\dot{\tau}_{id}]$ and the uncertainties $\bar{M}_i^{-1}\bar{\Delta}_i$. If $\tau_{id}$ is constant and $\bar{\Delta}_i = 0$, then $\psi = 0$. Since $\sigma_i$ is bounded, its filtered function $\sigma_i^{*}$ is also bounded, i.e., $\|\sigma_i^{*}\| \le \mu_\sigma$ for a constant $\mu_\sigma$. As the external torques $\tau_{id}$ and its derivative is bounded, $\psi$ is bounded for any finite a positive value of $m$, i.e., $\|\psi\| \le \bar{\psi}$. In this case, $\psi$ can be regarded as disturbances unsettling the ideal manifold $\Phi = 0$ in Lemma 7.1.

Considering the approach as in [145, 146], the variables of the proposed adaptive law are defined as

$$\begin{cases}\Gamma_1 = \Upsilon_1\hat{\tau}_{id} - \Upsilon_2 \\ \Gamma_2 = \sigma_i^{*T}\sigma_i^{*}\hat{\tau}_{id} - \sigma_i^{*T}((x_{2i}-x_{2i}^{*})/m - \Lambda_i^{*})\end{cases} \tag{150}$$

where $\hat{\tau}_{id}$ is the estimate of $\tau_{id}$, $\dot{\Upsilon}_1 = -a\Upsilon_1 + \sigma_i^{*T}\sigma_i^{*}$, and $\dot{\Upsilon}_2 = -a\Upsilon_2 + \sigma_i^{*T}((x_{2i}-x_{2i}^{*})/m - \Lambda_i^{*})$ when $\Upsilon_1(0) = 0$and $\Upsilon_2(0) = 0$, respectively, with $a$ is a positive constant scalar.

**Lemma 7.2***: The variables in* (150) *are equivalent to*

$$\begin{cases}\Gamma_1 = -\Upsilon_1\tilde{\tau}_{id} + \Omega \\ \Gamma_2 = -\sigma_i^{*T}\sigma_i^{*}\tilde{\tau}_{id} + \sigma_i^{*}\psi\end{cases} \tag{151}$$

*where* $\Omega = \int_0^t e^{-a(t-\tau)}\sigma_i^{*T}(\tau)(\sigma_i^{*}(\tau)(\tau_{id}(t)-\tau_{id}(\tau)) + \psi(\tau))d\tau$ *is a bounded residual error satisfying* $\|\Omega\| \le (2\mu_\sigma^2\varepsilon_{\tau_i} + \mu_\sigma\bar{\psi})/a$, *with* $\tilde{\tau}_{id} = \tau_{id} - \hat{\tau}_{id}$ *are the estimation errors and* $\|\tau_{id}\| \le \varepsilon_{\tau_i}$.

**Proof**: *The proof of the Lemma* 7.2 *is shown in Appendix* 7.2.

An adaptive gain $\kappa$ is calculated as

$$\dot{\kappa} = a\kappa - \kappa\sigma_i^{*T}\sigma_i\kappa \tag{152}$$

Then, taking the integral (152), which can be obtained as follows

$$\kappa^{-1} = e^{-at}\kappa_0 + \int_0^t e^{-a(t-\tau)}\sigma_i^{*T}(\tau)\sigma_i^{*}(\tau)d\tau = e^{-at}\kappa_0 + \Upsilon_1 \tag{153}$$

where the fact that $(d/dt)\kappa\kappa^{-1} = \dot{\kappa}\kappa^{-1} + \kappa(d/dt)\kappa^{-1} = 0$.

From (153) discloses that $\kappa$ converges to the inverse of $\Upsilon_1$. In [147], the definition of the persistently exciting, i.e., $\int_t^{t+T}\sigma^T(\tau)\sigma(\tau)d\tau \ge \beta$ for any finite $t$, $T$, $\beta$ are positive values. Since $\int_0^t e^{-a(t-\tau)}\sigma^T(\tau)\sigma(\tau)d(\tau) > \int_{t-T}^t e^{-aT}\sigma^T(\tau)\sigma(\tau)d(\tau) \ge \beta e^{-aT}$ holds for $t > T$. Hence, $\lambda_{\min}(\Upsilon_1) > \beta e^{-aT} > 0$ holds that $\Upsilon_1 > \beta e^{-aT} > 0$. Thus,

$$\kappa^{-1}(t) \le \kappa^{-1}(0) + \mu_\sigma^2 \int_0^t e^{-a(t-\tau)} d\tau \le \kappa_0 + \mu_\sigma^2 / a. \tag{154}$$

From (154) the boundedness of $\kappa$ can be derived as

$$\kappa^{-1}(t) = e^{-at}\kappa(0) + \Upsilon_1(t) \ge e^{-aT}\beta. \tag{155}$$

Combination (154) and (155) show that

$$\left(\lambda_{\min}(\kappa_0) + \mu_\sigma^2 / a\right)^{-1} \le \kappa(t) \le e^{aT}\beta^{-1}. \tag{156}$$

As a consequence, the adaptation law is expressed to estimate external torques as the following.

$$\dot{\hat{\tau}}_{id} = -\delta\kappa\left(\Gamma_1 + \eta\Gamma_2\right) \tag{157}$$

where $\delta$, $\eta$ is a positive scalar, and $\kappa$ is the online updated value in (154).

**Theorem 7.1***: The boundedness of the external force estimation error* $\|\tilde{\tau}_{id}\|$ *is guaranteed the convergence to an expression defined by* $\|\tilde{\tau}_{id}\| = \|\tau_{id} - \hat{\tau}_{id}\| \le \bar{\zeta}_i$, *where* $\bar{\zeta}_i$ *is a positive design parameter when σ is persistently exciting.*

**Proof**: *The proof of the Theorem* 7.1 *is shown in Appendix* 7.3.

### 7.2.2 Master control design

By measuring the active torque estimate applied by the operator, it is possible to compute the new reference trajectory required to make the master robot operate in certain mass, stiffness and damping parameters. As a result, the adapted angle $\theta_{mf}$ can be obtained with an impedance filter as follow:

$$\theta_{mf} = \frac{\hat{\tau}_{md} - \hat{\tau}_{sd}}{M_d s^2 + C_d s + K_d} + \theta_d \tag{158}$$

where $M_d$, $C_d$, $K_d$ are the designed impendence parameters and $\theta_d$ is the initial desired command of the master subsystem.

In order hand to achieve good tracking performance and fast response of systems, a fast finite time nonsingular terminal sliding mode control is proposed for the master system in the presence. The tracking errors are defined as the following

$$\tilde{\theta}_m = \theta_{mf} - \theta_m, \dot{\tilde{\theta}}_m = \dot{\theta}_{mf} - \dot{\theta}_m \tag{159}$$

To obtain the terminal convergence of the tracking errors, a special variable called terminal sliding surface is designed as

$$s_m = \lambda_m \tilde{\theta}_m^{[\alpha_m]} + \dot{\tilde{\theta}}_m \tag{160}$$

where $\alpha_m = p_m/q_m$, $p_m$ and $q_m$ are positive odd integers satisfying $q_m > p_m$; $\lambda_m$ is a positive parameter of the sliding surface.

From the system (19) and sliding surface formula (160), the derivative of the sliding surface with respect to time can be obtained as follows:

$$\begin{aligned}\bar{M}_m\dot{s}_m &= -\bar{M}_m\ddot{\theta}_{mf} + \bar{M}_m\lambda_m\alpha_m\tilde{\theta}_m^{[\alpha_m-1]}\dot{\tilde{\theta}}_m + \tau_m - \tau_{md} - \bar{C}_m\dot{\theta}_m - \bar{K}_m\theta_m \\ &= -\bar{M}_m\ddot{\theta}_{mr} - \bar{C}_m\dot{\theta}_{mr} - \bar{K}_m\theta_m + \tau_m - \tau_{md} - \bar{C}_m s_m\end{aligned} \tag{161}$$

where $\dot{\theta}_{mr} = s_m - \dot{\theta}_m = \dot{\theta}_{mf} + \lambda_m\tilde{\theta}_m^{[\alpha_m]}$. To preserve a fast finite-time convergence property, the reaching phase is chosen as follows:

$$s_m + \rho_{1m}s_m + \rho_{2m}s_m^{[\nu_m]}sign(s_m) = 0 \tag{162}$$

where $\rho_{1m}$, $\rho_{2m}$ are the positive constants for the reaching phase and $0 < \nu_m < 1$.

By applying the haptic control based on force sensorless is embedded into the control system to simultaneously compensate for the effects caused by dynamic uncertainties. The control signal in the master side is introduced as follows:

$$\tau_m = \bar{M}_m\ddot{\theta}_{mr} + \bar{C}_m\dot{\theta}_m + \bar{K}_m\theta_m - \varepsilon_m sign(s_m) - \rho_{1m}s_m - \rho_{2m}s_m^{[\nu_m]} + \hat{\tau}_{md} \tag{163}$$

where $\varepsilon_m$ is the bound value of the unexpected disturbances.

In the following, the sufficient condition for the stability of the master system is provided.

**Theorem 7.2**: *For the master subsystem is presented in* (19)*, with the bounded external force estimation in Theorem* 7.1 *and suppose that Assumption* 7.1 *is satisfied, i.e.* $\varepsilon_m \geq \bar{\zeta}_m + \bar{\omega}_m$*, if the sliding surface is designed as* (160) *and the control law is designed as* (163)*, then the tracking error will converge to zero in a finite time.*

**Proof:** *The proof of the Theorem* 7.2 *is shown in Appendix* 7.4.

### 7.2.3 Slave control design

A reference trajectory is designed in the slave with the input of the master position signal $\theta_m$, to produce the command trajectory for the tracking of the slave system.

The tracking errors are defined as the following

$$\theta_s = \theta_s - \theta_{sd}, \dot{\theta}_s = \dot{\theta}_s - \dot{\theta}_{sd} \tag{164}$$

where $\theta_{sd}(t)$ is the home position of the slave system. Then the sliding surfaces are designed as

$$s_s = \lambda_s\tilde{\theta}_s^{[\alpha_s]} + \dot{\tilde{\theta}}_s \tag{165}$$

where $\alpha_s = p_s/q_s$, $p_s$ and $q_s$ are positive odd integers satisfying $q_s > p_s$; $\lambda_s$ is a positive parameter of the sliding surface.

Thus, the combination of the derivative of the sliding surface (165) with respect to time and the slave dynamic (20) can be obtained as follows:

$$\begin{aligned}\bar{M}_s\dot{s}_s &= -\bar{M}_s\ddot{\tilde{\theta}}_{sd} + \bar{M}_s\lambda_s\alpha_s\tilde{\theta}_s^{[\alpha_s-1]}\dot{\tilde{\theta}}_s + \tau_s - \tau_{sd} - \bar{C}_s\dot{\theta}_s - \bar{K}_s\theta_s \\ &= -\bar{M}_s\ddot{\tilde{\theta}}_{sr} - \bar{C}_s\dot{\tilde{\theta}}_{sr} - \bar{K}_s\theta_s + \tau_s - \tau_{sd} - \bar{C}_s s_s\end{aligned} \tag{166}$$

where $\dot{\theta}_{sr} = s_s - \dot{\theta}_s = \dot{\theta}_{sd} + \lambda_s\tilde{\theta}_s^{[\alpha_s]}$. Furthermore, in order to improve the convergence toward equilibrium zero, the reaching phase is chosen as follows:

$$s_s + \rho_{1s}s_s + \rho_{2s}s_s^{[\nu_s]}sign(s_s) = 0 \tag{167}$$

where $\rho_{1s}$, $\rho_{2s}$ are the positive constants for the reaching phase and $0 < \nu_s < 1$. Thus, the slave controller can be designed as follows:

$$\tau_s = \bar{M}_s\ddot{\tilde{\theta}}_{sr} + \bar{C}_s\dot{\theta}_s + \bar{K}_s\theta_s - \varepsilon_s sign(s_s) - \rho_{1s}s_s - \rho_{2s}s_s^{[\nu_s]} + \hat{\tau}_{sd} \tag{168}$$

where $\varepsilon_s$ is the bound value of the unexpected disturbances.

**Theorem 7.3:** *For the slave system presented in* (20) *the input of the master position signal* $\theta_m$ *with the bounded external force estimation in Theorem* 7.1 *and suppose that Assumption* 7.1 *is satisfied, i.e.* $\varepsilon_s \geq \bar{\zeta}_s + \bar{\omega}_s$, *if the sliding surface is designed and the control law is designed as* (168), *then the tracking error will converge to zero in a finite time.*

**Proof:** *The proof of the Theorem* 7.3 *is shown in Appendix* 7.5.

Furthermore, the $i^{th}$ element (for $i = m,s$) of the surface $s_i$ in (160) and (165) can be given as follows:

$$s_i = \lambda_i\tilde{\theta}_i^{[\alpha_i]} + \dot{\tilde{\theta}}_i \tag{169}$$

When the terminal sliding surface (169) is reached ($s_i = 0$), its derivative with respect to time is obtained as

$$\begin{aligned}\dot{s}_i &= \lambda_i\alpha_i\tilde{\theta}_i^{[\alpha_i-1]}\dot{\tilde{\theta}}_i + \ddot{\tilde{\theta}}_i \\ &= -\lambda_i^2\alpha_i\tilde{\theta}_i^{[2\alpha_i-1]} + \ddot{\tilde{\theta}}_i\end{aligned} \tag{170}$$

It can be seen that, if $\alpha_i > 1/2$, then the singularity problem on the terminal sliding mode does not occur. Besides, in the case $\dot{\tilde{\theta}}_i \neq 0$ while $\tilde{\theta}_i = 0$ before the reaching phase $s_i \neq 0$, the modified terminal sliding surface is to deal with the singularity problem as the following [148]:

$$s_i = \Pi_i\left(\tilde{\theta}_i\right) + \dot{\tilde{\theta}}_i \tag{171}$$

where $\Pi_i(\tilde{\theta}_i) = \begin{cases} \lambda_i\tilde{\theta}_i^{[\alpha_i]}, & \text{if } s_i = 0 \text{ or } s_i \neq 0 \text{ and } \left|\tilde{\theta}_i\right| > \varsigma_i \\ z_{1i}\tilde{\theta}_i + z_{2i}\tilde{\theta}_i^2 sign(\tilde{\theta}_i), & \text{if } s_i \neq 0 \text{ and } \left|\tilde{\theta}_i\right| \leq \varsigma_i \end{cases}$

with $z_{1i} = (2 - \alpha_i)\varsigma_i^{[\alpha_i - 1]}$, $z_{2i} = (\alpha_i - 1)\varsigma_i^{[\alpha_i - 2]}$, $\varsigma_i$ is a positive constant.

**Remark 7.1**: *The range of the parameter* $\alpha_i$ *is defined as* $1/2 < \alpha_i < 1$ *to avoid the singularity problem.*

**Remark 7.2:** *According to the finite-time stability from* [148], *the parameters* $z_{1i}$, $z_{2i}$ *are chosen to make the function* $\Pi_i(\tilde{\theta}_i)$ *and its time derivative continuous.*

### 7.3 Experimental results and discussion

This section presents the experimental results of the position tracking control and force reflecting control with AFOB on the bilateral teleoperation system, which is separated into two aspects. In the first aspect, the accuracy and effectivity of the proposed AFOB scheme for obtaining the external force of the APAM system are compared with multiple state-of-the-art force observers. In the second aspect, to illustrate the effectiveness of the proposed control scheme in a good transparency performance of both force feedback and position tracking, two typical working sub-scenarios as following:

1) *Free space*: In this working condition, the master and slave robots freely move without the external torques from the human and environment. This test is to verify the effectiveness of the position tracking control scheme. A chirp signal with different amplitudes is chosen as a reference trajectory for the master system to verify the tracking ability of the slave robot. The control algorithm in the master system much drives the master robot to follow the desired trajectory. Moreover, the response of the master side becomes the reference signal of the slave side and the slave controller is developed to make the slave manipulator track the master robot's trajectory. Thus, the effectiveness of the bilateral control scheme is demonstrated by the tracking accuracy of the slave robot position following the desired trajectory given on the master side.

2) *Contact and recovery*: In this working condition, human torque is applied to drive the master robot. Meanwhile, the slave robot will follow the generated trajectory in the master side and contact with the environment. This test is employed to show the transparency performance of the designed teleoperation system. In detail, this experiment process is continuously conducted with free-motion stage and contact motion stage, in an interaction with a "soft" environment (low stiffness of the spring is 500 $N.mm^{-1}$ and the damping coefficient of the damper is 4 $N.s.mm^{-1}$), and then in an interaction with a "stiff" environment (high stiffness of the spring is 2800 N/mm and damping coefficient of the damper is 20 $N.s.mm^{-1}$). The

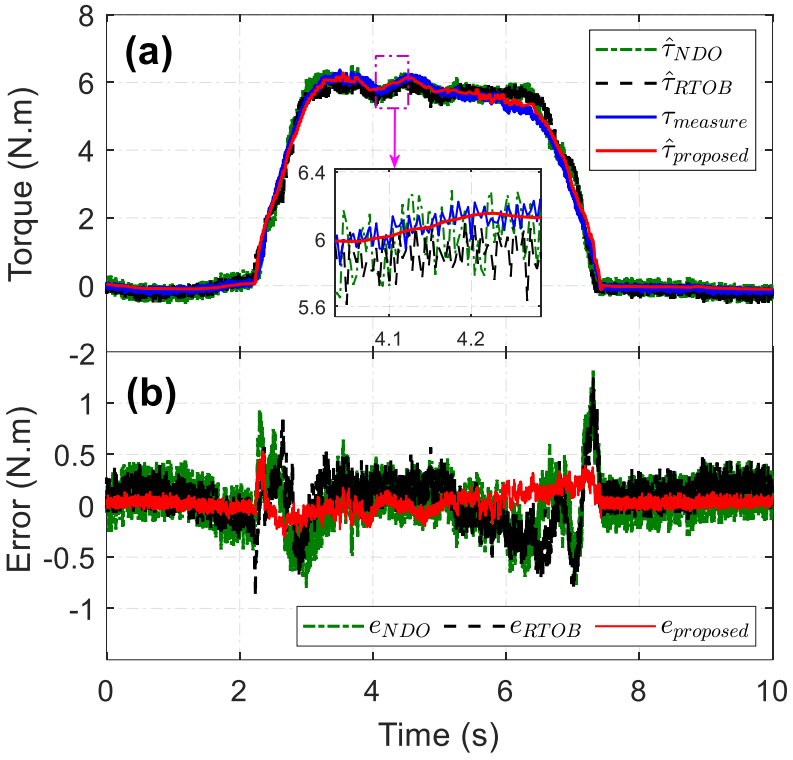


*Figure 37. Comparison of torque estimation performances in the interaction condition.*

disturbance and modeling error are set as $\varepsilon_s$ = $\varepsilon_m$ = 0.05. The impendence parameters are selected as $M_d$ = 1.5 kg, $B_d$ = 5.25 N.s.mm$^{-1}$, $K_d$ = 17.25 N.mm$^{-1}$.

### 7.3.1 Force Estimation

Three force observers are implemented to obtain the external force from the environment and from the human operator, which are the NDO used in [56], the reaction torque observer (RTOB) with Kalman filter used in [59], and the proposed AFOB. In the NDO design, the force observer gain for the master and the slave system are chosen as $L_h$ = $L_e$ = 10. In the RTOB design, the cut-off frequency of the force observer is designed as $\beta$ = 350 rad/s. Meanwhile, the parameter configurations of the proposed AFOB are designed as follows $\kappa_i(0)$ = 0.1, $\lambda_i$ = 10, $\eta_i$ = 0, $m$ = 0.1, $a$ = 10. The torque estimation performances of the three comparative observers in the interaction condition are depicted in Figure 37. As shown in Figure 37 (a), all three observers can fairly obtain the force information with acceptable estimation errors. As described in Figure 37 (b), however, root-mean-square-errors (RMSEs) associated with NDO, RTOB and proposed algorithm scheme are calculated of 0.211, 0.192 and 0.076, respectively. These results show that the performance of the proposed AFOB is much improved with the smallest steady-state estimation errors and effective noise suppression. With appropriate low-pass filters, the proposed approach shows the robustness with one tuning parameter that needs

to be selected but can also achieve high performance. Therefore, this force estimation information can be employed in the force feedback control scheme.

### 7.3.2 Tracking control performance

Following the above remarks, assumptions and on the system characteristics in the related study [22], the parameters of the proposed FNTSMC for the master and slave systems are selected as $\lambda_m = \lambda_s = 8$, $p_m = p_s = 5$, $q_m = q_s = 7$, $\varsigma_m = \varsigma_s = 10^{-4}$, $v_m = v_s = 9/11$, $\varepsilon_m = \varepsilon_s = 0.1$, $\rho_{1m} = \rho_{1s} = 10$, $\rho_{2m} = \rho_{2s} = 2$. Hence, the parameters of the PID controller were initialized by using the Zigler-Nichol method, which were selected as $K_P = 3.8$, $K_I = 25$ and $K_D = 0.15$. Based on these parameters, it is considered the basic control gains to provide a suitable control input to compel the system trajectory to its reference as closely as possible. Then, taking advantage of the TSMC and the proposed controller can adjust more specific parameters, which is given the above mention. To more express fair evaluation, the same working conditions have been applied simultaneously. Consequently, the experimental results obtained by applying, in turn, the PID, TSMC, and proposed controller to the testing system are shown in Figure 38, as well as zoom-in in the graph. From Figure 39 to Figure 42 show the experimental results of the proposed method where the position and force responses at both master and slave sides under various conditions of the environment.

In the free space situation, the desired chirp signal of the frequency of 0.36 Hz with the reducing amplitude by the function $5\pi \times (1 - 0.18t)$ via sampling time $t$ is supplied to the initial command of the master system as seen in Figure 38. The output tracking performances of the master and slave are shown in Figure 38 (a) and (b), as well as zoom-in performance, respectively, whereas Figure 38 (c) and (d) express the output tracking errors between the master/slave and desired/slave, respectively. For each situation, both master and slave robots are controlled bilaterally with the same pair of the PID, TSMC, or proposed controller, respectively. As shown in Figure 38 (c), the performances of a pair of proposed position control schemes developed by the PID framework make acceptable responses of tracking error of ± 1.1 deg. Meanwhile, the TSMC and the proposed controller algorithm improves the control performances with much smaller tracking errors. The tracking errors are mostly limited to an acceptable range of ± 0.6 deg, ± 0.4 deg, respectively. As results in Figure 38 (d), it is easily seen that the PID and TSMC performances of the slave robot were significantly degraded with the bound of the tracking error early two times that of the performance comparative case of the master/slave robot, from ± 1.1 deg to ± 2.2 deg, from ± 0.6 deg to ± 1.3 deg, respectively, whilst the bound of the tracking errors of the proposed controller algorithm is less than 0.8 deg. On

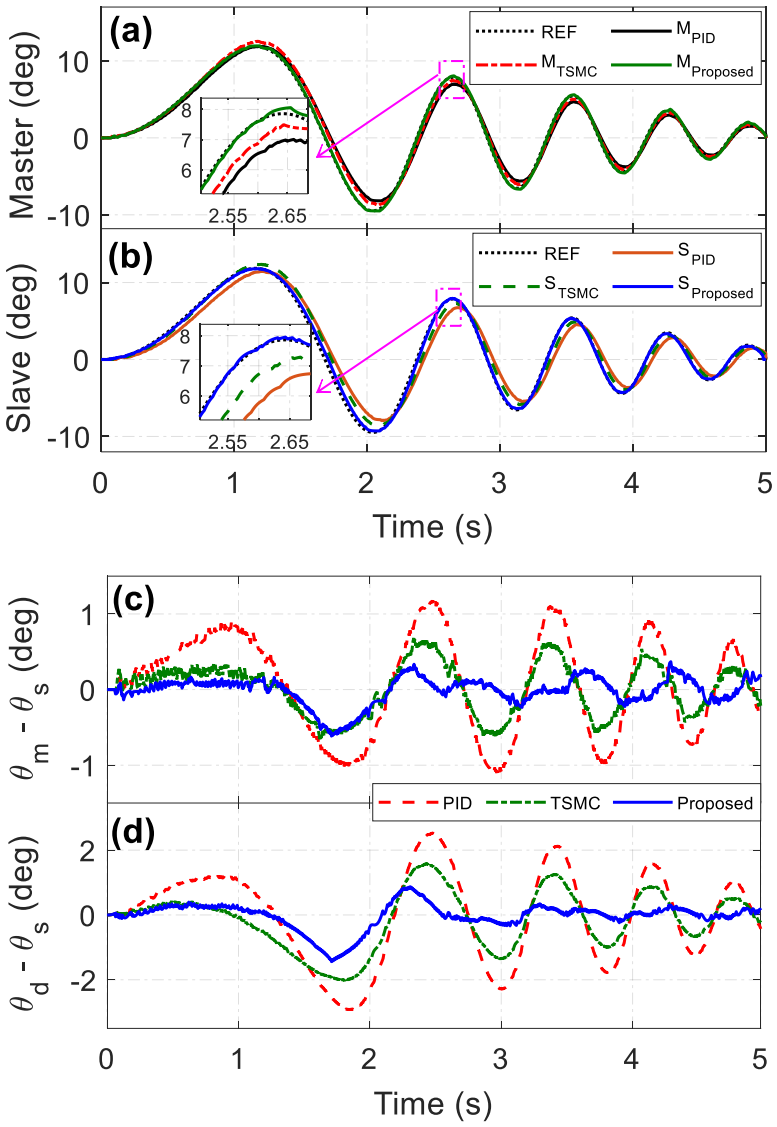


*Figure 38. Comparison of the tracking position performances in the free space situation.*

*Table 5. Performance indices of comparative controllers.*

| Controller | | PID | TSMC | Proposed |
|---|---|---|---|---|
| $\theta_m - \theta_s$ | $L_2[e]$ | 0.6496 | 0.3341 | 0.1823 |
| ($^O$) | $e_{max}$ | 1.1178 | 0.6811 | 0.3686 |
| $\theta_d - \theta_s$ | $L_2[e]$ | 1.4042 | 0.7053 | 0.4036 |
| ($^O$) | $e_{max}$ | 2.2428 | 1.5975 | 0.8394 |

the whole, the proposed control method always maintains the great tracking performance between the desired command and slave robot within a small range due to its robustness against nonlinearities or uncertainties. In order to have a quantitative comparison between the effectiveness of the control strategies, the tracking errors in Table 5 are calculated by the usage

of the integral absolute error $(L_2[\mathrm{e}] = \sqrt{(\int_0^T |e|^2\, dt)/T})$, where $T$ is the total experimental time. As shown in this table, the proposed control method is once again confirmed with the smallest tracking errors.

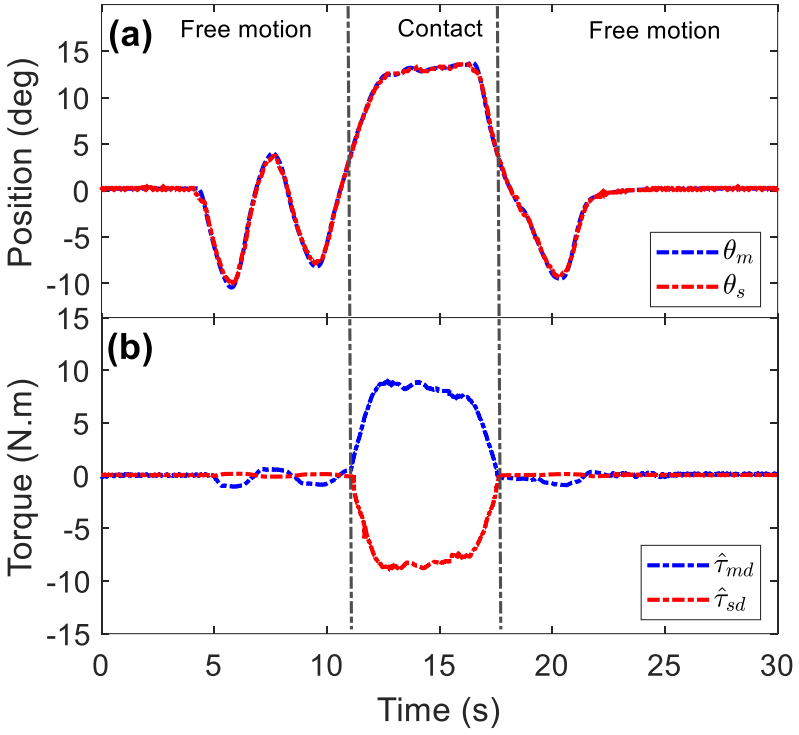


*Figure 39. Transparency performance of the BHTS in the free motion and soft contract.*

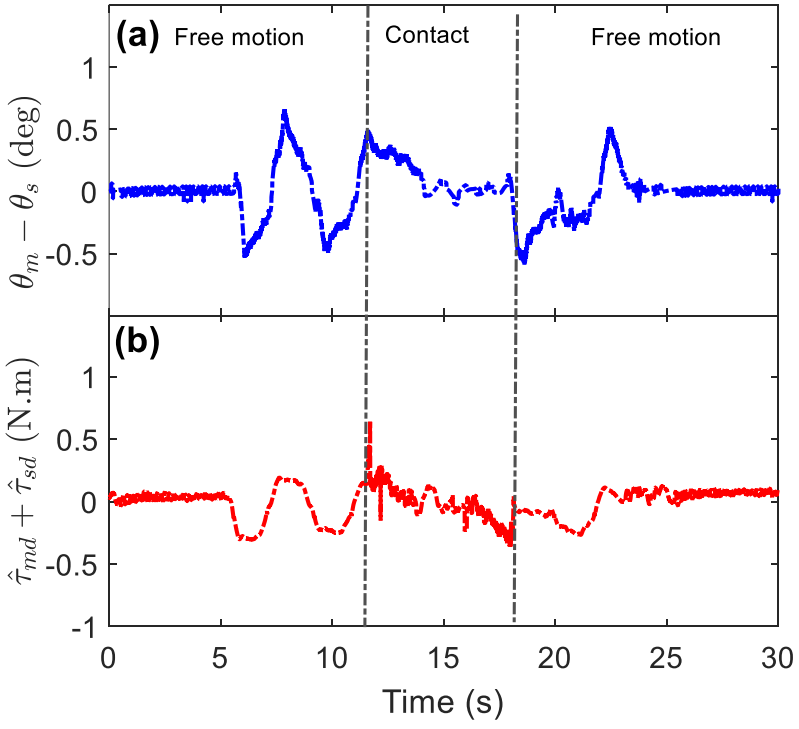


*Figure 40. Transparency errors of the BHTS in the free motion and soft contract.*

### 7.3.3 Transparency performance

In the contact and recovery situation, the initial desired command of the master subsystem is set to a home position, i.e. $\theta_d$ = 0. To start with, the environment model is adjusted in low stiffness and damping by the adjusting mechanism. Then the slave manipulator is in a collision

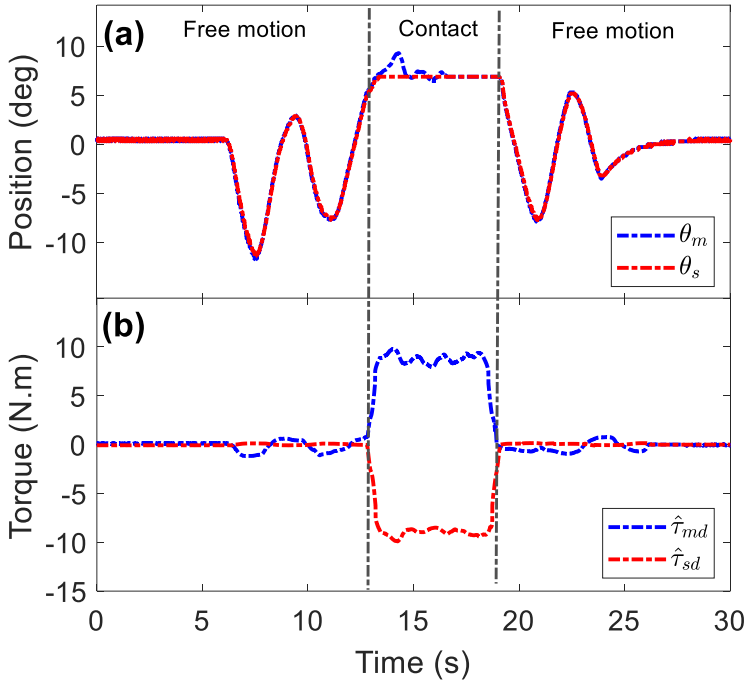


*Figure 41. Transparency performance of the BHTS in the free motion and stiff contract.*

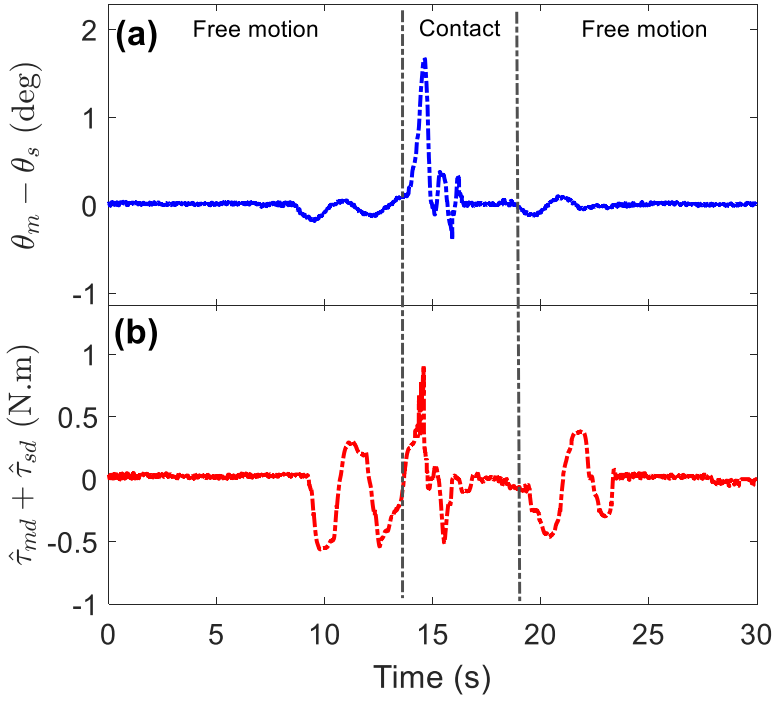


*Figure 42. Transparency errors of the BHTS in the free motion and stiff contract.*

with the "soft" environment when $t$ = 12 s, and the contact is released when $t$ = 18 s as seen in Figure 39. According to Figure 39 (a) and Figure 40 (b), the excellent tracking performance of the slave manipulator following the trajectory from the master manipulator is effectively achieved. As seen in Figure 39 (b) and Figure 40 (b), the force transmission in the state of contact is very small in a steady state.

Successively, the environment model is transformed into the "stiff" environment with high stiffness and damping as presented in Figure 41 and Figure 42. Then the interactions with the environment occur when $t \in$ [13 s, 19 s]. From these results, there is the overshoot of the master position at the beginning when the interaction of the slave with the environment occurs. However, this overshoot is controllable and the position tracking is also recovered rapidly. It is shown that the tracking performance of the bilateral teleoperation system is still guaranteed despite changing working conditions. Based on the results in Figure 41 (a) and Figure 42 (a), the performance of position tracking between the master and the slave is also satisfactory. According to the subfigures *b* in Figure 41 and Figure 42, when the system has occurred contact, the error between $\hat{\tau}_{md}$ and $-\hat{\tau}_{sd}$ is also realized.

In short, this also can prove the excellent tracking performances of both master and slave position tracking control scheme in the presence of nonlinearities and uncertainties in the APAM systems. Furthermore, the force reproduces at the master side sensed is in the opposite direction with respect to the force sensed at the slave side, and their sum is small in a steady state. Therefore, the great transparency performance and global stability of the bilateral haptic teleoperation under the proposed control scheme are achieved despite the uncertainties and in different working conditions.

## 7.4 Chapter summary

This chapter proposed a novel force reflecting control approach based on a new adaptive force observer scheme and robust bilateral control for the designed APAM based haptic system under uncertainties. The AFOB approach is designed to obtain the interaction force with an environment for the force reflecting control design with the elimination of the uncertainties and also the noise effect in the obtained force sensing. Then, a robust bilateral control scheme is developed with the combination of the separately fast finite time nonsingular terminal sliding mode control schemes with the force estimation in both subsystems.

Comparative experimental results show that the proposed force observer can obtain accurate force information with noise elimination. This force information is employed in the force

reflecting control scheme to improve transparency performance. Finally, the experimental results of the proposed bilateral control in different working conditions show that the provided stability of the overall system and the transparency performance can be attained simultaneously. In the future, the teleoperation test bench with a higher degree of freedom manipulator to extend the application of the teleoperation system

# Chapter 8

# CONCLUSION AND FUTURE WORKS

## 8.1 Conclusion

This thesis presents series controllers for the BHTS driven by APAM configuration to solve problems in order to realize the human-friendly therapy robot in the near future. First of all, a typical test-rig of the PAM actuator and proper materials is selected and simplified setup to verify each characteristic, then the BHTS is fabricated full set including master and slave subsystem. The system model is next derived based on the results in literature and experiments. To start with, the existence or the uncertain, nonlinear, and unknown terms in the system dynamics is core problems, which restrict guaranteeing operation performance. Thus, these problems need more attention in constructing an accurate position controller.

To develop an effective position tracking controller and overcome the difficulties of the system modeling, the AITSMC with TDE approach is proposed. The controller is built as taking advantage of both backstepping TSMC and integral sliding surface combinations under the sliding mode technique. Its uncertainties and disturbance are handled by adaptation gain and TDE. The effectiveness of the AITSMC controller was then verified in the setup system in comparison with a conventional PID controller under various working conditions.

Moreover, the interacted force properties with the environment are considered. In detail, a new force sensorless finite-time control scheme is investigated based on the new adaptive gain fast ITSMC combined with a friction-free disturbance (FSOB). As the experimental results, it can be easily seen that applicability for a system and not only simplicity in the design but also the significant effectiveness of force tracking problems. The stability and finite-time convergence characteristic of the controlled system are analyzed by the Lyapunov theory.

After investigating the position and force features of the PAM system by several proposed strategies, one of the difficult problems is needed to solve, when the detailed interacted human or environmental parameters are unknown. For robot-environment interaction control in the slave subsystem, the model-free controllers for optimal contact force are based on leaning online ability to guarantee position and force tracking. It is modified the classical robot interaction control to avoid the transformation from joint space to task space using the proposed *Q*-learning based RL approximation method. Experiment results are shown that the proposed approach is not only feasible but also assuring global stability.

Successively, in the master subsystem, human behavior may lead to difficulty in processing the outer-task. To address this drawback, the internal parameters of a prescribed impedance model of the system dynamics can be optimal by using the IRL approach based on the output-feedback algorithm. It is given little information on the human arm model while RNN is provided highly effective controllers in yielding guaranteed position control. Human-robot interaction force during the robot performing manipulation is presented as a novel barrier-Lyapunov-function. As a result, extensive experiments were done to definitely confirm the effectiveness of the proposed control in the human-robot cooperative task.

Finally, a novel force sensorless reflecting control for a haptic-enabled device driven by a bilateral PAM system,. With the wish to develop the simple, fast and robust online estimation, the novel adaptive force observer (AFOB) is proposed to estimate external forces without using any force sensor signal. Meanwhile, the separately fast finite time nonsingular terminal sliding mode control (FNTSMC) schemes are developed based on the force estimation in both subsystems to achieve good tracking performance and fast response. Thus, the great transparency performance with both force feedback and position tracking can be achieved simultaneously by using the proposed method. The finite-time stability of the total controlled system is demonstrated by theoretical proof.

## 8.2 Future works

The effectiveness and feasibility of the proposed controllers have been confirmed in both theoretical proof and experimental validation. However, some limitations can be remarked as follows. In control design in joint-space, some proper control strategies are employed to stabilize the closed-loop system with a highly robust property. Deploying these controllers with many control parameters, which are mainly tuned by the trial-and-error method, in a real-time system is really not a trivial task for an inexpert one. Besides, the proposed control strategies in joint-space are almost based on the mathematical or experimental model. For the faster convergence rate, the method should be implemented from the exact mathematical model of the system dynamics. In the model approximation strategies in task-space, because of the existence of reward function and the process of learning, the computational complexity scales exponentially with the size of data. This is a big problem to learn control policy from a large number of data. Based on the prototype developed in this thesis, it is possible to develop a high-quality commercial teleoperation device in the rehabilitation field. These limitations will be done in the near future.

# Appendix

## Appendix 3.1

In order to prove the Theorem 3.1, a Lyapunov candidate function is considered as follows:

$$V_1 = 0.5\upsilon_1^2 + 0.5\upsilon_2^2 \tag{172}$$

The time derivative of $V_1$ is computed as:

$$\begin{aligned}\dot{V}_1 &= \upsilon_1\dot{\upsilon}_1 + \upsilon_2\dot{\upsilon}_2 \\ &= \upsilon_1\left(\upsilon_2 + \beta_1 - \dot{x}_{1d}\right) + \upsilon_2\left(f_0\left(x_1, x_2\right) + g_0\left(x_1\right)u_n - \ddot{x}_{1d} + \eta_1\dot{\upsilon}_1 + \kappa_1\gamma_1\upsilon_1^{\gamma_1 - 1}\dot{\upsilon}_1\right) \\ &= -\eta_1\upsilon_1^2 - \kappa_1\upsilon_1^{\gamma_1+1} - \eta_2\upsilon_2^2 - \kappa_2\upsilon_2^{\gamma_2+1} \le 0\end{aligned} \tag{173}$$

According to the finite time stability from [148], the variables $\upsilon_1$ and $\upsilon_2$ can converge to zeros in a finite time. From (25) and (27), the tracking errors $e_1$ and $e_2$ also reach zeros in a finite time.

The proof is completed. ■

## Appendix 3.2

Considering the following Lyapunov candidate function.

$$V_2 = 0.5\rho\left(t\right)^2 \tag{174}$$

Differentiating the above Lyapunov function, one obtains:

$$\begin{aligned}\dot{V}_2 &= \rho\left(t\right)\dot{\rho}\left(t\right) \\ &= \rho\left(t\right)\left[\dot{s}\left(t\right) - \left(k_1e_2 + \alpha k_2e_1^{\alpha-1}e_2 + f_0\left(x_1, x_2\right) + g_0\left(x_1\right)u_n - \ddot{x}_{1d}\right)\right] \\ &= \rho\left(t\right)\left(g_0\left(x_1\right)u_s + d\right) \\ &= -\eta_3\left|\rho\left(t\right)\right| - \kappa_3\rho\left(t\right)^2 - \kappa_4\rho\left(t\right)^{\gamma_3+1} + \rho\left(t\right)d \\ &\le -\kappa_3\rho\left(t\right)^2 - \kappa_4\rho\left(t\right)^{\gamma_3+1} \le 0\end{aligned} \tag{175}$$

Using the finite time criterion described in [37] and [148], the convergence of $\rho(t)$ to zero in a finite time is guaranteed. According to (22) and (35), the tracking error of the system will reach zero in a finite time despite of the presence of the lump disturbance. Thus, the system is a finite time stable.

The proof is completed. ■

## Appendix 3.3

Considering the following Lyapunov function.

$$V_3 = 0.5\rho(t)^2 + 0.5\mu\left(\hat{\eta}_3 - \vartheta\right)^2 \tag{176}$$

Taking the time derivative of the above Lyapunov function, one obtains:

$$
\begin{aligned}
\dot{V}_3 &= \rho(t)\dot{\rho}(t) + \mu\left(\hat{\eta}_3 - \vartheta\right)\dot{\hat{\eta}}_3 \\
&= \rho(t)\Big[ k_1 e_2 + \alpha k_2 e_1^{\alpha-1} e_2 + f_0\left(x_1, x_2\right) + g_0\left(x_1\right)u + d - \ddot{x}_{1d} \\
&\quad -\left( k_1 e_2 + \alpha k_2 e_1^{\alpha-1} e_2 + f_0\left(x_1, x_2\right) + g_0\left(x_1\right)u_n + \hat{d} - \ddot{x}_{1d} \right)\Big] + \mu\left(\hat{\eta}_3 - \vartheta\right)\dot{\hat{\eta}}_3 \\
&= \rho(t)\left( g_0\left(x_1\right)u_s\left(t\right) + \varepsilon_d \right) + \mu\left(\hat{\eta}_3 - \vartheta\right)\dot{\hat{\eta}}_3 \\
&\quad -\rho(t)\Big[ \hat{\eta}_3 sign\left(\rho\right) + \kappa_3\rho\left(t\right) + \kappa_4\rho\left(t\right)^{\gamma_3} \Big] + \rho(t)\varepsilon_d + \mu\left(\hat{\eta}_3 - \vartheta\right)\dot{\hat{\eta}}_3 \\
&= -\kappa_4\rho\left(t\right)^{\gamma_3+1} - \kappa_3\rho\left(t\right)^2 \le 0
\end{aligned}
\tag{177}
$$

Basing on the Lyapunov stability criterion, the stability and finite-time convergence of the tracking error are guaranteed in spite of the presence of uncertainties and disturbances.

The proof is completed. ■

**Appendix 3.4**

This appendix presents the proof of the boundedness of TDE error $\varepsilon_d$.

The total control signal (33) for the PAM system can be rewritten as follows

$$
u = \psi - g_0\left(x_1\right)^{-1}\left( f_0\left(x_1, x_2\right) + \hat{d} \right) \tag{178}
$$

where $\psi \triangleq \left(g_0\left(x_1\right)\right)^{-1}\Big[ \ddot{x}_{1d} - \upsilon_1 - f_0\left(x_1, x_2\right) - \eta_1\dot{\upsilon}_1 - \kappa_1\upsilon_1^{\gamma_1-1}\dot{\upsilon}_1 - \eta_2\upsilon_2 - \kappa_2\upsilon_2^{\gamma_2} \Big] + u_s$. Substituting the control signal in (178) into the dynamic equation (11), the closed-loop dynamics applying the proposed control method can be expressed as

$$
\varepsilon_d = \ddot{x} - \Omega \tag{179}
$$

where $\Omega = g_0(x)\psi$. Let us define $G_0(x_1) = g_0(x_1)^{-1}$ and $G(x_1) = g(x_1)^{-1}$. By substituting (179) to (10), ones obtain

$$
G(x_1)\ddot{x} = \varphi + u \tag{180}
$$

where $\varphi \triangleq G(x_1)(f(x_1, x_2) + \Delta)$. By the combination of (178), (179) and (180), the dynamics equation of the PAM system with respect to $\varepsilon_d$ is given as follows.

$$
\begin{aligned}
G(x_1)\varepsilon_d &= -G(x_1)\Omega + \varphi + u \\
&= -G(x_1)\Omega + \varphi + \psi - G_0(x_1)\left( f_0\left(x_1, x_2\right) + \hat{d} \right) \\
&= \left(G_0(x_1) - G(x_1)\right)\Omega + \varphi - G_0(x_1)\, f_0\left(x_1, x_2\right) - G_0(x_1)\hat{d}
\end{aligned}
\tag{181}
$$

From the formula of the time delay estimator (34), the equation (181) is expressed

$$
\begin{aligned}
G(x_1)\varepsilon_d = &\left(G_0(x_1) - G(x_1)\right)\Omega + \varphi - \varphi(t - t_d) - \left(G_0(x_1) - G(x_1)\right)\ddot{x}_1(t - t_d) \\
&- G_0(x_1)\left( f_0\left(x_1, x_2\right) - f_0\left(x_1(t - t_d), x_2(t - t_d)\right)\right) \\
&+ (1 - G_0(x_1)/G_0(x_1(t - t_d)))\varphi(t - t_d)
\end{aligned}
\tag{182}
$$

Substituting $\ddot{x}_1(t-t_d)=\varepsilon_d(t-t_d)+\Omega(t-t_d)$ to (182), ones obtain

$$\varepsilon_d=\left(1-\varsigma(x_1)\right)\varepsilon_d(t-t_d)+\left(1-\varsigma(x_1)\right)\Upsilon_1+\Upsilon_2 \tag{183}$$

where $\varsigma\triangleq G_0(x_1)/G(x_1)$ , $\Upsilon_1\triangleq\left(\Omega(t-t_d)-\Omega\right)$ , $\Upsilon_2\triangleq\left[\varphi-\varphi(t-t_d)\right]/G(x_1)-\varsigma\left[f_0\left(x_1,x_2\right)-f_0\left(x_1(t-t_d),x_2(t-t_d)\right)\right]+\left[1-G_0(x_1)/G_0(x_1(t-t_d))\right]\varphi(t-t_d)/G(x_1)$ . Since $\Upsilon_1$ and $\Upsilon_2$ are bounded for a sufficient small time-delay $t_d$, the first-order differential equation expressed in (183) is asymptotically bounded if the roots of $(1-\varsigma(x_1))$ lie inside a unit circle.

The proof is completed. ■

**Appendix 4.1**

Considering the Lyapunov candidate function is considered as follows:

$$V_4=\frac{1}{2}\sigma^2 \tag{184}$$

The time derivative of $V_1$ is computed as:

$$\begin{aligned}\dot{V}_4&=\sigma\dot{\sigma}\\&=\lambda_1\sigma\left[\hat{K}_c^{-1}\varepsilon-\kappa_4\sigma-\hat{\kappa}_5 sign(\sigma)^{[v]}\right]\end{aligned} \tag{185}$$

which can be divided into two forms as

$$\dot{V}_4=-\lambda_1\sigma\left[\left(\kappa_4-\frac{\varepsilon}{K_c\sigma}\right)\sigma-\hat{\kappa}_5 sign(\sigma)^{[v]}\right] \tag{186}$$

and

$$\dot{V}_4=-\lambda_1\sigma\left[\kappa_4\sigma+\left(\kappa_5-\frac{\varepsilon}{K_c sign(\sigma)^{[v]}}\right)sign(\sigma)^{[v]}\right] \tag{187}$$

As presented (186), when $|\sigma|>|\varepsilon|\left(K_c\kappa_4\right)^{-1}>\gamma\left(K_c\kappa_4\right)^{-1}\triangleq\delta_1$ the time derivative of a Lyapunov function is negative and the sliding variable will reach to the region $|\sigma|<\delta_1$. For (187), when $|\sigma|^{[v]}>|\varepsilon|\left(K_c\kappa_4\right)^{-1}>\gamma\left(K_c\kappa_4\right)^{-1}\triangleq\delta_2$, the time derivative of a Lyapunov function is negative and the sliding variable will converge to the region $|\sigma|<\delta_2$. Based on the above analysis, the time derivative of the Lyapunov function, $\dot{V}$ is negative when $|\sigma|<\delta$, where $\delta\triangleq\min(\delta_1,\delta_2)$.

The proof is completed. ■

**Appendix 4.2**

Firstly, we consider (186) with defining a positive value $\varpi\triangleq\left(\kappa_1-\frac{\varepsilon}{K_c\sigma}\right)$. This equation is represented as follows

$$\dot{V}_4 = -\lambda_1\sigma\left[\varpi\sigma - \kappa_5 sign(\sigma)^{[v]}\right] = -\chi_1\sigma^2 - \chi_2\left|\sigma\right|^{[v+1]} \tag{188}$$

with $\chi_1 = \lambda_1\varpi > 0$ and $\chi_2 = \lambda_1\kappa_5 > 0$. From **Lemma 4.2**, (188) can be rewritten as follows:

$$\begin{aligned}\dot{V}_4 &= -\chi_1\sigma^2 - \chi_2\left|\sigma\right|^{[v+1]} \\ &\le -2\chi_1 V_1 - 2^{\frac{1}{2}[v+1]} - \chi_2 V_1^{\frac{1}{2}[v+1]}\end{aligned} \tag{189}$$

From **Lemma 4.3**, the closed-loop system converges to the terminal integral sliding surface (51) infinite settling time by:

$$T \le \frac{1}{\frac{\chi_1}{2}(3-v)}\ln\left(\frac{\chi_1}{\chi_2}2^{\frac{1}{2}(1-v)}V^{\frac{1}{2}(1-v)}(0)+1\right) \tag{190}$$

when (187) is analyzed by the same above method, the finite-time convergence of the closed-loop system is guaranteed.

The proof is completed. ■

**Appendix 4.3**

The Lyapunov function is selected as follows

$$V_5 = V_4 + \frac{\eta_4}{2\eta_5}\tilde{\kappa}_5^2 \tag{191}$$

The time derivative of the Lyapunov function (191) yields as

$$\begin{aligned}\dot{V}_5 &= \dot{V}_4 + \frac{\eta_1}{\eta_2}\dot{\hat{\kappa}}_5\tilde{\kappa}_5 = -\left(\kappa_4\sigma^2 - \varepsilon\sigma - \hat{\kappa}_5 sig(\sigma)^{[v+1]}\right) \\ &\le -\kappa_4\sigma^2 + \left(\kappa_5^* - \hat{\kappa}_5\right)\left|\sigma\right|^{[v+1]} - \frac{\eta_4}{\eta_5}\dot{\hat{\kappa}}_5 \\ &= -\kappa_4\sigma^2 + \tilde{\kappa}_5\left(\left|\sigma\right|^{[v+1]} - \frac{\eta_4}{\eta_5}\dot{\hat{\kappa}}_5\right)\end{aligned} \tag{192}$$

We consider two scenarios: $\sigma \ge \varepsilon_\sigma$ and $\sigma < \varepsilon_\sigma$. In the case of $\sigma \ge \varepsilon_\sigma$, the time derivative of the Lyapunov function is rewritten as follows:

$$\dot{V}_5 \le -\kappa\sigma^2 \tag{193}$$

which means that the function $V_5(t)$ is decreasing and bounded. Additionally, the sliding variable will converge to the region, $\sigma < \varepsilon_\sigma$, with a finite time $t_\varepsilon > 0$.

After a finite time $t_\varepsilon$, the sliding variable, $\sigma(t)$, go across the region $|\sigma| < \varepsilon$, the derivative of the Lyapunov function becomes $\dot{V}_5 = -\kappa_4\sigma^2 + \left(1+\eta_4^2\right)\left|\sigma\right|^{[v+1]}$, which means the sliding variable is continuous moving in the sliding manifold until $\kappa_4 < \left(1+\eta_4^2\right)\left|\sigma\right|^{[v+1]}$ holds. After that, the

sliding variable will move out. If the sliding variable leaves the region $\sigma < \varepsilon_\sigma$, $\dot{V}_5(t)$ becomes negative again and it will drive the sliding variable back toward the sliding surface. We can conclude that the closed-loop system is globally uniformly ultimate bounded.

The proof is completed. ■

**Appendix 5.1**

Consider the TD-error (94) and the parametrization (95) the parameter vector $\phi$ of (99) is updated as

$$\begin{aligned}\dot{\phi}(t) &= r(t-\Delta t) + \frac{1}{\Delta t}(1-\gamma\Delta t)\left[\Psi^T(t+\Delta t)\phi(t) - \Psi^T\left(e_r(t), F_d(t)\right)\phi(t)\right] \\ &= F\left(\phi(t)\right)\end{aligned} \tag{194}$$

The basis function satisfies:

$$\sum_{i=1}^{K}\left|\psi_i(e_r, F_d)\right| \le 1 \tag{195}$$

The condition (195) is evident. $F(\phi(t))$ in (194) is separated as

$$F = \underbrace{\left(r(t-\Delta t) + \Delta t^{-1}\left(1-\gamma\Delta t\right)\Psi^T(t+\Delta t)\right)\Psi(t)}_{F_1} \underbrace{-\Delta t^{-1}\Psi\left(e_r(t), F_d(t)\right)\Psi^T\left(e_r(t), F_d(t)\right)\phi(t)}_{F_2} \tag{196}$$

By the contraction property, we obtain:

$$\left\|F_1(\phi_1) - F_2(\phi_2)\right\|_\infty \le \frac{1}{\Delta t}(1-\gamma\Delta t)\left\|\phi_1 - \phi_2\right\|_\infty \le \frac{1}{\Delta t}\left\|\phi_1 - \phi_2\right\|_\infty \tag{197}$$

Moreover, the $\phi$ of (194) satisfies $F(\phi^*) = 0$. For any $\rho$-norm, it holds:

$$\begin{aligned}\frac{d}{dt}\left\|\phi - \phi^*\right\|_\rho &= \left\|\phi - \phi^*\right\|_\rho^{1-\rho}\sum_{i=1}^{K}\left(\phi(i) - \phi^*(i)\right)^{\rho-1}\left(\left[F_1(\phi)_i - F_1\left(\phi^*\right)_i\right] - \left[F_2(\phi)_i - F_2\left(\phi^*\right)_i\right]\right) \\ &\le \left\|F_1(\phi)_i - F_1\left(\phi^*\right)_i\right\| - \left\|F_2(\phi)_i - F_2\left(\phi^*\right)_i\right\|\end{aligned} \tag{198}$$

By choosing $\rho = \infty$, (198) is obtained

$$\frac{d}{dt}\left\|\phi(t) - \phi^*\right\|_\infty \le -\gamma\left\|\phi(t) - \phi^*\right\|_\infty \Leftrightarrow \left\|\phi(t) - \phi^*\right\|_\infty \le e^{-\gamma t}\left\|\phi(0) - \phi^*\right\|_\infty \tag{199}$$

The solution (199) means that (194) is globally asymptotically stable

$$F_1\left(\phi^*\right) + F_2\left(\phi^*\right) = 0 \Rightarrow F_1\left(\phi^*\right) = -F_2\left(\phi^*\right) \tag{200}$$

The equilibrium point h is obtained by minimizing the $\hat{Q}$ function,

$$\phi = \bar{\Psi}(t)\left[r(t-\Delta t) + \left(1-\gamma\Delta t\right)\min_{F_d}\Psi^T\left(e_r(t), F_d(t)\right)\phi^*\right] \tag{201}$$

where $\bar{\Psi}(\bullet)=\left(\Psi\Psi^T\right)^{-1}\Psi$ is de Moore Penrose pseudoinverse.

(194) is rewritten as

$$\dot{\phi}(t)=\upsilon(t)\Omega\left(\phi(t),\Gamma(t)\right)=F\left(\phi(t)\right) \tag{202}$$

where $\Gamma(t)$ are the components of all data. Since $\Omega(t)$ is compensation of RBFs, $\Omega\left(\phi(t),\Gamma(t)\right)$ is bounded as

$$\left\|\Omega\left(\phi(t),\Gamma(t)\right)\right\|_\infty \le -\chi\left(1+\left\|\phi(t)\right\|_\infty\right) \tag{203}$$

where $\chi$ is positive; When the conditions (199) and (203) are satisfied, then there exists a positive definite function $G(\phi(t))$ with bounded second derivatives which satisfy

$$\frac{dG\left(\phi(t)\right)}{dt}=\frac{\partial G\left(\phi(t)\right)}{\partial\phi(t)}F\left(\phi(t)\right)\le 0, G\left(\phi(t)\right)=0, \phi(t)\cong\phi^* \tag{204}$$

The PE condition is satisfied. Noting that in (204) $\partial G\left(\phi(t)\right)/\partial\phi(t)>0$. According to [149], $\phi(t)$ converges to a near-optimal value $\phi^*$, and (98) converges to $\hat{Q}^*\left(e_r,F_d;\phi^*\right)$.

**Appendix 6.1**

Differentiating $e(t)$ in (106) with respect to time and equivalently gives:

$$\begin{cases}\dot{\theta}=\dot{\theta}_m-\dot{e}\\ \ddot{\theta}=\ddot{\theta}_m-\ddot{e}\end{cases} \tag{205}$$

Thus, the sliding mode tracking error (108) is rewritten and differentiated with respect to time as follows:

$$\begin{cases}\dot{e}=\sigma_h-\mu_1 e-\mu_2\xi\\ \ddot{e}=\dot{\sigma}_h-\mu_1\dot{e}-\mu_2 e\end{cases} \tag{206}$$

Using (206) in (18) yields

$$M(\ddot{\theta}_m-(\dot{\sigma}_h-\mu_1\dot{e}-\mu_2 e))+C(\dot{\theta}_m-(\sigma_h-\mu_1 e-\mu_2\xi))+Ke+\tau_d=\tau+K_h\tau_h \tag{207}$$

This gives the sliding mode error dynamics

$$M\dot{\sigma}_h=-C\sigma_h+\psi(q)+\tau_d-\tau-K_h\tau_h \tag{208}$$

with $\psi$ defined in (109) The robot dynamics (18) is assumed to be unknown and therefore $\psi$ in (208) is unknown and approximated online by (108). Then, the closed-loop filtered error dynamics (208) becomes

$$M\dot{\sigma}_h=-C\sigma_h+\hat{W}_1^T\phi(V^Tq)+\tau_d-(\tau+K_h\tau_h)+\tilde{\psi} \tag{209}$$

where $\tilde{\psi} = \psi - \hat{\psi}$ is the estimation error for approximating the function $\psi$. Substituting $\tau$ form (107) and (108) in (209) gives

$$M\dot{\sigma}_h = -C\sigma_h + \tau_d - (K_s\sigma_h - u_r(t)) + \tilde{\psi} \tag{210}$$

A candidate Lyapunov function is now selected as follow:

$$V_6 = \frac{1}{2}\sigma_h^T M\sigma_h + tr(\tilde{W}_1^T F^{-1}\tilde{W}_1) + tr(\tilde{W}_2^T G^{-1}\tilde{W}_2) \tag{211}$$

where the weight estimation errors are $\tilde{W}_1 = W_1 - \hat{W}_1, \tilde{W}_2 = W_2 - \hat{W}_2$. Taking the derivatives of (211) and doing some manipulations yields [37, 150]

$$\begin{aligned}
\dot{V}_6 &= -\sigma_h^T K_s\sigma_h + \frac{1}{2}\sigma_h^T(\dot{M} - 2C) + tr\left\{\tilde{W}_1^T\left(F^{-1}\tilde{W}_1 + \left(\hat{\phi} - \hat{\phi}'\hat{W}_2^T q\right)\sigma_h^T\right)\right\} \\
&\qquad + tr\left\{\tilde{V}^T\left(G^{-1}\tilde{W}_2 + \left(\hat{\phi} - \hat{\phi}'\hat{W}_2^T q\right)\sigma_h^T\right)\right\} + \sigma_h^T\delta_\Delta \\
&= -\sigma_h^T K_s\sigma_h + k\|\sigma_h\|\left(tr\left\{\tilde{W}_1^T(W_1 - \tilde{W}_1)\right\} + tr\left\{\tilde{W}_2^T(W_2 - \tilde{W}_2)\right\}\right) + \sigma_h^T\left(\delta_\Delta + u_r\right) \\
&\le -\sigma_h^T K_s\sigma_h + k\|\sigma_h\|.\left\|\tilde{Z}\right\|_F(Z_B - \left\|\tilde{Z}\right\|_F) - K_Z(\left\|\hat{Z}\right\|_F + Z_B)\|\sigma_h\|^2 + \|\sigma_h\|.\|\delta_\Delta\| \\
&\le K_{s_{\min}}\|\sigma_h\|^2 + k\|\sigma_h\|.\left\|\tilde{Z}\right\|_F(Z_B - \left\|\tilde{Z}\right\|_F) - K_Z(\left\|\hat{Z}\right\|_F + Z_B)\|\sigma_h\|^2 \\
&\qquad + \|\sigma_h\|.\left[C_0 + C_1\left\|\tilde{Z}\right\|_F + C_2\|\sigma_h\|.\left\|\tilde{Z}\right\|_F\right] \\
&\le -\|\sigma_h\|\left[K_{s_{\min}}\|\sigma_h\| - k\left\|\tilde{Z}\right\|_F(Z_B - \left\|\tilde{Z}\right\|_F) - C_0 - C_1\left\|\tilde{Z}\right\|_F\right] \\
&\le -\|\sigma_h\|\left[k(\left\|\tilde{Z}\right\|_F - \frac{1}{2}C_3)^2 + K_{s_{\min}}\|\sigma_h\| - C_0 - k\frac{C_3^2}{4}\right]
\end{aligned} \tag{212}$$

where $\delta_\Delta = \xi + \tau_d$; Since $tr\left\{\tilde{Z}^T(Z - \tilde{Z})\right\} =< \tilde{Z}, Z - \left\|\tilde{Z}\right\|_F^2 \le \left\|\tilde{Z}\right\|_F\|Z\|_F - \left\|\tilde{Z}\right\|_F^2$; and $K_{s_{\min}}$ is the minimum singular value of $K_s$; $C_3 = Z_B + C_1/k$ is defined with $C_0$, $C_1$, and $C_2$ are known constants [151]. The last inequality $\dot{V}_3$ is negative as long as the term in braces is positive, it means that is guaranteed positive as long as either

$$\|\sigma_h\| > \frac{C_0 - k\frac{C_3^2}{4}}{K_{s_{\min}}} \equiv B_\sigma \ or \ \left\|\tilde{Z}\right\|_F > \frac{C_3}{2} + \sqrt{\frac{C_0}{k} + \frac{C_3^2}{4}} \equiv B_Z \tag{213}$$

Thus, $V_6$ is negative outside a compact set. According to the LaSalle extension, this demonstrates the uniform ultimate boundedness of both $||\sigma_h||$ and $||Z||_F$ as long as the control remains valid within this set. However, the PD gain condition (1) shows that the compact set defined by $|| \sigma_h || \le B_\sigma$ is contained, so that the approximation property holds throughout.

This completes the proof. ■

**Appendix 6.2**

Consider the Lyapunov function

$$V_7(X) = X^T PX \tag{214}$$

In the steady-state case, $\dot{P}$ = 0, taking the derivative with respect to time along with the augmented state equation (134) and taking the derivative (214) along the trajectories of the closed-loop system is given by

$$\begin{aligned}
\dot{V}_7 &= \frac{1}{2}(\dot{X}^T PX + X^T \dot{P}X + X^T P\dot{X}) \\
&= \frac{1}{2}((A^T X^T + B^T u_e^T)PX + X^T \dot{P}X + X^T P(AX + Bu_e)) \\
&= \frac{1}{2}(A^T X^T PX + B^T u_e^T PX + X^T \dot{P}X + X^T PAX + X^T PBu_e) \\
&= \frac{1}{2} X^T (A^T P + \dot{P} + PA)X + X^T PBu_e) \\
&= -\frac{1}{2} X^T QX \le 0.
\end{aligned} \tag{215}$$

Therefore, the solution to the formulated LQR problem gives the optimal values of the prescribed impedance model parameters and the gain of the human operator force.

This completes the proof. ■

**Appendix 7.1**

For the boundedness of $\vartheta$, a candidate Lyapunov function is selected as follow:

$$V_8 = \frac{1}{2}\vartheta^T \vartheta \tag{216}$$

Then the time derivative of $V_8$ is given as

$$\begin{aligned}
\dot{V}_8 &= -\vartheta^T \frac{1}{a}\left(\vartheta + \bar{M}_i^{-1}\bar{\Delta}_i + m\sigma_i^* \dot{\tau}_{id}\right) \\
&\le -\frac{1}{m}\vartheta^T \vartheta + \frac{1}{m}\left\|\vartheta\right\|\left\|\bar{M}_i^{-1}\bar{\Delta}_i + m\sigma_i^* \dot{\tau}_{id}\right\| \\
&\le -\frac{1}{m}\vartheta^T \vartheta + \frac{1}{2m}\vartheta^T \vartheta + \frac{1}{2m}\left(\bar{M}_i^{-1}\bar{\Delta}_i + m\sigma_i^* \dot{\tau}_{id}\right)^2 \\
&\le -\frac{1}{m}V_1 + \frac{1}{2m}\Xi^2
\end{aligned} \tag{217}$$

where $\left\|\bar{M}_i^{-1}\bar{\Delta}_i + m\sigma_i^* \dot{\tau}_{id}\right\| \le \Xi$, a Young's inequality is applied to $\left\|\vartheta\right\|\left\|\bar{M}_i^{-1}\bar{\Delta}_i + m\sigma_i^* \dot{\tau}_{id}\right\|$. Since $\dot{\tau}_{id}, \sigma_i^*$ and $\bar{\Delta}_i$ are bounded, $\left(\bar{M}_i^{-1}\bar{\Delta}_i + m\sigma_i^* \dot{\tau}_{id}\right)$ is bounded. From the comparison lemma in [152] raised as follows:

$$V_8 \le e^{-t/m}V_8(0) + \frac{1}{2}\Xi^2 \tag{218}$$

Thus, $\mathcal{G}$ will exponentially converge to a small compact set bounded by $\|\mathcal{G}(t)\| \le \sqrt{2V_1} \le \Xi$, where its size is determined by the filter parameter *m* and the upper bound of $\left\|\bar{M}_i^{-1}\bar{\Delta}_i + m\sigma_i^*\dot{\tau}_{id}\right\|$. We can be obtained

$$\lim_{t\to\infty}\|\mathcal{G}(t)\| = \Xi \tag{219}$$

which disappear for sufficiently small *m*, constant $\tau_{id}$ and $\bar{\Delta}_i$ = 0. Additionally, $\lim_{t\to 0}\left[\lim_{t\to\infty}\|\mathcal{G}(t)\|\right] = 0$, which means that $\mathcal{G}(t)$ converges to zero for any bounded $\mathcal{G}(0)$ and thus $\mathcal{G}(t)$ = 0 is an invariant manifold for $m \to 0$.

The proof is completed. ■

**Appendix 7.2**

Taking integral of the variables in (150), we have

$$\Upsilon_1 = \int_0^t e^{-a(t-\tau)}\sigma_i^{*T}(\tau)\sigma_i^*(\tau)d\tau;\ \ \Upsilon_2 = \int_0^t e^{-a(t-\tau)}\sigma_i^{*T}\sigma_i^{*\mathrm{T}}(\tau)\left(\frac{x_{2i}-x_{2i}^*}{a} - \Lambda_i^*\right)(\tau)d\tau \tag{220}$$

Then, substituting (220) into adaptive law (152) and combining (147). Therefore, we obtain the inequality as following

$$\begin{aligned}\|\Omega\| &\le \int_0^t e^{-a(t-\tau)}\left\|\sigma_i^*\right\|\left(\left\|\sigma_i^*\right\|\left(\tau_{id}(t) - \tau_{id}(\tau)\right) + \left\|\psi(\tau)\right\|\right)d\tau \\ &\le \int_0^t \left(2\mu_\sigma^2\varepsilon_{\tau_i} + \mu_\sigma\bar{\psi}\right)e^{-a(t-\tau)}d\tau \le \frac{1}{a}\left(2\mu_\sigma^2\varepsilon_{\tau_i} + \mu_\sigma\bar{\psi}\right).\end{aligned} \tag{221}$$

The proof of the boundedness of Ω is completed. ■

**Appendix 7.3**

In order to prove the Theorem 7.1, a Lyapunov candidate function is selected as follows:

$$V_9 = \frac{1}{2}\delta^{-1}\tilde{\tau}_{id}^T\kappa^{-1}\tilde{\tau}_{id} \tag{222}$$

Taking derivative is calculated along (151) and (152) as

$$
\begin{aligned}
\dot{V}_9 &= \delta^{-1}\tilde{\tau}_{id}^T\kappa^{-1}\dot{\tilde{\tau}}_{id} + 0.5\delta^{-1}\tilde{\tau}_{id}^T\dot{\kappa}^{-1}\tilde{\tau}_{id} \\
&= \delta^{-1}\tilde{\tau}_{id}^T\kappa^{-1}\left(\dot{\tilde{\tau}}_{id} + \delta\kappa\left[-\Upsilon_1\tilde{\tau}_{id} + \Omega - \eta\sigma_i^{*\mathrm{T}}\sigma_i^*\tilde{\tau}_{id} + \eta\sigma_i^*\psi\right]\right) + 0.5\delta^{-1}\tilde{\tau}_{id}^T\left(-a\kappa^{-1} + \sigma_i^{*\mathrm{T}}\sigma_i^*\right)\tilde{\tau}_{id} \\
&\le -\left(e^{-aT}\beta + \frac{ae^{-aT}\beta - \mu_{\sigma_i^*}^2}{2\|\delta\|} - \frac{3}{2\omega}\right)\|\tilde{\tau}_{id}\|^2 + 0.5\omega\left[\left(\mu_\sigma\bar{\psi}\beta\right)^2 + \frac{\mu_{\tau_{id}}^2}{\|\delta\|^2}\left(\lambda_{\min}(\kappa_0) + \mu_\sigma^2/a\right)^2\right. \\
&\qquad\qquad \left. + \frac{1}{a^2}\left(2\mu_\sigma^2\varepsilon_{\tau_{id}} + \mu_\sigma\bar{\psi}\right)^2\right] \\
&\le -\eta_{V_9}V_9 + \delta_{V_9}
\end{aligned}
\tag{223}
$$

where

$$
\eta_{V_9} = \frac{2\|\delta\|}{\lambda_{\min}(\kappa_0) + \mu_\sigma^2/a}\left(e^{-aT}\beta + \frac{ae^{-aT}\beta - \mu_\sigma^2}{2\|\delta\|} - \frac{3}{2\omega}\right)\|\tilde{\tau}_{id}\|^2
$$

$$
\delta_{V_9} = \frac{1}{2}\omega\left[\left(\mu_\sigma\bar{\psi}\beta\right)^2 + \frac{\mu_{\tau_{id}}^2}{\|\delta\|^2}\left(\lambda_{\min}(\kappa_0) + \mu_\sigma^2/a\right)^2 + \frac{1}{a^2}\left(2\mu_\sigma^2\varepsilon_{\tau_{id}} + \mu_\sigma\bar{\psi}\right)^2\right]
$$

$$
\left\|\dot{\tilde{\tau}}_{id}\right\| \le \mu_{\tau_{id}}
$$

and $\omega$ is a positive constant scalar. Based on [152], from the inequality (223)

$$
V_9(t) \le e^{-\eta_{V_2}t}V_9(0) + \frac{\delta_{V_9}}{\eta_{V_9}}. \tag{224}
$$

Therefore, the external force estimation errors converge to the compact set defined as follows

$$
\|\tilde{\tau}_{id}\| \le \sqrt{\frac{2\|\delta\|\delta_{V_9}\beta}{\eta_{V_2}e^{aT}}} = \bar{\zeta}_i \tag{225}
$$

The proof is completed. ■

**Appendix 7.4**

A Lyapunov candidate function is selected to proof the Theorem 7.2 as

$$
V_{10}(t) = \frac{1}{2}s_m^T\bar{M}_m s_m \tag{226}
$$

Using the derivative of (160), the time derivative of $V_{10}(t)$ can be written as

$$
\begin{aligned}
\dot{V}_{10} &= s_m^T \bar{M}_m \dot{s}_m + \frac{1}{2} s_m^T \dot{\bar{M}}_m s_m \\
&= s_m \left[ -\bar{M}_m \ddot{\bar{\theta}}_{mr} - \bar{C}_m \dot{\bar{\theta}}_{mr} - \bar{K}_m \theta_m + \tau_m - \tau_{md} - \bar{C}_m s_m \right] + \frac{1}{2} s_m^T \dot{\bar{M}}_m s_m \\
&\le s_m \left[ \varepsilon_m sign(s_m) - \rho_{1m} s_m - \rho_{2m} s_m^{[v_m]} + \hat{\tau}_{md} - \tau_{md} \right] + \frac{1}{2} s_m^T \left[ \dot{\bar{M}}_m - 2\bar{C}_m \right] s_m \\
&\le -\varepsilon_m |s_m| - \rho_{1m} s_m^2 - \rho_{2m} s_m^{[v_m+1]} + s_m \left( \hat{\tau}_{md} - \tau_{md} \right) \\
&\le -\rho_{1m} s_m^2 - \rho_{2m} s_m^{[v_m+1]} = -2\rho_{1m} V_{10} - 2\rho_{2m} V_{10}^{[v_m+1]/2}
\end{aligned}
\tag{227}
$$

According to the finite-time stability from [148] and [153], the variable sliding surfaces can converge to zero in finite time can converge to zero in a finite time. Then the tracking error $\tilde{\theta}_m$ can reach zero in a finite time.

The proof of Theorem 7.2 is completed. ■

**Appendix 7.5**

In order to demonstrate the Theorem 7.3, a Lyapunov candidate function is selected as

$$
V_{11}(t) = \frac{1}{2} s_s^T \bar{M}_s s_s \tag{228}
$$

Using the derivative of (165), the time derivative of $V_{11}(t)$ can be written as

$$
\begin{aligned}
\dot{V}_{11} &= s_s^T \bar{M}_s \dot{s}_s + \frac{1}{2} s_s^T \dot{\bar{M}}_s s_s \\
&= s_s \left[ -\bar{M}_s \ddot{\bar{\theta}}_{sr} - \bar{C}_s \dot{\bar{\theta}}_{sr} - \bar{K}_s \theta_s + \tau_s - \tau_{sd} - \bar{C}_s s_s \right] + \frac{1}{2} s_s^T \dot{\bar{M}}_s s_s \\
&= s_s \left[ \varepsilon_s sign(s_s) - \rho_{1s} s_s - \rho_{2s} s_s^{[v_s]} + \hat{\tau}_{sd} - \tau_{sd} \right] + \frac{1}{2} s_s^T \left[ \dot{\bar{M}}_s - 2\bar{C}_s \right] s_s \\
&= -\varepsilon_s |s_s| - \rho_{1s} s_s^2 - \rho_{2s} s_s^{[v_s+1]} + s_s \left( \hat{\tau}_{sd} - \tau_{sd} \right) \\
&\le -\rho_{1s} s_s^2 - \rho_{2s} s_s^{[v_s+1]} = -2\rho_{1s} V_{11} - 2\rho_{2s} V_{11}^{[v_s+1]/2}
\end{aligned}
\tag{229}
$$

For the finite-time stability from [148] and [153], the variable sliding surfaces can converge to zero in finite time can converge to zero in a finite time. Then the tracking error $\tilde{\theta}_s$ can reach zero in a finite time.

The proof of Theorem 7.3 is completed. ■

# PUBLICATIONS

***International Journal***

[1] **C. P. Vo**, M. Shahriar, C. D. Le, and K. K. Ahn, "Mechanically Active Transducing Element Based on Solid-Liquid Triboelectric Nanogenerator for Self-Powered Sensing," *Inter. J. Pr. Eng. Man.-GT*, vol. 6, no. 4, pp. 741-749, 2019. 10.1007/s40684-019-00143-z.

[2] M. Shahriar, **C. P. Vo,** and K. K. Ahn, "Self-powered Flexible PDMS Channel Assisted Discrete Liquid Column Motion Based Triboelectric Nanogenerator (DLC-TENG) as Mechanical Transducer," *Inter. J. Pr. Eng. Man.-GT*, vol. 6, no. 5, pp. 907-917, 2019. 10.1007/s40684-019-00148-8.

[3] **C. P. Vo**, X. D. To, and K. K. Ahn, "A Novel Adaptive Gain Integral Terminal Sliding Mode Control scheme of a Pneumatic Artificial Muscle system with Time-delay Estimation", *IEEE Access*, vol. 7, pp. 141133-141143, 2019. 10.1109/ACCESS.2019.2944197.

[4] **C. P. Vo**, X. D. To, and K. K. Ahn, "A Novel Force Sensorless Reflecting Control for Bilateral Haptic Teleoperation System", *IEEE Access*, vol. 8, pp. 96515-96527, 2020. 10.1109/ACCESS.2020.2994374.

[5] G. H. Nam, J. H. Ahn, G. H. Lee, **C. P. Vo**, and K. K. Ahn, "A New Pathway for Liquid-Solid Triboelectric Nanogenerator Using Streaming Flow by a Novel Direct Charge Transfer," *Advanced Energy and Sustainability Research*, pp. 2000031, 2020. 10.1002/aesr.202000031.

[6] C. D. Le*, **C. P. Vo***, T. H. Nguyen, D. L. Nguyen and K. K. Ahn, "Liquid-Solid Contact Electrification Based on Discontinuous-Conduction Triboelectric Nanogenerator Induced by Radially Symmetrical Structure", *Nano Energy*, vol. 80 pp. 105571, 2021. 10.1016/j.nanoen.2020.105571.

***International Conferences***

[7] **C. P. Vo** and K. K. Ahn, "High-precision Position Control of Soft Actuator Systems, " *The 3rd International Workshop on Active Materials and Soft Mechatronics (AMSM2018)*, KAIST, Daejeon, South Korea, Oct. 2018.

[8] **C. P. Vo**, D. T. Tran and K. K. Ahn, "The Predictive Control for Networked Control System with Random Delays and Packet Dropouts," in *2018 22nd International Conference on Mechatronics Technology (ICMT)*, Jeju, South Korea, Oct. 2018.

[9] **C. P. Vo**, X. D. To, and K. K. Ahn, "Variable Impedance Control for a Robotic Leg with External Uncertainties," in *2019 23rd International Conference on Mechatronics Technology (ICMT)*, SALERNO, Italy, Oct. 2019, 10.1109/ICMECT.2019.8932102.

[10] D. T. Tran, C. D. Le, **C. P. Vo** and K. K. Ahn, " Robust network predictive control for DC motor with delay and dropout," in *2018 22nd International Conference on Mechatronics Technology (ICMT)*, Jeju, South Korea, Oct. 2018.

***Ongoing***

[11] **C. P. Vo**, V. D. Phan, T. H. Nguyen and K. K. Ahn, "A Novel Compact and Adjustable Stiffness Rotary Actuator based on Linear Springs: Working Principle design and Experimental Verification", *Mech. Syst. Signal Process.*

[12] **C. P. Vo**, and K. K. Ahn, "Survey on the control strategies for bilateral teleoperation systems", *Electronics*

[13] **C. P. Vo** and K. K. Ahn, "A Novel Adaptive Finite-Time Force Sensorless Control scheme of a PAM system with TDE", *Mech. Syst. Signal Process.*

[14] **C. P. Vo** and K. K. Ahn, "Model-free control for Optimal contact force of a Pneumatic Artificial Muscles system in Unknown Environments using Reinforcement Learning", *Mech. Syst. Signal Process.*

[15] D. L. Nguyen, **C. P. Vo**, C. D. Le and K. K. Ahn, "Enhancing the Output Performance of Fluid based Triboelectric Nanogenerator by Using PVDF-HFP/Ionic Liquid Nanoporous Membrane", *Applied Energy*

[16] V. D. Phan, **C. P. Vo,** H. V. Dao and K. K. Ahn, "Robust fault-tolerant control of an electro-hydraulic actuator with a novel nonlinear unknown input observer", *IEEE Access.*

[17] H. V. A. Truong, T. D. Dang, **C. P. Vo**, and K. K. Ahn, "Feasibility of Active Control Strategies for Load Mitigation and System Enhancement on Floating Offshore Wind Turbines: A Review", *Renew. Sust. Energ. Rev.*

# REFERENCES


[1] P. F. Hokayem, and M. W. Spong, "Bilateral teleoperation: An historical survey," *Automatica,* vol. 42, no. 12, pp. 2035-2057, Dec, 2006.

[2] W. Ting, and S. Aiguo, "An Adaptive Iterative Learning Based Impedance Control for Robot-Aided Upper-Limb Passive Rehabilitation," *Frontiers in Robotics and AI,* vol. 6, no. 41, 2019-June-04, 2019.

[3] Q.-T. Dao, and S.-i. Yamamoto, "Assist-as-Needed Control of a Robotic Orthosis Actuated by Pneumatic Artificial Muscle for Gait Rehabilitation," *Appl. Sci.,* vol. 8, no. 4, 2018.

[4] M. M. Zhang, S. Q. Xie, X. L. Li, G. L. Zhu, W. Meng, X. L. Huang, and A. J. Veale, "Adaptive Patient-Cooperative Control of a Compliant Ankle Rehabilitation Robot (CARR) With Enhanced Training Safety," *IEEE Trans. Ind. Electron.,* vol. 65, no. 2, pp. 1398-1407, Feb, 2018.

[5] M. Farag, and N. Z. Azlan, "Adaptive Backstepping Position Control of Pneumatic Anthropomorphic Robotic Hand," *Procedia Computer Science,* vol. 76, pp. 161-167, 2015/01/01/, 2015.

[6] J. Furukawa, T. Noda, T. Teramae, and J. Morimoto, "An EMG-Driven Weight Support System With Pneumatic Artificial Muscles," *Ieee Systems Journal,* vol. 10, no. 3, pp. 1026-1034, Sep, 2016.

[7] C. Ching-Ping, and B. Hannaford, "Measurement and modeling of McKibben pneumatic artificial muscles," *IEEE Trans. Robot. Autom.,* vol. 12, no. 1, pp. 90-102, 1996.

[8] D. B. Reynolds, D. W. Repperger, C. A. Phillips, and G. Bandry, "Modeling the dynamic characteristics of pneumatic muscle," *Ann Biomed Eng,* vol. 31, no. 3, pp. 310-7, Mar, 2003.

[9] M. Tothova, and J. Pitel, "Dynamic model of pneumatic actuator based on advanced geometric muscle model," in 2013 IEEE 9th International Conference on Computational Cybernetics (ICCC), Tihany, 2013, pp. 8-87.

[10] T. Tagami, T. Miyazaki, T. Kawase, T. Kanno, and K. Kawashima, "Pressure Control of a Pneumatic Artificial Muscle Including Pneumatic Circuit Model," *IEEE Access,* vol. 8, pp. 60526-60538, 2020.

[11] H. B. Li, K. Kawashima, K. Tadano, S. Ganguly, and S. Nakano, "Achieving Haptic Perception in Forceps' Manipulator Using Pneumatic Artificial Muscle," *Ieee-Asme Transactions on Mechatronics,* vol. 18, no. 1, pp. 74-85, Feb, 2013.

[12] H. P. H. Anh, "Online tuning gain scheduling MIMO neural PID control of the 2-axes pneumatic artificial muscle (PAM) robot arm," *Expert Systems with Applications,* vol. 37, no. 9, pp. 6547-6560, 2010.

[13] D. H. Zhang, X. G. Zhao, and J. D. Han, "Active Model-Based Control for Pneumatic Artificial Muscle," *IEEE Trans. Ind. Electron.,* vol. 64, no. 2, pp. 1686-1695, Feb, 2017.

[14] A. Merola, D. Colacino, C. Cosentino, and F. Amato, "Model-based tracking control design, implementation of embedded digital controller and testing of a biomechatronic device for robotic rehabilitation," *Mechatronics,* vol. 52, pp. 70-77, Jun, 2018.

[15] R. Kelly, Santibáñez Davila, Victor, Loría Perez, Julio Antonio, "Control of Robot Manipulators in Joint Space (Advanced Textbooks in Control and Signal Processing)." in *Book Control of Robot Manipulators in Joint Space (Advanced Textbooks in Control and Signal Processing).* New York: Springer-Verlag, 2005.

[16] T. U. D. C. Thanh, and K. K. Ahn, "Nonlinear PID control to improve the control performance of 2 axes pneumatic artificial muscle manipulator using neural network," *Mechatronics,* vol. 16, no. 9, pp. 577-587, 2006.

[17] G. Andrikopoulos, G. Nikolakopoulos, I. Arvanitakis, and S. Manesis, "Piecewise Affine Modeling and Constrained Optimal Control for a Pneumatic Artificial Muscle," *IEEE Trans. Ind. Electron.,* vol. 61, no. 2, pp. 904-916, Feb, 2014.

[18] H. Aschemann, and D. Schindele, "Sliding-Mode Control of a High-Speed Linear Axis Driven by Pneumatic Muscle Actuators," *IEEE Trans. Ind. Electron.,* vol. 55, no. 11, pp. 3855-3864, Nov, 2008.

[19] H. Nejatbakhsh Esfahani, V. Azimirad, and M. Danesh, "A Time Delay Controller included terminal sliding mode and fuzzy gain tuning for Underwater Vehicle-Manipulator Systems," *Ocean Engineering,* vol. 107, pp. 97-107, 10/1/, 2015.

[20] Q. Ai, C. Zhu, J. Zuo, W. Meng, Q. Liu, S. Q. Xie, and M. Yang, "Disturbance-Estimated Adaptive Backstepping Sliding Mode Control of a Pneumatic Muscles-Driven Ankle Rehabilitation Robot," *Sensors (Basel),* vol. 18, no. 1, Dec 28, 2017.

[21] Z. Man, and Y. Xing Huo, "Terminal sliding mode control of MIMO linear systems," *IEEE Transactions on Circuits and Systems I: Fundamental Theory and Applications,* vol. 44, no. 11, pp. 1065-1070, 1997.

[22] Y. Feng, X. Yu, and Z. Man, "Non-singular terminal sliding mode control of rigid manipulators," *Automatica,* vol. 38, no. 12, pp. 2159-2167, 12//, 2002.

[23] T. A. Vo, and H.-J. Kang, "An Adaptive Neural Non-Singular Fast-Terminal Sliding-Mode Control for Industrial Robotic Manipulators," *Applied Sciences,* vol. 8, no. 12, 2018.

[24] H. S. Lee, S. J. Won, and K. K. Ahn, "The Numerical Modeling and Sliding Mode Control of A New Submersible Fish Cage," *Journal of Drive and Control,* vol. 14, no. 3, pp. 18-24, 06/01, 2017.
[25] S. F. Wu, and J. W. Zhang, "A Terminal Sliding Mode Observer Based Robust Backstepping Sensorless Speed Control for Interior Permanent Magnet Synchronous Motor," *International Journal of Control Automation and Systems,* vol. 16, no. 6, pp. 2743-2753, Dec, 2018.
[26] K. Oh, and J. Seo, "Sliding Mode Observer-based Fault Detection Algorithm for Steering Input of an All-Terrain Crane," *Journal of Drive and Control,* vol. 14, no. 2, pp. 30-36, 06/01, 2017.
[27] S. Mobayen, "Adaptive Global Terminal Sliding Mode Control Scheme with Improved Dynamic Surface for Uncertain Nonlinear Systems," *International Journal of Control Automation and Systems,* vol. 16, no. 4, pp. 1692-1700, Aug, 2018.
[28] E. Rouhani, and A. Erfanian, "A Finite-time Adaptive Fuzzy Terminal Sliding Mode Control for Uncertain Nonlinear Systems," *International Journal of Control Automation and Systems,* vol. 16, no. 4, pp. 1938-1950, Aug, 2018.
[29] Z. R. Cao, Y. G. Niu, and H. J. Zhao, "Finite-time Sliding Mode Control of Markovian Jump Systems Subject to Actuator Faults," *International Journal of Control Automation and Systems,* vol. 16, no. 5, pp. 2282-2289, Oct, 2018.
[30] F. Castanos, and L. Fridman, "Analysis and design of integral sliding manifolds for systems with unmatched perturbations," *IEEE Transactions on Automatic Control,* vol. 51, no. 5, pp. 853-858, 2006.
[31] S. I. Han, and J. M. Lee, "Adaptive Fuzzy Backstepping Dynamic Surface Control for Output-constrained Non-smooth Nonlinear Dynamic System," *International Journal of Control Automation and Systems,* vol. 10, no. 4, pp. 684-696, Aug, 2012.
[32] V. T. Yen, W. Y. Nan, P. V. Cuong, N. X. Quynh, and V. H. Thich, "Robust adaptive sliding mode control for industrial robot manipulator using fuzzy wavelet neural networks," *International Journal of Control Automation and Systems,* vol. 15, no. 6, pp. 2930-2941, Dec, 2017.
[33] J. Fei, Y. Chu, and S. Hou, "A Backstepping Neural Global Sliding Mode Control Using Fuzzy Approximator for Three-Phase Active Power Filter," *IEEE Access,* vol. 5, pp. 16021-16032, 2017.
[34] X. Ma, F. C. Sun, H. B. Li, and B. He, "Neural-network-based Integral Sliding-mode Tracking Control of Second-order Multi-agent Systems with Unmatched Disturbances and Completely Unknown Dynamics," *International Journal of Control Automation and Systems,* vol. 15, no. 4, pp. 1925-1935, Aug, 2017.
[35] D. B. Tong, L. P. Zhang, W. N. Zhou, J. Zhou, and Y. H. Xu, "Asymptotical Synchronization for Delayed Stochastic Neural Networks with Uncertainty via Adaptive Control," *International Journal of Control Automation and Systems,* vol. 14, no. 3, pp. 706-712, Jun, 2016.
[36] W. J. Si, X. D. Dong, and F. F. Yang, "Adaptive Neural Dynamic Surface Control for a General Class of Stochastic Nonlinear Systems with Time Delays and Input Dead-zone," *International Journal of Control Automation and Systems,* vol. 15, no. 5, pp. 2416-2424, Oct, 2017.
[37] T. X. Dinh, and K. K. Ahn, "Radial basis function neural network based adaptive fast nonsingular terminal sliding mode controller for piezo positioning stage," *International Journal of Control Automation and Systems,* vol. 15, no. 6, pp. 2892-2905, Dec, 2017.
[38] M. Defoort, T. Floquet, W. Perruquetti, and S. V. Drakunov, "Integral sliding mode control of an extended Heisenberg system," *IET Control Theory & Applications,* vol. 3, no. 10, pp. 1409-1424, 2009.
[39] M. Van, "Adaptive neural integral sliding-mode control for tracking control of fully actuated uncertain surface vessels," *International Journal of Robust and Nonlinear Control,* vol. 29, no. 5, pp. 1537-1557, 2019/03/25, 2019.
[40] T. X. Dinh, T. D. Thien, T. H. V. Anh, and K. K. Ahn, "Disturbance Observer Based Finite Time Trajectory Tracking Control for a 3 DOF Hydraulic Manipulator Including Actuator Dynamics," *IEEE Access,* vol. 6, pp. 36798-36809, 2018.
[41] M. Rubagotti, A. Estrada, F. Castanos, A. Ferrara, and L. Fridman, "Integral Sliding Mode Control for Nonlinear Systems With Matched and Unmatched Perturbations," *IEEE Transactions on Automatic Control,* vol. 56, no. 11, pp. 2699-2704, 2011.
[42] Y. Park, N. Paine, and S. Oh, "Development of Force Observer in Series Elastic Actuator for Dynamic Control," *IEEE Trans. Ind. Electron.,* vol. 65, no. 3, pp. 2398-2407, 2018.
[43] A. S. a. D. J. Braun, "[40] Enhancing Mobility With Quasi-Passive Variable Stiffness Exoskeletons," 2019.
[44] C. P. Vo, X. D. To, and K. K. Ahn, "A Novel Adaptive Gain Integral Terminal Sliding Mode Control Scheme of a Pneumatic Artificial Muscle System With Time-Delay Estimation," *IEEE Access,* vol. 7, pp. 141133-141143, 2019.
[45] Q. Liu, A. Liu, W. Meng, Q. Ai, and S. Q. Xie, "Hierarchical Compliance Control of a Soft Ankle Rehabilitation Robot Actuated by Pneumatic Muscles," *Front Neurorobot,* vol. 11, pp. 64, 2017.

[46] N. Hogan, "Impedance Control: An Approach to Manipulation." pp. 304-313.
[47] G. W. Zeng, and A. Hemami, “An overview of robot force control,” *Robotica,* vol. 15, no. 5, pp. 473-482, Sep-Oct, 1997.
[48] A. Sabanovic, and I. Khalil, "Sensorless Torque/Force Control," *Advances in Motor Torque Control*, 2011.
[49] H. Yang, X. Gao, Y. Chen, and L. Hao, “Hammerstein Adaptive Impedance Controller for Bionic Wrist Joint Actuated by Pneumatic Muscles,” *IEEE Access,* vol. 7, pp. 47-56, 2019.
[50] A. E. K. Mohammad, J. Hong, and D. Wang, “Design of a force-controlled end-effector with low-inertia effect for robotic polishing using macro-mini robot approach,” *Robotics and Computer-Integrated Manufacturing,* vol. 49, pp. 54-65, 2018.
[51] F. Chen, H. Zhao, D. Li, L. Chen, C. Tan, and H. Ding, “Contact force control and vibration suppression in robotic polishing with a smart end effector,” *Robotics and Computer-Integrated Manufacturing,* vol. 57, pp. 391-403, 2019.
[52] L. Zhao, C. Zheng, Y. Wang, and B. Liu, “A Finite-Time Control for a Pneumatic Cylinder Servo System Based on a Super-Twisting Extended State Observer,” *IEEE Trans. Syst. Man Cybern. Syst.,* pp. 1-10, 2019.
[53] X. R. Shen, “Nonlinear model-based control of pneumatic artificial muscle servo systems,” *Control Engineering Practice,* vol. 18, no. 3, pp. 311-317, Mar, 2010.
[54] Y. Yuan, Y. Yu, and L. Guo, “Nonlinear Active Disturbance Rejection Control for the Pneumatic Muscle Actuators With Discrete-Time Measurements,” *IEEE Trans. Ind. Electron.,* vol. 66, no. 3, pp. 2044-2053, 2019.
[55] Z. Chen, F. H. Huang, C. N. Yang, and B. Yao, “Adaptive Fuzzy Backstepping Control for Stable Nonlinear Bilateral Teleoperation Manipulators With Enhanced Transparency Performance,” *IEEE Trans. Ind. Electron.,* vol. 67, no. 1, pp. 746-756, Jan, 2020.
[56] H. Amini, B. Farzaneh, F. Azimifar, and A. A. D. Sarhan, “Sensor-less force-reflecting macro–micro telemanipulation systems by piezoelectric actuators,” *ISA Transactions,* vol. 64, pp. 293-302, 2016/09/01/, 2016.
[57] L. Chan, F. Naghdy, and D. Stirling, “An Improved Extended Active Observer for Adaptive Control of A n−DOF Robot Manipulator,” *Journal of Intelligent & Robotic Systems,* vol. 85, no. 3, pp. 679-692, 2017/03/01, 2017.
[58] Y. Yuan, Y. J. Wang, and L. Guo, “Force Reflecting Control for Bilateral Teleoperation System Under Time-Varying Delays,” *IEEE Trans. Ind. Informat.,* vol. 15, no. 2, pp. 1162-1172, Feb, 2019.
[59] C. Mitsantisuk, K. Ohishi, and S. Katsura, “Estimation of Action/Reaction Forces for the Bilateral Control Using Kalman Filter,” *IEEE Trans. Ind. Electron.,* vol. 59, no. 11, pp. 4383-4393, 2012.
[60] T. T. Phuong, K. Ohishi, and Y. Yokokura, “Fine Sensorless Force Control Realization Based on Dither Periodic Component Elimination Kalman Filter and Wide Band Disturbance Observer,” *IEEE Transactions on Industrial Electronics,* vol. 67, no. 1, pp. 757-767, 2020.
[61] H. Zhu, and H. Fujimoto, “Suppression of Current Quantization Effects for Precise Current Control of SPMSM Using Dithering Techniques and Kalman Filter,” *IEEE Transactions on Industrial Informatics,* vol. 10, no. 2, pp. 1361-1371, 2014.
[62] K. Ogata, “Modern Control Engineering,” in *Book Modern Control Engineering*: Prentice Hall PTR, 2001.
[63] A. Levant, “Higher-order sliding modes, differentiation and output-feedback control,” *Int. J. Control,* vol. 76, no. 9-10, pp. 924-941, 2003/01/01, 2003.
[64] J. Na, Y. Li, Y. Huang, G. Gao, and Q. Chen, “Output Feedback Control of Uncertain Hydraulic Servo Systems,” *IEEE Transactions on Industrial Electronics,* vol. 67, no. 1, pp. 490-500, 2020.
[65] A. Levant, “Robust exact differentiation via sliding mode technique,” *Automatica,* vol. 34, no. 3, pp. 379-384, 1998.
[66] J. E. Slightam, and M. L. Nagurka, "Modeling of Pneumatic Artificial Muscle with Kinetic Friction and Sliding Mode Control." pp. 3342-3347.
[67] S. H. Yu, X. H. Yu, B. Shirinzadeh, and Z. H. Man, “Continuous finite-time control for robotic manipulators with terminal sliding mode,” *Automatica,* vol. 41, no. 11, pp. 1957-1964, Nov, 2005.
[68] J. Lee, M. Jin, N. Kashiri, D. G. Caldwell, and N. G. Tsagarakis, “Inversion-free force tracking control of piezoelectric actuators using fast finite-time integral terminal sliding-mode,” *Mechatronics,* vol. 57, pp. 39-50, 2019.
[69] S. Chiaverini, B. Siciliano, and L. Villani, “A survey of robot interaction control schemes with experimental comparison,” *IEEE/ASME Trans. Mechatron.,* vol. 4, no. 3, pp. 273-285, 1999.
[70] W. Yu, and A. Perrusquía, “Simplified Stable Admittance Control Using End-Effector Orientations,” *International Journal of Social Robotics*, 2019.

[71] J. Z. Peng, Z. Q. Yang, and T. L. Ma, “Position/Force Tracking Impedance Control for Robotic Systems with Uncertainties Based on Adaptive Jacobian and Neural Network,” *Complexity,* vol. 2019, pp. 1-16, 2019.
[72] K. X. Ba, B. Yu, Z. J. Gao, W. F. Li, G. L. Ma, and X. D. Kong, “Parameters Sensitivity Analysis of Position-Based Impedance Control for Bionic Legged Robots' HDU,” *Applied Sciences-Basel,* vol. 7, no. 10, Oct, 2017.
[73] D. S. Cheon, and K. H. Nam, “Pedaling torque sensor-less power assist control of an electric bike via model-based impedance control,” *International Journal of Automotive Technology,* vol. 18, no. 2, pp. 327-333, Apr, 2017.
[74] S. Devie, P.-P. Robet, Y. Aoustin, and M. Gautier, “Impedance Control Using a Cascaded Loop Force Control,” *IEEE Robotics and Automation Letters,* vol. 3, no. 3, pp. 1537-1543, 2018.
[75] M. Tufail, and C. W. d. Silva, "Impedance control schemes for bilateral teleoperation." pp. 44-49.
[76] F. Dimeas, and N. Aspragathos, “Online Stability in Human-Robot Cooperation with Admittance Control,” *IEEE Trans Haptics,* vol. 9, no. 2, pp. 267-78, Apr-Jun, 2016.
[77] M. Matinfar, and K. Hashtrudi-Zaad, “Optimization-based Robot Compliance Control: Geometric and Linear Quadratic Approaches,” *Int. J. Robot Res.,* vol. 24, no. 8, pp. 645-656, 2005.
[78] R. G. Bonitz, and T. C. Hsia, “Internal force-based impedance control for cooperating manipulators,” *IEEE Trans. Robot. Autom.,* vol. 12, no. 1, pp. 78-89, Feb, 1996.
[79] C. Wang, Y. Li, S. S. Ge, and T. H. Lee, “Optimal critic learning for robot control in time-varying environments,” *IEEE Trans Neural Netw Learn Syst,* vol. 26, no. 10, pp. 2301-10, Oct, 2015.
[80] A. Perrusquía, W. Yu, A. Soria, and R. Lozano, “Stable admittance control without inverse kinematics,” *IFAC-PapersOnLine,* vol. 50, no. 1, pp. 15835-15840, 2017/07/01/, 2017.
[81] T. Yamamoto, M. Bernhardt, A. Peer, M. Buss, and A. M. Okamura, "Techniques for environment parameter estimation during telemanipulation." pp. 217-223.
[82] W. S. Lu, and Q. H. Meng, “Impedance control with adaptation for robotic manipulations,” *IEEE Trans. Robot. Autom.,* vol. 7, no. 3, pp. 408-415, 1991.
[83] “Reinforcement Learning and Feedback Control: Using Natural Decision Methods to Design Optimal Adaptive Controllers,” *IEEE Control Systems,* vol. 32, no. 6, pp. 76-105, 2012.
[84] A. G. B. R.S. Sutton, “Reinforcement Learning: An Introduction,” in *Book Reinforcement Learning: An Introduction,* Cambridge, MA: MIT Press, 1998.
[85] A. Perrusquía, W. Yu, and A. Soria, “Position/force control of robot manipulators using reinforcement learning,” *Industrial Robot: the international journal of robotics research and application,* vol. 46, no. 2, pp. 267-280, 2019.
[86] C. Yang, G. Peng, Y. Li, R. Cui, L. Cheng, and Z. Li, “Neural Networks Enhanced Adaptive Admittance Control of Optimized Robot-Environment Interaction,” *IEEE Trans Cybern,* vol. 49, no. 7, pp. 2568-2579, Jul, 2019.
[87] K. D. Kallu, J. Wang, S. J. Abbasi, and M. C. Lee, “Estimated Reaction Force-Based Bilateral Control between 3DOF Master and Hydraulic Slave Manipulators for Dismantlement,” *Electronics,* vol. 7, no. 10, Oct, 2018.
[88] M. Zheng, T. Q. Yuan, and T. Huang, “Time-Varying Impedance Control of Port Hamiltonian System with a New Energy-Storing Tank,” *Complexity,* vol. 2018, pp. 1-10, 2018.
[89] H. Y. Li, I. Paranawithana, L. J. Yang, T. S. K. Lim, S. Foong, F. C. Ng, and U. X. Tan, “Stable and Compliant Motion of Physical Human-Robot Interaction Coupled With a Moving Environment Using Variable Admittance and Adaptive Control,” *Ieee Robotics and Automation Letters,* vol. 3, no. 3, pp. 2493-2500, Jul, 2018.
[90] M.-C. Chien, and A.-C. Huang, “Adaptive Impedance Control of Robot Manipulators based on Function Approximation Technique,” *Robotica,* vol. 22, no. 4, pp. 395-403, 2004.
[91] C. P. Vo, X. D. To, and K. K. Ahn, “A Novel Force Sensorless Reflecting Control for Bilateral Haptic Teleoperation System,” *IEEE Access,* pp. 1-1, 2020.
[92] W. Yu, J. Rosen, and X. Li, "PID admittance control for an upper limb exoskeleton." pp. 1124-1129.
[93] J. Seul, T. C. Hsia, and R. G. Bonitz, “Force tracking impedance control of robot manipulators under unknown environment,” *IEEE Trans. Control Syst. Technol.,* vol. 12, no. 3, pp. 474-483, 2004.
[94] J. T. Wen, and S. Murphy, “Stability analysis of position and force control for robot arms,” *IEEE Trans. Autom. Control,* vol. 36, no. 3, pp. 365-371, 1991.
[95] L. S. Wilfinger, J. T. Wen, and S. H. Murphy, “Integral force control with robustness enhancement,” *IEEE Contr. Syst. Mag.,* vol. 14, no. 1, pp. 31-40, 1994.
[96] D. Vrabie, O. Pastravanu, M. Abu-Khalaf, and F. L. Lewis, “Adaptive optimal control for continuous-time linear systems based on policy iteration,” *Automatica,* vol. 45, no. 2, pp. 477-484, Feb, 2009.

[97] K. Doya, "Reinforcement learning in continuous time and space," *Neural Comput,* vol. 12, no. 1, pp. 219-45, Jan, 2000.
[98] L. Busoniu, R. Babuska, B. D. Schutter, and D. Ernst, "Reinforcement Learning and Dynamic Programming Using Function Approximators," in *Book Reinforcement Learning and Dynamic Programming Using Function Approximators*: CRC Press, Inc., 2010.
[99] S. Suzuki, and K. Furuta, "Adaptive Impedance Control to Enhance Human Skill on a Haptic Interface System," *Journal of Control Science and Engineering,* vol. 2012, pp. 1-10, 2012.
[100] S. Baron, D. L. Kleinman, and W. H. Levison, "An optimal control model of human response part II: Prediction of human performance in a complex task," *Automatica,* vol. 6, no. 3, pp. 371-383, 1970/05/01/, 1970.
[101] S. Franklin, D. M. Wolpert, and D. W. Franklin, "Visuomotor feedback gains upregulate during the learning of novel dynamics," *J Neurophysiol,* vol. 108, no. 2, pp. 467-78, Jul, 2012.
[102] T. Tsuji, and Y. Tanaka, "Tracking Control Properties of Human–Robotic Systems Based on Impedance Control," *IEEE Transactions on Systems, Man, and Cybernetics - Part A: Systems and Humans,* vol. 35, no. 4, pp. 523-535, 2005.
[103] V. Duchaine, and C. Gosselin, "Safe, Stable and Intuitive Control for Physical Human-Robot Interaction." pp. 3383-3388.
[104] R. Ikeura, T. Moriguchi, and K. Mizutani, "Optimal variable impedance control for a robot and its application to lifting an object with a human." pp. 500-505.
[105] A. Munawar, and G. Fischer, "A Surgical Robot Teleoperation Framework for Providing Haptic Feedback Incorporating Virtual Environment-Based Guidance," *Frontiers in Robotics and AI,* vol. 3, no. 47, 2016-August-09, 2016.
[106] S. Oh, H. Woo, and K. Kong, "Frequency-Shaped Impedance Control for Safe Human-Robot Interaction in Reference Tracking Application," *Ieee-Asme Transactions on Mechatronics,* vol. 19, no. 6, pp. 1907-1916, Dec, 2014.
[107] A. Kouris, F. Dimeas, and N. Aspragathos, "A Frequency Domain Approach for Contact Type Distinction in Human-Robot Collaboration," *Ieee Robotics and Automation Letters,* vol. 3, no. 2, pp. 720-727, Apr, 2018.
[108] S. Cremer, S. K. Das, I. B. Wijayasinghe, D. O. Popa, and F. L. Lewis, "Model-Free Online Neuroadaptive Controller With Intent Estimation for Physical Human–Robot Interaction," *IEEE T. Robot.,* vol. 36, no. 1, pp. 240-253, 2020.
[109] K. Furuta, Y. Kado, and S. Shiratori, "Assisting control in Human Adaptive Mechatronics — single ball juggling —." pp. 545-550.
[110] K. Kurihara, S. Suzuki, F. Harashima, and K. Furuta, "Human adaptive mechatronics (HAM) for haptic system." pp. 647-652 Vol. 1.
[111] A. Suarez, G. Heredia, and A. Ollero, "Physical-Virtual Impedance Control in Ultralightweight and Compliant Dual-Arm Aerial Manipulators," *IEEE Robotics and Automation Letters,* vol. 3, no. 3, pp. 2553-2560, 2018.
[112] M. H. Vu, and U. J. Na, "A New 6-DOF Haptic Device for Teleoperation of 6-DOF Serial Robots," *Ieee Transactions on Instrumentation and Measurement,* vol. 60, no. 11, pp. 3510-3523, Nov, 2011.
[113] C. Mitsantisuk, K. Ohishi, and S. Katsura, "Variable mechanical stiffness control based on human stiffness estimation." pp. 731-736.
[114] R. Wu, H. Zhang, T. Peng, L. Fu, and J. Zhao, "Variable impedance interaction and demonstration interface design based on measurement of arm muscle co-activation for demonstration learning," *Biomedical Signal Processing and Control,* vol. 51, pp. 8-18, May, 2019.
[115] L. Roveda, N. Iannacci, F. Vicentini, N. Pedrocchi, F. Braghin, and L. M. Tosatti, "Optimal Impedance Force-Tracking Control Design With Impact Formulation for Interaction Tasks," *IEEE Robotics and Automation Letters,* vol. 1, no. 1, pp. 130-136, 2016.
[116] C. Wang, Y. Li, S. S. Ge, K. P. Tee, and T. H. Lee, "Continuous critic learning for robot control in physical human-robot interaction." pp. 833-838.
[117] Y. C. Wu, F. W. Chen, T. T. Liao, and C. T. Chen, "Force reflection in a pneumatic artificial muscle actuated haptic system," *Mechatronics,* vol. 61, pp. 37-48, Aug, 2019.
[118] F. Dimeas, and N. Aspragathos, "Reinforcement learning of variable admittance control for human-robot co-manipulation." pp. 1011-1016.
[119] H. Modares, I. Ranatunga, F. L. Lewis, and D. O. Popa, "Optimized Assistive Human-Robot Interaction Using Reinforcement Learning," *IEEE Trans Cybern,* vol. 46, no. 3, pp. 655-67, Mar, 2016.
[120] C. Chen, H. Modares, K. Xie, F. L. Lewis, Y. Wan, and S. L. Xie, "Reinforcement Learning-Based Adaptive Optimal Exponential Tracking Control of Linear Systems With Unknown Dynamics," *IEEE Trans. Autom. Control,* vol. 64, no. 11, pp. 4423-4438, Nov, 2019.

[121] L. Roveda, J. Maskani, P. Franceschi, A. Abdi, F. Braghin, L. Molinari Tosatti, and N. Pedrocchi, "Model-Based Reinforcement Learning Variable Impedance Control for Human-Robot Collaboration," *J. Intell. Robot. Syst.*, 2020.
[122] G. Bingjing, H. Jianhai, L. Xiangpan, and Y. Lin, "Human–robot interactive control based on reinforcement learning for gait rehabilitation training robot," *International Journal of Advanced Robotic Systems*, vol. 16, no. 2, 2019.
[123] Y. N. Li, S. S. Ge, Q. Zhang, and T. H. Lee, "Neural networks impedance control of robots interacting with environments," *Iet Control Theory and Applications*, vol. 7, no. 11, pp. 1509-1519, Jul, 2013.
[124] H. Modares, F. L. Lewis, and M.-B. Naghibi-Sistani, "Integral reinforcement learning and experience replay for adaptive optimal control of partially-unknown constrained-input continuous-time systems," *Automatica*, vol. 50, no. 1, pp. 193-202, 2014.
[125] H. Modares, F. L. Lewis, and M. B. Naghibi-Sistani, "Adaptive optimal control of unknown constrained-input systems using policy iteration and neural networks," *IEEE Trans Neural Netw Learn Syst*, vol. 24, no. 10, pp. 1513-25, Oct, 2013.
[126] B. Kiumarsi, F. L. Lewis, M. B. Naghibi-Sistani, and A. Karimpour, "Optimal Tracking Control of Unknown Discrete-Time Linear Systems Using Input-Output Measured Data," *IEEE Trans Cybern*, vol. 45, no. 12, pp. 2770-9, Dec, 2015.
[127] H. Modares, and F. L. Lewis, "Linear Quadratic Tracking Control of Partially-Unknown Continuous-Time Systems Using Reinforcement Learning," *IEEE Trans. Autom. Control*, vol. 59, no. 11, pp. 3051-3056, Nov, 2014.
[128] D. Vrabie, and F. Lewis, "Neural network approach to continuous-time direct adaptive optimal control for partially unknown nonlinear systems," *Neural Netw*, vol. 22, no. 3, pp. 237-46, Apr, 2009.
[129] Y. Jiang, and Z.-P. Jiang, "Computational adaptive optimal control for continuous-time linear systems with completely unknown dynamics," *Automatica*, vol. 48, no. 10, pp. 2699-2704, 2012.
[130] J. Y. Lee, J. B. Park, and Y. H. Choi, "Integral reinforcement learning for continuous-time input-affine nonlinear systems with simultaneous invariant explorations," *IEEE Trans Neural Netw Learn Syst*, vol. 26, no. 5, pp. 916-32, May, 2015.
[131] J. Brewer, "Kronecker products and matrix calculus in system theory," *IEEE Transactions on Circuits and Systems*, vol. 25, no. 9, pp. 772-781, 1978.
[132] D. Wang, K. Ohnishi, and W. Xu, "Novel Emerging Sensing, Actuation, and Control Techniques for Haptic Interaction and Teleoperation," *IEEE Trans. Ind. Electron.*, vol. 67, no. 1, pp. 624-626, Jan, 2020.
[133] Y. Yang, D. Constantinescu, and Y. Shi, "Input-to-State Stable Bilateral Teleoperation by Dynamic Interconnection and Damping Injection: Theory and Experiments," *IEEE Trans. Ind. Electron.*, vol. 67, no. 1, pp. 790-799, Jan, 2020.
[134] H. G. Lee, H. J. Hyung, and D. W. Lee, "Egocentric teleoperation approach," *International Journal of Control Automation and Systems*, vol. 15, no. 6, pp. 2744-2753, Dec, 2017.
[135] D. Q. Truong, B. N. M. Truong, N. T. Trung, S. Abu Nahian, and K. K. Ahn, "Force Reflecting Joystick Control for Applications to Bilateral Teleoperation in Construction Machinery," *Int. J. Pr. Eng. Man.*, vol. 18, no. 3, pp. 301-315, Mar, 2017.
[136] H. Y. Wen, W. L. Xu, and M. Cong, "Kinematic Model and Analysis of an Actuation Redundant Parallel Robot With Higher Kinematic Pairs for Jaw Movement," *IEEE Trans. Ind. Electron.*, vol. 62, no. 3, pp. 1590-1598, Mar, 2015.
[137] J. Aleotti, G. Micconi, S. Caselli, G. Benassi, N. Zambelli, M. Bettelli, and A. Zappettini, "Detection of Nuclear Sources by UAV Teleoperation Using a Visuo-Haptic Augmented Reality Interface," *Sensors (Basel)*, vol. 17, no. 10, pp. 2234, 2017.
[138] B. Willaert, B. Corteville, D. Reynaerts, H. Van Brussel, and E. B. Vander Poorten, "A mechatronic analysis of the classical position-force controller based on bounded environment passivity," *Int. J. Robot Res.*, vol. 30, no. 4, pp. 444-462, 2011/04/01, 2010.
[139] C. P. Vo, X. D. To, and K. K. Ahn, "A Novel Adaptive Gain Integral Terminal Sliding Mode Control scheme of a Pneumatic Artificial Muscle system with Time-delay Estimation," *IEEE Access*, pp. 1-1, 2019.
[140] F. H. Huang, W. Zhang, Z. Chen, J. Z. Tang, W. Song, and S. Q. Zhu, "RBFNN-Based Adaptive Sliding Mode Control Design for Nonlinear Bilateral Teleoperation System Under Time-Varying Delays," *Ieee Access*, vol. 7, pp. 11905-11912, 2019.
[141] H. Cho, H. Lee, Y. Kim, and J. Kim, "Design of an Optical Soft Sensor for Measuring Fingertip Force and Contact Recognition," *International Journal of Control Automation and Systems*, vol. 15, no. 1, pp. 16-24, Feb, 2017.

[142] F. Zhou, B. Dong, and Y. C. Li, "Torque Sensorless Force/position Decentralized Control for Constrained Reconfigurable Manipulator with Harmonic Drive Transmission," *International Journal of Control Automation and Systems*, vol. 15, no. 5, pp. 2364-2375, Oct, 2017.
[143] T. Q. Dinh, J. I. Yoon, J. Marco, P. Jennings, K. K. Ahn, and C. Ha, "Sensorless force feedback joystick control for teleoperation of construction equipment," *Int. J. Pr. Eng. Man.*, vol. 18, no. 7, pp. 955-969, Jul, 2017.
[144] P. A. Ioannou, and J. Sun, "Robust adaptive control," in *Book Robust adaptive control*: Prentice-Hall, Inc., 1995.
[145] J. Na, G. Herrmann, R. Burke, and C. Brace, "Adaptive input and parameter estimation with application to engine torque estimation," in 2015 54th IEEE Conference on Decision and Control (CDC), Osaka, Japan, 2015, pp. 3687-3692.
[146] M. N. Mahyuddin, J. Na, G. Herrmann, X. M. Ren, and P. Barber, "Adaptive Observer-Based Parameter Estimation With Application to Road Gradient and Vehicle Mass Estimation," *IEEE Trans. Ind. Electron.*, vol. 61, no. 6, pp. 2851-2863, Jun, 2014.
[147] S. Sastry, and M. Bodson, "Adaptive control: stability, convergence, and robustness," in *Book Adaptive control: stability, convergence, and robustness*: Prentice-Hall, Inc., 1989.
[148] T. X. Dinh, and K. K. Ahn, "Adaptive-gain fast nonsingular terminal sliding mode for position control of a piezo positioning stage," *Proceedings of the Institution of Mechanical Engineers Part I-Journal of Systems and Control Engineering*, vol. 232, no. 8, pp. 994-1014, Aug, 2018.
[149] A. Benveniste, P. Priouret, and M. Métivier, "Adaptive algorithms and stochastic approximations," in *Book Adaptive algorithms and stochastic approximations*: Springer-Verlag, 1990.
[150] D. T. Tran, H. V. A. Truong, and K. K. Ahn, "Adaptive Backstepping Sliding Mode Control Based RBFNN for a Hydraulic Manipulator Including Actuator Dynamics," *Applied Sciences-Basel*, vol. 9, no. 6, Mar 26, 2019.
[151] F. L. Lewis, A. Yesildirek, and L. Kai, "Multilayer neural-net robot controller with guaranteed tracking performance," *IEEE Transactions on Neural Networks*, vol. 7, no. 2, pp. 388-399, 1996.
[152] H. K. Khalil, "Nonlinear systems; 3rd ed.," in *Book Nonlinear systems; 3rd ed.*, 2002.
[153] D. Zhao, S. Li, F. Gao, and Q. Zhu, "Robust adaptive terminal sliding mode-based synchronised position control for multiple motion axes systems," *IET Control Theory & Applications*, vol. 3, no. 1, pp. 136-150, 2009.